

AMERICAN UNIVERSITY OF BEIRUT

QUANTITATIVE CHARACTERIZATION OF
MULTIPHASE MIXTURES APPLIED TO OIL
SPILL THICKNESS MEASUREMENT

by

MAHDI BASSAM SALEH

A dissertation
submitted in partial fulfillment of the requirements
for the degree of Doctor of Philosophy
to the Department of Electrical and Computer Engineering
of the Maroun Semaan Faculty of Engineering and Architecture
at the American University of Beirut

Beirut, Lebanon
December 2020

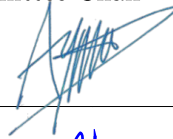
AMERICAN UNIVERSITY OF BEIRUT
QUANTITATIVE CHARACTERIZATION OF
MULTIPHASE MIXTURES APPLIED TO OIL
SPILL THICKNESS MEASUREMENT

by
MAHDI BASSAM SALEH

Approved by:

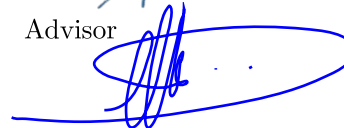
Dr. Ayman Kayssi, Professor
Electrical and Computer Engineering

Committee Chair



Dr. Imad H. Elhajj, Professor
Electrical and Computer Engineering

Advisor



Dr. Daniel Asmar, Associate Professor
Mechanical Engineering

Co-advisor



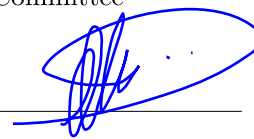
Dr. Naseem Daher, Assistant Professor
Electrical and Computer Engineering

Member of Committee



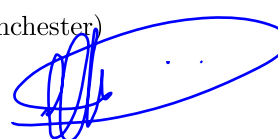
Dr. Najib Metni, Associate Professor
Mechanical Engineering (Notre Dame University – Louaize)

Member of Committee



Dr. Wuqiang Yang, Professor
Electrical and Electronic Engineering (The University of Manchester)

Member of Committee



Date of dissertation defense: December 22, 2020

AMERICAN UNIVERSITY OF BEIRUT

THESIS, DISSERTATION, PROJECT RELEASE FORM

Student Name: Salah Mahdi Bassam
Last First Middle

Master's Thesis

Master's Project

Doctoral Dissertation

I authorize the American University of Beirut to: (a) reproduce hard or electronic copies of my thesis, dissertation, or project; (b) include such copies in the archives and digital repositories of the University; and (c) make freely available such copies to third parties for research or educational purposes.

I authorize the American University of Beirut, to: (a) reproduce hard or electronic copies of it; (b) include such copies in the archives and digital repositories of the University; and (c) make freely available such copies to third parties for research or educational purposes after: **One ___ year from the date of submission of my thesis, dissertation or project.**

Two ___ years from the date of submission of my thesis , dissertation or project.

Three ___ years from the date of submission of my thesis , dissertation or project.

Mahdi Signature
January 12, 2021 Date

Acknowledgements

Special thanks are to my advisors Professor Imad H. Elhadj and Professor Daniel Asmar for their guidance and support throughout my doctoral studies. I am also thankful to all the staff and colleagues from the Vision and Robotics Lab (VRL) for their support. In particular, I would like to acknowledge Ghasan Oueidat, Sevag Babikian, and Mustafa Ammouri for their contributions to implementing the experimental setups and packaging designs.

My recognition and gratitude are addressed to the American University of Beirut (AUB) and the National Council for Scientific Research of Lebanon (CNRS-L) for granting me a doctoral fellowship. I am also thankful for the funding and testing facilities provided by the Bureau of Safety and Environmental Enforcement (BSEE) (Development of Oil Slick Thickness Sensors, BSEE Award E17PC00001, Oil Thickness Sensor Phase II, BSEE Award 140E0118C0003).

I would like to express my sincere appreciation to the members of my dissertation committee for their guidance. I express my gratitude to Professor Ayman Kayssi and Professor Naseem Daher from the American University of Beirut for their time, effort, and support throughout my dissertation work. I am indebted to Professor Wuqiang Yang from the University of Manchester and Professor Najib Metni from Notre Dame University-Louaize for agreeing to act as external referees for my dissertation.

Finally, I wish to thank my family for their love and encouragement. I would like especially thank my father for always supporting me, even when it is not easy to do. I dedicate this work to my wife and children. Without your support, I would not have made it through my PhD degree.

An Abstract of the Thesis of

Mahdi Bassam Saleh for Doctor of Philosophy
Major: Electrical and Computer Engineering

Title: Quantitative Characterization of Multiphase Mixtures Applied to Oil Spill Thickness Measurement

During oil spill incidents, large amounts of oil mixtures spread through open water. Studies have shown that the effectiveness of oil cleaning techniques depends on knowing the actual thickness of oil films. However, under open water conditions, this task is challenging due to wavy sea conditions and varying environmental conditions. This research proposes a new sensing approach that can respond to this need by measuring the thickness of oil included in the multiphase air-oil-water mixture under open water conditions. There are three main contributions of the developed work: first, the proposed method relies on measuring the relative differences between a discrete set of sensing cells, thus, it allows the system to operate without requiring calibration against different types of oil or water. Second, using smart measurement algorithms, the system can operate under dynamic open water conditions and while being dragged. Third, through hardware- and software- based techniques, it mitigates the effect of oil fouling, an issue long considered problematic in the community of oil thickness measurement. In this dissertation, we present the design, implementation, and testing of two sensing systems, the first based on a self-capacitance sensor array and the second based on a dual-modality capacitive/ultrasonic sensing platform aimed to provide oil-thickness measurements in real-time. In addition, we present two additional applications to our proposed sensing methodology related to the measurement of oil viscosity in online applications and the characterization of soil water content. The systems and methods presented in this dissertation have a broader impact on the general field of multiphase characterization.

Contents

Acknowledgements	v
Abstract	vi
1 Introduction	1
1.1 Problem statement	1
1.2 Motivation	1
1.3 Objectives	2
1.4 Contributions	2
1.5 Organization	3
1.6 Publications	3
2 Background and related work	6
2.1 Oil spill sensing methods	6
2.1.1 Remote sensing methods	6
2.1.2 Contact-based sensing methods	7
2.2 Planar capacitive sensors	9
2.3 Segmented electrical sensor arrays	10
2.3.1 Dual-plate sensing systems	10
2.3.2 Single-plate sensing systems	12
2.4 Tomographic sensing systems	13
2.5 Wire-mesh sensing systems	14
2.6 Conclusion	16
3 Self-capacitance sensor array	17
3.1 Proposed sensing approach	17
3.1.1 Design principle	17
3.1.2 Design characteristics	18
3.1.3 Principle of thickness estimation	19
3.2 Sensing method and circuit model	19
3.2.1 Proposed sensing principle	19
3.2.2 Sensor circuit model	21
3.3 System implementation	25

3.3.1	Sensor unit	26
3.3.2	Data acquisition unit	27
3.3.3	Processing unit	29
3.3.4	Housing	30
3.4	Measurement approach	31
3.4.1	Normalization	31
3.4.2	Interface detection	32
3.4.3	Threshold-based detection	33
3.4.4	Edge-based detection	34
3.4.5	Iterative interface detection	35
3.5	Opportunistic filtering	37
3.5.1	Dynamic conditions	37
3.5.2	Highest point algorithm	38
3.5.3	Corrected lowest point algorithm	39
3.6	Operational testing and results	41
3.6.1	Experimental setups	41
3.6.2	Laboratory testing	42
3.6.3	Bridge-mounted tests	46
3.6.4	Skimmer-mounted tests	49
3.7	Conclusion	51
4	Dual-modality sensing system	52
4.1	Proposed sensing approach	52
4.1.1	Sensor fusion	52
4.1.2	Dual-modality sensing	53
4.1.3	Sensing parameters	54
4.2	Capacitive sensor design optimization	56
4.2.1	Design variables	56
4.2.2	Evaluation parameters	57
4.2.3	Design options	58
4.2.4	Assessment via simulations	59
4.2.5	Proposed design	63
4.2.6	Experimental evaluation	66
4.2.7	Conclusion	68
4.3	System implementation	69
4.3.1	Ultrasonic sensor	69
4.3.2	Hand-held device	69
4.3.3	Skimmer-mount device	71
4.4	Classification approach	73
4.4.1	Data acquisition	73
4.4.2	Normalization	74
4.4.3	Feature extraction	75
4.4.4	Classification model	75

4.5	Dataset and model development	76
4.5.1	Dataset creation procedure	76
4.5.2	Applied procedure and created dataset	78
4.5.3	Model development	82
4.6	Experimental evaluation and analysis	83
4.6.1	Ultrasonic sensor	83
4.6.2	Measurement of oil thickness	84
4.7	Conclusion	87
5	Other applications	88
5.1	Measurement of oil viscosity	88
5.1.1	Related work	89
5.1.2	Proposed sensing method	90
5.1.3	Implementation and experimental evaluation	91
5.1.4	Conclusion	92
5.2	Measurement of soil moisture	93
5.2.1	Related work	94
5.2.2	Proposed sensing method	95
5.2.3	Implementation and experimental evaluation	95
5.2.4	Conclusion	98
6	Summary and future work	99
6.1	Summary	99
6.2	Contributions	101
6.3	Limitations	102
6.4	Future work	102
A	Abbreviations	104

List of Figures

2.1	Schematic of the electric field between coplanar electrodes	10
2.2	Segmented capacitive sensor model	11
2.3	3D model of an ECT sensor - Non-invasive electrodes distributed along the periphery of the sensing domain	14
2.4	Wire-mesh sensor model	15
3.1	Illustration of the design principle for the capacitive sensor	18
3.2	Simulation circuit for the self-capacitance sensing mode	21
3.3	Current source signal (left) - Voltage at the capacitor (right)	22
3.4	Circuit model of a sensing cell immersed in a dielectric	23
3.5	Simulation circuit with base and sensor capacitances	24
3.6	Output voltage (V_{out}) vs. sensor capacitance (C_x) - $C_B = 10$ pF	24
3.7	Output voltage (V_{out}) vs. sensor capacitance (C_x)	25
3.8	PCB Layout (from left to right): silkscreen layer, top copper layer, inner copper layer 1, inner copper layer 2, bottom copper layer	26
3.9	Implemented sensor unit. Left: Sensor PCB. Right: Pins	27
3.10	MPR121: charging-discharging measurement cycle	28
3.11	Electrical schematic of the data acquisition unit	29
3.12	Block diagram of the processing unit	30
3.13	Processing unit PCB with components	30
3.14	Complete sensor package	31
3.15	Sample of the sensor output when immersed in a multiphase mixture (y-axis: voltage % change (intensity), x-axis: electrode index)	33
3.16	The rate of change of the intensity output vector (ΔI)	35
3.17	Flow chart of the <i>Get Interface</i> method	36
3.18	Grayscale intensity image	38
3.19	Flow chart of the <i>Highest Point Algorithm</i>	39
3.20	Indoors experimental setup	42
3.21	Outdoors experimental setup	43
3.22	Measured vs. Actual Thickness (Dipping - Diesel)	44
3.23	Measured vs. Actual Thickness (Dipping - Hoops)	44
3.24	Measured vs. Actual Thickness (Dipping - Hydrocal 300)	45
3.25	Measured vs. Actual Thickness (Dipping - Calsol 8240)	46
3.26	Capacitive sensing system mounted to the moving bridge	48

3.27	Measured vs. Actual Thickness (Hydrocal 300) – Bridge	49
3.28	Capacitive sensing system mounted on a skimmer	50
3.29	Skimmer-mounted tests – Experimental results	51
4.1	Sensing principle of the dual-modality system	54
4.2	Capacitance (pF) vs. MUT thickness (mm)	60
4.3	Sensitivity vs. MUT thickness (mm)	61
4.4	Magnitude of the electric field – Top: Without a backplane. Bot- tom: With conductive backplane connected to 0V	62
4.5	Capacitance (pF) vs. lift-off distance (mm)	63
4.6	Magnitude of the electric field - Initial sensor with pins (front view)	64
4.7	Capacitance (pF) vs. MUT thickness (mm)	65
4.8	Electric field magnitude - Single sensing cell	66
4.9	Electric field magnitude - Three separated sensing cells	66
4.10	Electric field magnitude - Five sensing cells	67
4.11	Implemented sensor prototypes (optimization study)	67
4.12	Hand-held device	70
4.13	PCB layout - Hand-held capacitive sensor	71
4.14	Implemented capacitive sensors - hand-held	72
4.15	Implemented skimmer-mount capacitive sensor	73
4.16	Processing unit PCB for the skimmer-mount device	73
4.17	Flow chart of the signal classification method	74
4.18	Flow chart for dataset creation in static mode	77
4.19	Experimental setup for the skimmer-mount device	80
4.20	Oil fouling of the sensing pins - skimmer-mount sensor	81
4.21	Scatter plot of the dataset (black: water, brown: oil)	82
4.22	Ultrasonic distances resulting from max, mean, and median filters	84
4.23	Left: Hand-held testing: container (left), hand-held device (right)	85
5.1	Capacitive sensor board used for viscosity measurement	91
5.2	Experimental setup for viscosity measurement system	92
5.3	Plot of absolute capacitance (pF) vs. position (mm)	93
5.4	Plot of Capacitance Relative Change (%) vs. position (mm)	94
5.5	Coplanar capacitive sensor for soil moisture measurement	96
5.6	Average voltage (ADC) vs. soil moisture - tuning	97
5.7	Relative moisture change vs. time	98

List of Tables

3.1	Disposed oil amounts with actual oil thickness - Lab tank	42
3.2	Disposed oil amounts with actual oil thickness - Bridge testing . .	47
3.3	Test cases for bridge-mounted testing	47
3.4	Wave conditions for skimmer-mounted tests	50
4.1	Design alternatives, including parallel, interleaved with N= 9, in- terleaved with N= 18, and concentric	58
4.2	Results for thickness-sweep simulations	60
4.3	Penetration Depths	63
4.4	Experimental results of the design optimization study	68
4.5	Base voltages for skimmer-mount capacitive sensor 1	79
4.6	Sample of the dataset (static mode) - skimmer-mount sensor . . .	80
4.7	Coefficients of the trained classification models	82
4.8	Hand-held sensor testing (manual) - experimental results	85
4.9	Hand-held sensor testing (fixed) - experimental results	86
4.10	Skimmer-mount device - experimental results	86
4.11	Skimmer-mount device - dynamic testing results	87
5.1	Water amounts and moisture percentages	96

Chapter 1

Introduction

1.1 Problem statement

In-situ characterization of multiphase air-oil-water mixtures under oil spill conditions is challenging due to several factors including the unpredicted mixtures of oil/water types, dynamic (wavy) behavior of the measured liquid, high viscosity of heavy and crude oils, and varying environmental conditions. The main aim of this work is to develop a multiphase sensing system that does not rely on calibration against different types of material and can work under challenging dynamic liquid conditions. The systems and methods presented in this dissertation contribute to enhancing the efficiency of the applied oil spill remediation techniques by providing real-time quantitative information about oil slicks floating on open water surfaces.

1.2 Motivation

Sea routes are used for the transportation of oil across the world using large oil tankers, and with the high volume of traffic at sea, it is not uncommon to witness accidental oil spills. Offshore platforms, oil wells, and pipelines also contribute to the pollution of our seas from oil leaks. For instance, in 2010, an explosion on the *Deepwater Horizon* drilling rig led to a catastrophic oil spill in the northern Gulf of Mexico. During this spill, around 3.19 million barrels of toxic oil were released into the ocean causing long-term impacts on coastal habitats [1]. In addition to such accidental spills, frequent illegal oil discharges play a significant role in polluting the marine ecosystem. In general, oil spills have long-term hazardous effects on the environment, especially on human health and living organisms, such as birds, sea mammals, and fish [2].

Since oil is lighter than water, it rises to the top of the ocean surface and floats, thereby forming a thin layer known as an oil slick. Under open water conditions, the location and extent of oil spills could be tracked using modern remote sensing

techniques. Tracking the locations of oil spills is essential for applying effective countermeasures. However, obtaining information about the local thickness of oil slicks presents an extremely challenging task, mainly due to the properties of oils which may form unpredicted mixtures whose appearance may change as a function of time and weather conditions [3].

Knowing the exact thickness of oil slicks in the local area to be treated is one of the key features impacting the effectiveness of the applied remediation techniques. For instance, when at least one millimeter of oil slick thickness is detected, in-situ burning becomes an option [4]. For emulsified oils, in-situ burning is possible only at a thickness ranging from three to ten millimeters. Application of chemical dispersants is another remediation technique that relies on oil thickness information; the slick thickness should be greater than two millimeters for the effective application of chemical dispersants [5]. Other methods used to recover oil such as skimmers, also rely on oil thickness information to head in the direction of the thickest oil concentrations [6]. Note that skimmers perform physical oil/water separation and oil thickness information is important to control their pumping rate and to assess their performance in real-time.

1.3 Objectives

The primary objective of this dissertation is to develop a sensing method for measuring multiphase mixtures composed of materials with distinct electrical properties such as oil and water. As an application for the proposed sensing method, we focus on measuring the thickness of oil slicks caused by accidental oil spills in open water environments. The secondary objectives include the development of robust classification algorithms to infer and track interfaces separating different components of the multiphase mixture in real-time. In addition, signal filtering methods were studied to mitigate the effects of dynamic liquid conditions on the measurement accuracy.

1.4 Contributions

The main contribution of the developed work is to provide an in situ multiphase measurement system that can work under dynamic and harsh liquid conditions (waves and dragging). In contrast to other systems available in the literature, the proposed system is able to perform the following tasks:

- provide oil slick thickness measurements in real-time
- detect and track more than one interface (gas-oil, oil-water)
- operate against different types of oil and water without requiring calibration
- mitigate the effect of oil fouling caused by highly viscous oils

1.5 Organization

The remaining of this dissertation is organized as the following:

Chapter 2 reviews the sensing methods presented in the literature for measuring oil spills. Also, it explains the theoretical principles related to electrical sensing systems developed for measuring multiphase mixtures in process monitoring applications.

Chapter 3 presents the design, implementation, and testing of the first measurement system based on a self-capacitance array. This chapter starts by describing the proposed sensing approach based on the concept of geometrical sensing. Then, it presents the implementation details including the sensor, data acquisition, and signal processing units. At the end of this chapter, the operational testing of the implemented prototype is presented and the results are discussed.

Chapter 4 presents the design, implementation, and testing of the second sensing system based on a dual-modality ultrasonic/capacitive sensing platform. After describing the proposed dual-modality sensing approach, the implementation details are discussed. Based on the dual-modality sensing principle, two different devices were implemented to meet different use-case applications. The first device is a hand-held sensor designed to measure oil slick thicknesses in testing facilities and from on-board vessels to obtain sample measurements in the field. The second sensing device is designed for mounting on skimmers, buoys, or in an oil spill boom apex to provide thickness data in a field application.

Chapter 5 presents two additional applications which lend themselves well to this type of coplanar capacitive sensing. The first section describes a new sensing method for detecting the viscosity of oils in online measurement applications. The proposed method is based on analyzing the changes in the capacitance of a coplanar capacitive sensor while being moved from the oil phase to the air phase. The second section presents the use of a self-capacitance sensor array for measuring the moisture of soil at different depths.

Chapter 6 summarizes the main topics presented in this dissertation and lists the main contributions and limitations of the proposed methods. In addition, it provides possible tracks for future development.

1.6 Publications

At the time of writing, this dissertation work has been incrementally published in several articles, papers, and reports listed below.

Patent Applications

- I. H. Elhajj, D. Asmar, M. Saleh, and G. Oueidat, “Thickness measurement device and methods of use,” Aug. 8 2019. US Patent App. 16/243,584

Journal Articles

- M. Saleh, G. Oueidat, I. H. Elhajj, and D. Asmar, “In situ measurement of oil slick thickness,” *IEEE Transactions on Instrumentation and Measurement*, vol. 68, no. 7, pp. 2635–2647, 2018

Conference Papers

- M. Saleh, I. H. Elhajj, D. Asmar, and S. Antoun, “Real-time detection of oil viscosity using coplanar capacitive sensors,” in *2020 IEEE Sensors*, IEEE, 2020
- M. Saleh, I. H. Elhajj, and D. Asmar, “Capacitive sensing for measuring oil thickness under fouling conditions,” in *2019 IEEE International Instrumentation and Measurement Technology Conference (I2MTC)*, IEEE, 2019
- M. Saleh, I. H. Elhajj, and D. Asmar, “An opportunistic approach for mitigating fouling in the measurement of oil thickness,” in *2019 IEEE International Instrumentation and Measurement Technology Conference (I2MTC)*, IEEE, 2019
- M. Saleh, G. Oueidat, M. Ghamlouch, I. H. Elhajj, and D. Asmar, “LED-based Spectrometer for In Situ Oil Slick Thickness Measurement,” in *2018 IEEE International Multidisciplinary Conference on Engineering Technology (IMCET)*, IEEE, 2018
- M. Saleh, I. H. Elhajj, D. Asmar, I. Bashour, and S. Kidess, “Experimental evaluation of low-cost resistive soil moisture sensors,” in *IEEE International Multidisciplinary Conference on Engineering Technology (IMCET)*, pp. 179–184, IEEE, 2016

Datasets

- M. Saleh, I. H. Elhajj, D. Asmar, “Dataset for binary classification of digital sensor signals”, *IEEE Dataport*, October 5, 2020

Technical Reports

- I. H. Elhajj, D. Asmar, M. Saleh, and G. Oueidat, “Development of oil slick thickness sensors,” tech. rep., Bureau of Safety and Environmental Enforcement, 2018

Contributed Articles

- M. Saleh, I. H. Elhajj, and D. Asmar, “In situ profiling of soil water content,” *Annual Climate Change Student Competition 2017-2018 Climate Change and Land in the Middle East and North Africa Region*, 2018

- M. Saleh, I. H. Elhajj, and D. Asmar, “Sensors measure oil thickness,” *The Ohmsett Gazette*, 2018
- I. H. Elhajj, D. Asmar, M. Saleh, and G. Oueidat, “Sensors for oil slick detection and thickness measurement,” *ISCO Newsletter*, vol. 626, 2018

Chapter 2

Background and related work

2.1 Oil spill sensing methods

Several studies were performed to develop systems and methods for oil spill sensing in open water environments. In this section, we describe some of the major methods used for detecting and characterizing oil spills at different scales. These methods can be categorized into two general categories: remote-based (long-range) and contact-based (short-range).

2.1.1 Remote sensing methods

Remote sensing techniques based on visual imaging and visual observation, are widely used for providing a large-scale assessment of oil spill area and thickness. By utilizing airborne vehicles, human experts can provide an estimate of the oil slick thickness based on color observations. Although such techniques can be useful, they are affected by environmental conditions such as haze and light reflection from the sea, the temperature of the environment, and sea conditions [7]. Multi-spectral and hyper-spectral imaging from airborne vehicles are also used to detect and monitor oil spills [8]. Studies showed that by using this type of imaging with appropriate processing and analysis techniques, oil slicks could be identified and continuously monitored. Limitations of these methods include the high cost of the imaging equipment and their sensitivity to cloud coverage, lighting conditions, and sea state.

Microwave passive imaging techniques were used for measuring oil spill thickness from airborne or satellite platforms. These methods are relatively unaffected by cloud coverage and adverse weather conditions. For instance, in the work of Calla *et al.* [9], oil spill locations were detected through temperature measurements, collected from a Special Sensor Microwave/Imager (SSM/I), and an Advanced Microwave Scanning Radiometer for EOS (AMSR-E) satellite carrying passive microwave sensors. The analysis of the satellite images showed that the temperature of the oil spill area was higher than that of the surrounding unpol-

luted areas. Therefore, real-time monitoring for a sudden or abnormal shift in temperature within the same area may be used for detecting an oil spill. On the downside, the measurement (versus detection) of the oil thickness based on temperature variations could not be easily performed, because the temperature of the oil is affected by several factors other than its thickness, such as its dielectric constant [10].

In [11], intensity images produced by Synthetic Aperture Radar (SAR) were used to identify oil spill areas. This method requires high processing-time to discriminate between oil spill areas and other dark areas caused by some natural phenomena (biogenic slicks, currents, low wind areas). Intensity images are also produced by infrared imaging techniques. These techniques measure the re-emitted portion of solar radiation absorbed by optically thick layers of oil [12]. In particular, parts of the absorbed solar radiation are emitted as thermal energy in the wavelength region between 8 and 14 μm . Thus, thermal cameras are used to detect oil slicks based on detecting predefined temperature signatures. The problem with these methods is that oil films with intermediate thicknesses may appear cold, and very thin oil layers, usually known as “sheens”, may be hard to detect based on temperature variations.

To summarize, although the remote-based sensing technologies are successful in detecting oil spills and assessing their extent at large scales, they cannot be used for accurate measurement of oil slick thickness at local scales. The contact-based/short-range sensing techniques designed to provide a localized measurement of oil slick thickness are discussed in the next section.

2.1.2 Contact-based sensing methods

Contact-based/short-range sensing techniques refer to traditional instrumentation approaches, such as those relying on optical and electrical sensing methods. Some of these methods designed for oil slick thickness measurement applications are described below.

Several studies focused on detecting the presence of oil slicks using short-range spectral analysis devices. For instance, Karathanassi [13] studied the spectral behavior of different types of oil using a commercial hand-held spectro-radiometer device *GER 1500* [14] working in the wavelength range between 350 and 1050 nm. The spectro-radiometer was used to record the spectral signatures of a set of oil samples with different thicknesses under laboratory and field conditions. The laboratory experiments included light and heavy oils, at thicknesses ranging from 1 to 200 μm . The results showed a high correlation between the spectral reflectance and the oil thickness. These results indicated that, given the oil type, the estimated correlation functions could be used to determine the oil slick thickness. On the other hand, the experiments performed in the marine environment showed that weather conditions and spectral characteristics of the sea bottom impacted the spectral signatures of thin oil films. Thus, the correlation equa-

tions obtained from the laboratory experiments were not applicable to be used in the marine environment.

Optical-based sensing systems rely on the phenomenon of light absorption or reflection to determine the oil slick thickness. These systems are capable of detecting oil thicknesses at very high resolutions, in the order of μm . For instance, Massaro *et al.* [15] proposed an optical sensing system, composed of two optical fibers to extract the relation between different oil concentrations and the intensity of a reflected light beam. Inferring the oil thickness was performed by analyzing the intensity of the received light, after being reflected from the measured oil layer. Another optical-based system presented by Baozhen *et al.* [16] aimed to measure the thickness of thin oil films by using differential laser triangulation; it emits a laser beam on the oil surface and measures the deviation angle of the reflected beam. In addition to the reflection-based methods, other optical sensing systems relied on analyzing the intensity of the absorbed light after passing through the examined oil layer. For instance, Oh and Lee [17] proposed an attenuation-based optical sensing system composed of a set of Light Emitting Diodes (LEDs) and a Charged Couple Device (CCD) sensor. The images produced by the sensor were analyzed to infer the attenuation of the light beams after passing through the oil layer. The experimental results showed that the maximum variation of the received light intensity, against oil thicknesses, was observed at a wavelength of 465 nm.

Despite that the optical-based sensing systems produce accurate results under controlled laboratory experimental conditions, they have several limitations that affect their usability in real oil-spill thickness measurement applications. For instance, all optical-based sensing methods are affected by the optical properties of the examined oil (*e.g.* refractive index). These properties affect the sensitivity and range of the optical sensors and accordingly impose a requirement for calibration against different types of oil. Note that under oil spill conditions, the composition and physical properties of oil mixtures may change with time. Thus, the dependency of the optical methods on the physical properties of oils represents a major limitation for using them under realistic oil spill conditions. In addition to this major limitation, we should note that the optical lenses can be fouled by heavy oil types and as a result may impact the correctness of the estimated oil thickness as shown in our previous work presented in [18].

In addition to the optical-based sensing systems, other studies proposed the combination of electrical and light sensor arrays to measure the oil slick thickness. For instance, in the work of Denkilkian *et al.* [19], two arrays of conductivity and light sensors were combined to form a calibration-independent sensing system for measuring the oil slick thickness. The light sensors were distributed vertically along a cylindrical platform to detect the variation in the emitted light intensity as it propagates horizontally through different phases of the oil-water mixture. The conductivity sensors were implemented using a set of metallic probes connected to a set of resistors. A microcontroller was used to measure the variations

in the electrical resistance of different phases included in the oil-water mixture. Note that different aqueous solutions feature different electrical properties; in contrast to seawater, which is highly conductive because of its sodium ions, the oil possesses low electric conductivity. Although the implemented prototype provided accurate measurements under static conditions, it suffered from problems of corrosion, as well as a low resolution in the order of several centimeters.

To summarize, the electrical-based sensing methods were considered more suitable than other contact-based methods for providing localized measurements of oil slick thickness under oil spill conditions. However, electrical systems presented in the literature have several limitations including the dependency on calibration, requirement for temperature compensation, and being severely affected by dynamic (wavy) liquid conditions.

2.2 Planar capacitive sensors

Planar Capacitive Sensors (PCS) represent one category of electrical sensing systems where the sensing plates (electrodes) are mounted next to each other on the same plane [20]. They have several advantages over other electrical sensing modalities, such as simplicity and low cost of manufacturing, fast sensing rates, and low maintenance requirements. Due to these advantages, they have been used in a wide variety of applications including security scanners [21], Non-Destructive Evaluation (NDE) [22], and industrial process monitoring applications [23].

The operating principle of the PCS systems follows the basic principle of capacitive sensing which could be explained based on 2.1 representing the capacitance of a parallel-plate capacitor; two conductive plates facing each other with a dielectric material filling the gap between them. Any change in the capacitance parameters, such as the distance between the plates or the type of dielectric, has a direct impact on the measured capacitance. Thus, based on capacitance measurements, sensors are designed to infer and track structural or dimensional changes in a certain physical phenomenon.

$$C = \frac{\epsilon_0 \epsilon_r A}{D} \quad (2.1)$$

where C is the capacitance in Farads, ϵ_0 is the permittivity of free space (8.85×10^{-12} Farad per meter), ϵ_r is the relative permittivity of the dielectric, A is the surface area of the plates measured in $meter^2$, and D is the distance between the plates measured in meters.

Capacitive sensors operate at low-frequencies in which the electromagnetic field follows the quasi-static approximation, which neglects the magnetic flux and a static electric field is assumed between the plates. Since the conductive plates are mounted next to each other in PCS systems, the electric field extends beyond the sensing plane (see Figure 2.1). Thus, the electric field distribution is created

within the material located in front of the sensing plane; usually known as the Material Under Test (MUT). As the electrical properties of the MUT changes, the electric field pattern is affected differently. These changes in the electric field cause related changes in the charge of the sensing electrodes and consequently change the capacitance between them.

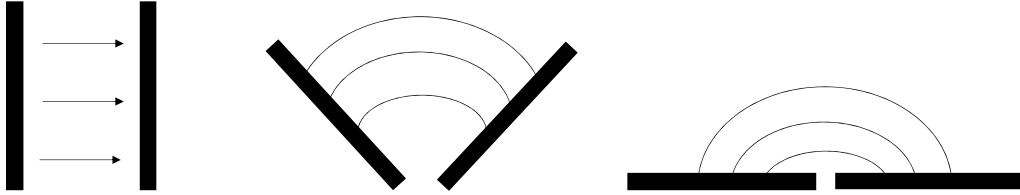


Figure 2.1: Schematic of the electric field between coplanar electrodes

A data acquisition unit is usually used to measure the capacitance between the sensing electrodes. This unit is composed of a set of circuits responsible for providing electrical excitation to the electrodes and measuring the resulting capacitance formed between them. The measured capacitances are sent to an image reconstruction unit to infer the permittivity distribution of the MUT. The estimated permittivity distribution, displayed as an intensity-based image, could be analyzed using traditional image processing techniques to extract the dimensions of the multiphase mixture components.

2.3 Segmented electrical sensor arrays

In the literature, different types of electrical sensor arrays were designed for imaging and material characterization applications [24]. Many of these systems were aimed at characterizing multiphase flows inside industrial process plants and crude oil separators [25]. Generally, these systems could be categorized into either dual-plate or single-plate systems. In what follows we present the working principle of these systems and discuss their main limitations.

2.3.1 Dual-plate sensing systems

The first segmented sensing system for liquid level detection was presented by *Shell* in 1984 [26]. The system is composed of a set of vertically disposed U-shaped sensing cells as illustrated in Figure 2.2, where L , W , and G represents the width, length, and gap of the cells respectively.

Each of the sensing cells has three conductive elements: an excitation element, a detection element, and a zero-potential element. The cells are excited with an

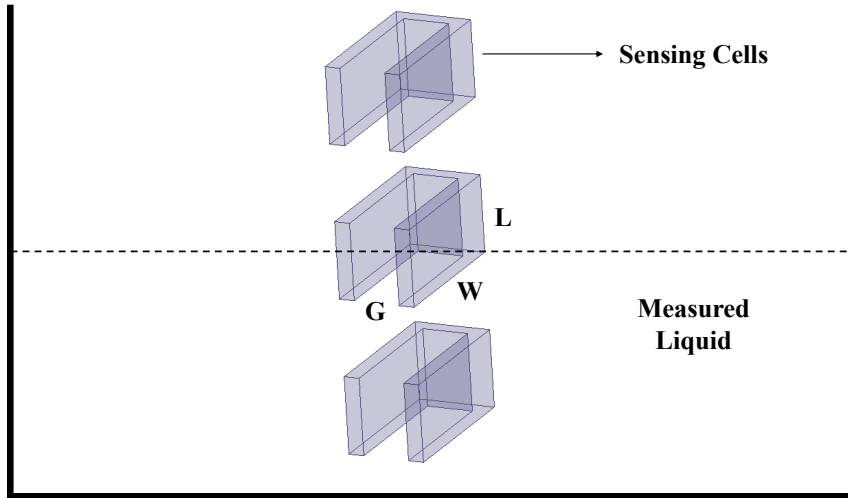


Figure 2.2: Segmented capacitive sensor model

AC voltage signal with a frequency of 25 KHz. At the receiver, an amplifier circuit is used to measure the variations in the amplitude and phase of the transmitted signal. The transmitted signal is affected differently based on the electrical properties of the material filling the gap between the excitation and detection electrodes. Based on this difference, the system detects the cell that possesses an intermediate capacitance between the capacitances of the cells immersed in gas and liquid phases; this cell is known as the *interface* since it separates the gas phase from the liquid phase. After identifying the interface cell, the fraction of its immersion in the liquid is estimated using an interpolation method that assumes a linear relationship between the measured capacitance and the level of the liquid filling the cell. The output of the system is the total liquid level which is calculated by summing the height of the interface cell and the fraction of the liquid filling it.

One major limitation of this system is related to the structure of its U-shaped sensing cells which increases the probability of oil buildup between the transmitter and receiver elements. This probability increases when dealing with heavy and crude oils, especially when working under dynamic liquid conditions. Another limitation is related to the interface detection method which relies on knowing the capacitance of the cells under different conditions (air and liquid). In other words, the system should be calibrated against different types of liquids and under different environmental conditions.

Another multi-interface detection system proposed by Yang *et al.* [27] includes a segmented capacitance sensor designed to characterize multiphase flows in oil separators. The first plate consists of an array of 64 electrodes (20 x 10 mm),

excited sequentially via four multiplexers. A sinusoidal voltage signal of 10 KHz frequency and 20 VPP was used for excitation. The second plate consists of a common detection electrode with a length of 808 mm, used for capacitance measurement. The detection electrode was connected to a stray-immune capacitance-to-voltage converter. The two plates were isolated with an epoxy resin layer, and housed in stainless steel tubes facing each other; the plates are separated with a distance of 13 mm. To detect the foam layer, the authors proposed a method based on Fast Fourier Transform (FFT) analysis. The interfaces between different materials were detected by analyzing the normalized differences between adjacent electrodes.

Based on multi-modality sensing, a multi-interface level measurement system was presented by Hwili and Yang in [28]. This system works based on combining capacitance and electromagnetic measurements to detect the interfaces between different materials included in crude oil separators. The multi-modality sensing principle was used to overcome the problems related to the use of single-modality capacitive and electromagnetic sensors. For instance, capacitive sensors are affected by fouling, temperature changes, and short-circuiting when working against conductive material. On the other hand, single-modality electromagnetic sensors cannot be used to differentiate between insulating materials such as gas and oil. By combining the information obtained from the two sensing techniques, the system was able to differentiate between different conductive and non-conductive layers included in the measured multiphase mixture.

It is important to note that the dual-plate sensing systems presented in the literature were designed for deployment in crude oil separators and were not intended to be used in open water environments. Thus, even though the developed interface detection method was able to find transition points between different phases under static liquid conditions, it is not guaranteed to work correctly under dynamic liquid conditions where oil fouling plays a significant role in affecting the output signal. Thus, it may not be possible to track the interfaces using a simple edge detection algorithm. In addition, with the high viscosity of crude oils, there is a high risk of oil build up between the emitter and receiver plates forming the dual-plate sensing systems.

2.3.2 Single-plate sensing systems

Single-plate segmented sensors were proposed to handle the problem of oil-blockage and to reduce manufacturing costs, dimensions, and design complexity of the dual-plate systems. The first multi-electrode capacitive array, following the single plate structure, was presented by Shi *et al.* in 1991 [29]. The sensor is composed of a double-sided Printed Circuit Board (PCB) plate holding a set of electrodes on the top layer and the connection tracks on the bottom layer. It works by measuring the changes in the fringe capacitance between couples of adjacent electrodes mounted along the vertical sensing plane. The electrodes were connected through

a multiplexer to a capacitance-to-voltage converter working based on the charge-transfer principle. A low-pass filter was used to extract the DC component of the measured signal, and a band-pass filter extracted the AC component. The output signal components were sent to an analog-to-digital converter (A/D) connected to a computer for analysis. Detection of the interface cell was done by comparing the measured capacitances to a set of predefined thresholds (acquired through calibration). Interpolation was used to detect the exact location of the interface within the initially identified interface cell.

Other studies focused on optimizing the design of the electrodes included in single-plate sensors. For instance, Wang *et al.* [30] presented a simulation-based study using the Finite Element Method (FEM) to enhance the performance of the single-plate sensors by selecting the optimum geometrical design parameters. In the conclusion of their optimization study, the authors proposed to use comb-shaped electrodes to enhance the sensitivity of the single-plate sensors.

Although the single-plate segmented sensors presented in the literature solved the problem of oil blockage, they did not provide a solution for the problem of oil fouling that could affect the performance of the sensors when operating under dynamic liquid conditions. In particular, when the electrodes mounted on the same sensing plane move from the oil phase to the water phase, they may be covered by a thin layer of oil, separating them from contacting the water. Because of the relatively high ratio of sensor vertical velocity to electrode cleaning, single-plate sensors are inadvertently affected by oil fouling.

2.4 Tomographic sensing systems

Electrical tomography is an imaging technique that provides cross-sectional images characterizing the distribution of different materials included in a multiphase mixture [31]. It works by measuring the changes in the electrical properties of the materials included in the sensing domain by using a set of electrodes distributed along its periphery. This working principle is known as *soft sensing* and differs from the traditional *hard sensing* principles used in medical imaging systems such as x-ray which rely on measuring the attenuation of the transmitted signals. Electrical tomography systems have several advantages over traditional imaging systems in terms of response rate, cost, and safety. Electrical Capacitance Tomography (ECT) is one member of the family of electrical tomography techniques that relies on capacitance measurements between different pairs of electrodes distributed around the sensing domain (see Figure 2.3) [32].

Several ECT systems were developed to measure multiphase flows. For instance, the system presented in [33] was designed to measure the layers of water, oil/water emulsion, oil, foam, and gas inside an oil separator. The sensing electrodes are distributed around the process to be imaged and connected to a data acquisition unit. The capacitance between different combinations of electrodes is

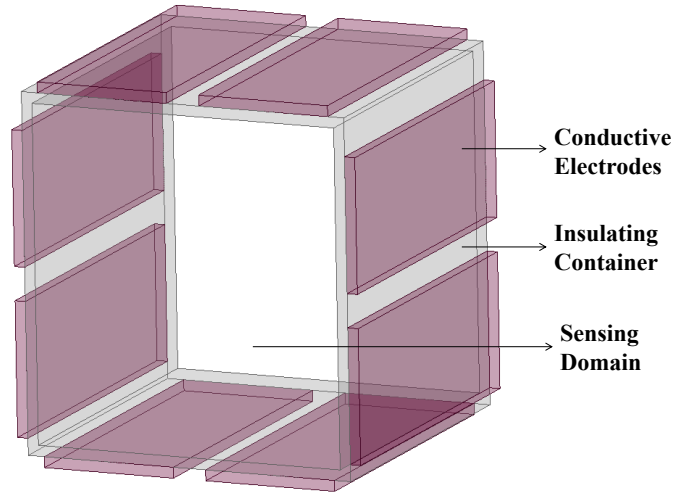


Figure 2.3: 3D model of an ECT sensor - Non-invasive electrodes distributed along the periphery of the sensing domain

measured sequentially using a multiplexer and a capacitance detector. The measurements are fed as input parameters to the image reconstruction algorithm, which produces a cross-sectional image showing the components of the sensing area.

One major limitation of the ECT technique is that the reconstructed images are approximate (qualitative) and has a low resolution. In addition, most of the implemented tomographic systems are applied to closed circular vessels. For open water sensing applications, such as oil spills, the planar segmented sensing systems are preferred over the tomographic systems due to their reduced size and complexity.

2.5 Wire-mesh sensing systems

Wire-mesh sensing systems are based on a predetermined grid pattern of wires under tension; horizontal and vertical (see Figure 2.4). The two planes of wires are spaced at a predetermined distance from each other. Depending on the measurement modality, these systems could be classified as conductive or capacitive systems. Usually, conductive systems are used to measure the level of conductive liquids, such as water, and capacitive systems are intended to work against dielectrics such as oil.

A wire-mesh sensing system based on conductivity measurements was presented in [34]. This system was designed to measure the water-cut in a multi-phase flow. It works based on measuring the conductivity of the material filling the space at the intersection of the vertical and horizontal wires of the mesh. For

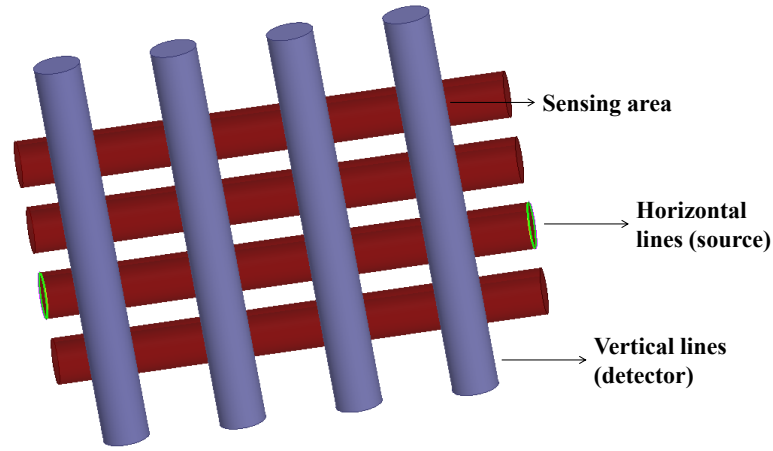


Figure 2.4: Wire-mesh sensor model

this purpose, the voltages at the vertical lines are measured sequentially while one of the horizontal lines is connected to a voltage source. This process is repeated for each horizontal line in the mesh. As a result, a matrix of 16 values could be created from a mesh containing four vertical lines and four horizontal lines. The resulting matrix represents the conductivity distribution of the fluid flow passing through the sensor mesh. The level of water is determined given the measurement matrix and knowing the geometrical dimensions of the sensor mesh.

Another wire-mesh sensor based on permittivity measurements was presented in [35]. The sensor is designed to work against non-conducting fluids, such as oil or other organic liquids. The wire-mesh consists of two planes of 16 stainless steel wires with 0.12 mm diameter each. The wires are separated from each other in the same plane by 3.12 mm and between the two planes along the axial direction by 1.5 mm. The sensor mesh is mounted on an acrylic frame that forms a part of the rectangular flow channel. The principle of operation is based on measuring the capacitance between the intersections of lines included in the wire-mesh. The capacitance is assumed to be directly proportional to the relative permittivity of the material located at the intersection. To measure the capacitance, an AC measurement configuration was used; a sinusoidal alternating voltage signal is applied as an excitation to the transmitter electrode and a trans-impedance amplifier is used to measure the current at the receiver electrode.

2.6 Conclusion

Based on the assessment of the sensing systems presented in the literature, it was found that the planar capacitive sensing systems are most suitable for the oil-spill sensing application due to their simple sensor design and sensitivity to conductive and non-conductive material such as water and oil. However, most of the capacitive-based instruments presented in the literature require calibration against different types of material. As mentioned before, the calibration requirement represents a major limitation to the use of these systems under oil spill conditions.

Chapter 3

Self-capacitance sensor array

This chapter describes the design, implementation, and testing of a sensing system based on a self-capacitance sensor array designed for measuring the thickness of oil slicks under open-water conditions. There are three main advantages of the proposed system over the prior art: first, it can operate in dynamic environments, measuring the oil thickness in wavy sea environments and while being dragged. Second, only initial factory calibration is required; once a baseline capacitance is recorded in the air, the system can be used to measure the thickness of different types of oil. Third, using solutions in both software and hardware, it significantly mitigates the effect of oil fouling, an issue long considered problematic in the community of oil thickness measurement. The proposed system was implemented and tested extensively, first in a lab, then inside a large outdoor pool, by dragging the sensor at different velocities, through waves of varying amplitude and frequency. The results of the experiments demonstrated the accuracy and robustness of the proposed system using multiple oil types and thicknesses, under static and dynamic conditions.

3.1 Proposed sensing approach

This section introduces the main principles of the proposed sensing system including the sensor design, its characteristics, and the oil-thickness estimation approach.

3.1.1 Design principle

The sensor design is based on an array of horizontal sensing pads (electrodes), stratified vertically along a planar sensing platform (see Figure 3.1). Since the dielectric constant (also known as the relative permittivity) of the material surrounding each of the electrodes is directly related to its capacitance, capacitances measured at all electrodes could be used to identify those electrodes that are im-

mersed in oil, those in water, and those that are in air. In addition, analyzing the variation of the capacitances measured at adjacent electrodes allows for the detection of the interfaces separating distinct components of the multiphase mixture. The thickness of the oil layer is calculated given the geometrical dimensions of the electrodes immersed in the oil phase. This sensing approach offers the sensor immunity to changes in environmental conditions and removes the need for calibration against different types of water or oil.

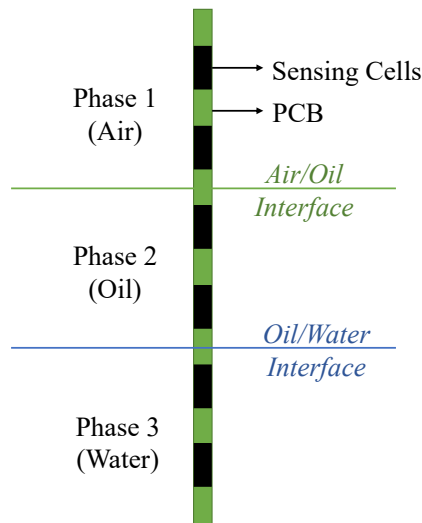


Figure 3.1: Illustration of the design principle for the capacitive sensor

3.1.2 Design characteristics

The main characteristics of the proposed sensing system are as follows.

- Planar shape

To reduce the amount of oil that could be accumulated around traditional sensors implemented using pipes or cylindrical structures, the proposed system follows a thin (knife-like) planar design based on a multi-layer Printed Circuit Board (PCB). This allows the sensor to cut through water vertically (up and down) or horizontally if it is being dragged.

- Anti-fouling mechanism

Since the sensing platform is in direct contact with the multiphase mixture, an important aspect to consider is the fouling problem: when any electrode transitions from oil to the adjacent medium of water or air, any residual

oil can result in a false measurement. In order to mitigate the undesirable effect of oil fouling caused by high viscosity oil types, the proposed system uses a set of thin needle-like pins mounted perpendicular to the horizontal sensing pads. The pins allows the sensor to penetrate the oil layer caused by fouling and enhances the rate of signal change.

- Opportunistic filtering method

An opportunistic filtering algorithm was developed to mitigate the effect of oil fouling on measurement accuracy. The proposed algorithm is based on detecting the measurements performed while the sensor is positioned at the optimum positions in terms of the lowest expected error.

3.1.3 Principle of thickness estimation

The general approach for oil thickness estimation is based on a two-step process. First, the oil-water and air-oil interfaces are detected. Second, the thickness of the target oil layer is calculated based on the geometrical properties of the electrodes immersed in oil. It is important to note that by designing the interface detection algorithm based on differential rather than absolute measurements, the proposed method circumvent the need for any static calibration formula. In addition, this approach does not depend on knowing the exact positions of the oil or the water phases along the sensor body. Thus, in contrast to traditional capacitive sensing systems presented in the literature, it does not require a floater to maintain a fixed position of the sensor on the top of the liquid surface.

3.2 Sensing method and circuit model

The proposed sensing system is based on measuring the capacitance of an array of electrodes mounted on a planar platform. This section presents the proposed capacitive sensing method and describes the circuit model of the sensor.

3.2.1 Proposed sensing principle

Several modes of capacitive sensing can be used for material identification. One of the widely used modes is known as the *Transmission Mode (TM)*. This mode is based on measuring the *mutual capacitance* between adjacent pairs of electrodes. Thus, a pair of electrodes are required to perform a single capacitance measurement; the first electrode acts as the transmitter, usually connected to an Alternating Current (AC) oscillator, and the second electrode acts as the receiver, usually connected to a current detection circuit (trans-impedance amplifier (TIA)). The transmission sensing mode was used in several applications

including liquid level detection [36] and proximity detection of moving targets [37].

The dependency of the transmission sensing mode on pairs of electrodes to measure a single capacitance has implications on the design of the sensor array and on the complexity of the system. To simplify the measurement process, another mode of capacitive sensing known as the *Single-electrode Mode (SM)* is used. This mode relies on measuring the *self-capacitance* of the sensing probes sequentially. In contrast to the transmission mode, this mode requires only a single electrode that acts as both the excitation electrode and the measurement electrode. It is applied by charging the target electrode using direct electric current (DC) for a specific amount of time. Then, at the end of the charging phase, the voltage of the electrode is measured relative to the system ground. Note that the electrical current passing through a capacitor is related to the change in voltage relative to time, as shown in 3.1.

$$i = C \frac{dv}{dt} \quad (3.1)$$

where C is the capacitance in Farads, i is the instantaneous current flowing through the capacitor in Amperes, and $\frac{dv}{dt}$ is the rate of voltage change in Volts/second.

The self-capacitance sensing method was adopted in our system due to its advantages including the design simplicity and high sensitivity to changes in material properties [20]. Based on this mode, each of the electrodes included in the sensor array acts independently from the other electrodes and is used for both excitation and measurement. As the excitation current is a positive constant, the voltage increases linearly and the sensor is considered “charging” because more charges are accumulated on its probes. Consequently, the intensity of the electric field also increases since it is directly related to the amount of charge. On the other hand, when the current is a negative constant, the voltage decreases linearly and the sensor is considered “discharging”. The voltage measured at the end of the charging phase could be represented by integrating 3.1 relative to time as shown in 3.2, leading to 3.3. As shown in 3.3, the capacitance (C) is inversely related to the measured voltage (V) and could be calculated given the charging current (I) and duration (T).

$$\int_0^T i dt = C \int_0^T \frac{dv}{dt} dt \quad (3.2)$$

$$C = \frac{IT}{V} \quad (3.3)$$

where I is the charging current in Amperes (Coulombs/second), T is the charge duration in seconds, C is the capacitance in Farads, and V is the voltage in Volts.

As a demonstration for the self-capacitance sensing method, a simulation was designed using the *Proteus* software provided by *Labcenter Electronics*. First, an excitation signal was created using two pulse current sources as shown in Figure 3.2. The charging parameters of the current sources are set to $63 \mu\text{A}$ and $0.5 \mu\text{s}$. The generated current signal was displayed using an Analog Analysis Graph (AAG) equipped with the current probes S_1 and S_2 . The time interval of the analysis was set to $10 \mu\text{s}$, allowing the observation of 10 consecutive measurement cycles. A second AAG with a similar time interval was used to plot the voltage of the sensing channel as measured by the voltage probe V_{out} . The simulation was activated after connecting a capacitor of 20 pF between the probe V_{out} and the system ground (GND); this capacitor represents the capacitance of the sensing channel. The signals obtained from the two AAGs are shown in Figure 3.3.

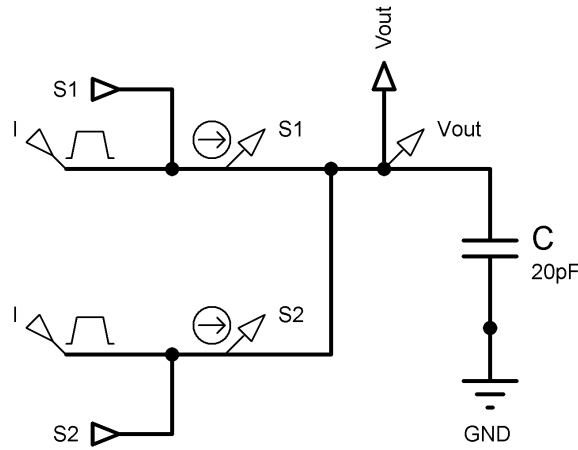


Figure 3.2: Simulation circuit for the self-capacitance sensing mode

The simulation result demonstrates the triangular behavior of the capacitor's voltage (V_{out}) when supplied by a pulsed DC excitation. The voltage measured at the end of the charging phase (1.57 V) could be used to infer the capacitance given the charging parameters; $C = (63 \mu\text{A})(0.5 \mu\text{s}) / 1.57 \text{ V} = 20 \text{ pF}$.

3.2.2 Sensor circuit model

The electrodes are connected to a set of sensing channels in the data acquisition unit. The connection between each electrode and the corresponding channel is made via a thin conductive track embedded in the inner layers of the PCB and surrounded by conductive sheets acting as passive shields. Thus, to create an accurate circuit model for a single sensing channel, all of the capacitances involved in different sections of the channel should be taken into account. Based on this fact, we categorize the components of the measured channel capacitance C_{Ch} , into two major parts:

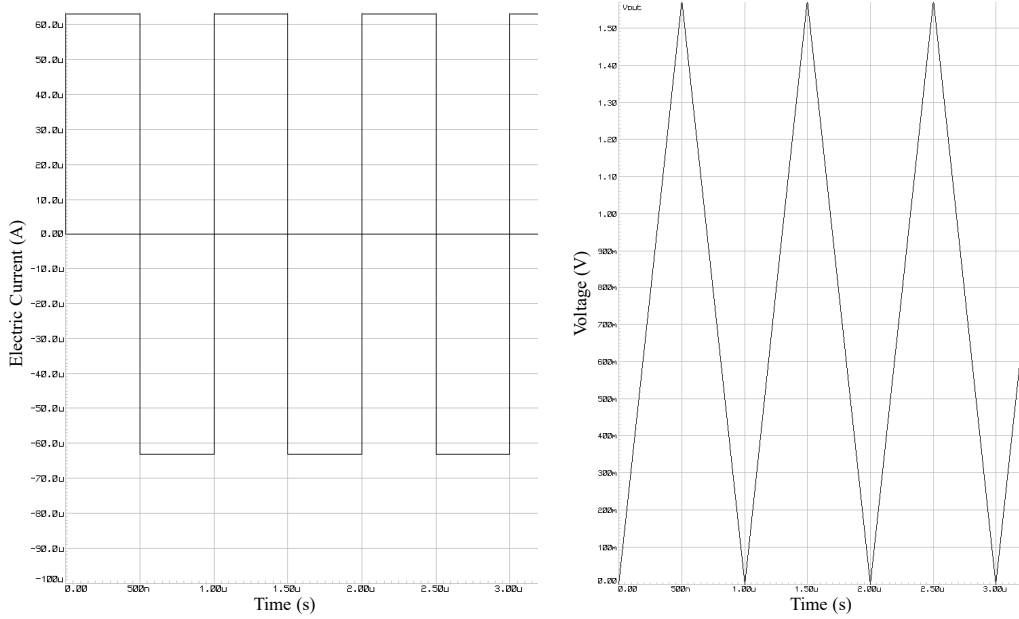


Figure 3.3: Current source signal (left) - Voltage at the capacitor (right)

1. Base capacitance (C_B): represents the capacitance between the connection trace and the surrounding shielding. The base capacitance is constant and does not change due to material contact.
2. Sensor capacitance (C_X): represents the capacitance between the electrodes forming a single sensing cell. The sensor capacitance is variable and increases due to material contact; when the sensor is immersed in the measured material.

In general, the circuit model representing a single sensing cell (electrodes filled by the measured material) is represented by a lossy capacitor model to account for the conductivity of the material. The model is composed of a capacitor C_x connected in parallel with a resistor R_x . The two components represent the electrical properties of the material filling the gap between the electrodes. When the conductivity of the material is less than a certain limit, the material acts as an insulator, and the resistor could be removed from the model. Thus, when dealing with an insulating material such as oil or air, at room temperature, the equivalent circuit model of the sensing cell could be described by a single capacitor C_x . In this case, the model of the sensing cell is considered as “capacitance dominant”. The sensor capacitance (C_X) is proportional to the relative permittivity of the sensed material (ϵ_r) as shown in 3.4.

$$C_x = \epsilon_r(\epsilon_0 K_g) \quad (3.4)$$

Since the electrodes are exposed to the measured material, the sensor capacitance is added in parallel to the base capacitance when the sensor is immersed in the multiphase mixture. The basic circuit model representing a single sensing cell immersed in the insulating material is shown in Figure 3.4. When the sensor is immersed in air, the relative permittivity of the sensed material is approximated as one ($\epsilon_{r(air)} = 1$); thus, the sensor capacitance is a constant represented by $C_0 = C_{x(air)} = \epsilon_0 K_g$. If the sensor is immersed in any other material having a relative permittivity greater than one, the sensor capacitance increases. For instance, if the sensed material is oil with a relative permittivity of three, the sensor capacitance is represented as $C_{x(oil)} = 3 \times C_0$.

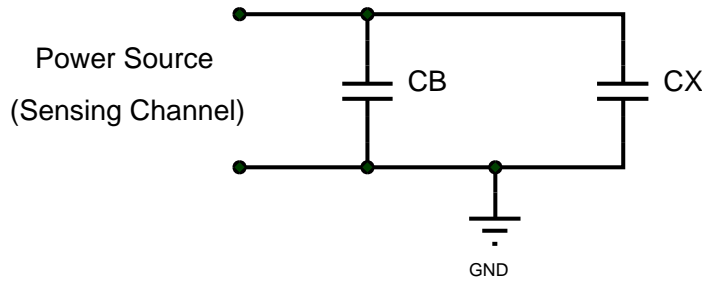


Figure 3.4: Circuit model of a sensing cell immersed in a dielectric

As described before, the proposed sensing method relies on calculating the capacitance given the voltage measured at the end of the charging phase. The measured voltage (V_T) is defined in terms of the base and sensor capacitances as shown in 3.5. Note that the measured voltage is inversely related to the sensor capacitance C_X . This relation is not linear and the base capacitance C_B plays a major role in affecting the sensitivity of the sensor output (voltage) relative to variations in the measured capacitance C_X .

$$V_T = \frac{Q}{C_B + C_X} \quad (3.5)$$

To demonstrate the relation between the base capacitance (standing capacitance) and the measured voltage, simulations were performed after adding a constant base capacitance ($C_B = 10$ pF) to the simulation circuit described before (see Figure 3.5). In these simulations, we increased the sensor capacitance C_X from 1 pF to 20 pF with increments of 1 pF. The output voltages obtained from calculations and simulations are plotted in Figure 3.6.

The simulation showed that the voltage is inversely and non-linearly related to the sensor capacitance C_x . To monitor the effect of the base capacitance on the sensor output, the base capacitance was increased gradually from 10 pF to 20 pF with increments of 2 pF. After each increment, the voltage was calculated while increasing the sensor capacitance from 1 pF to 20 pF with increments of

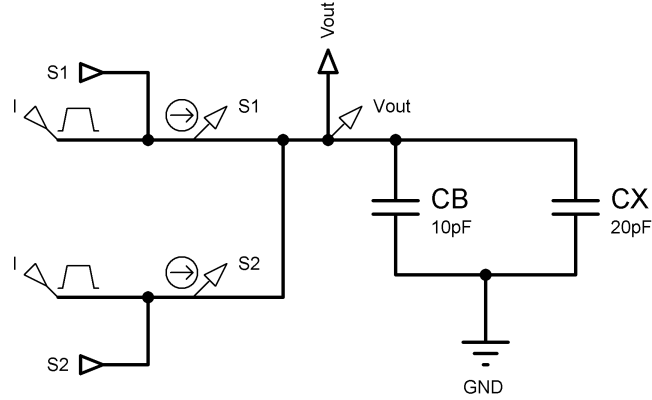


Figure 3.5: Simulation circuit with base and sensor capacitances

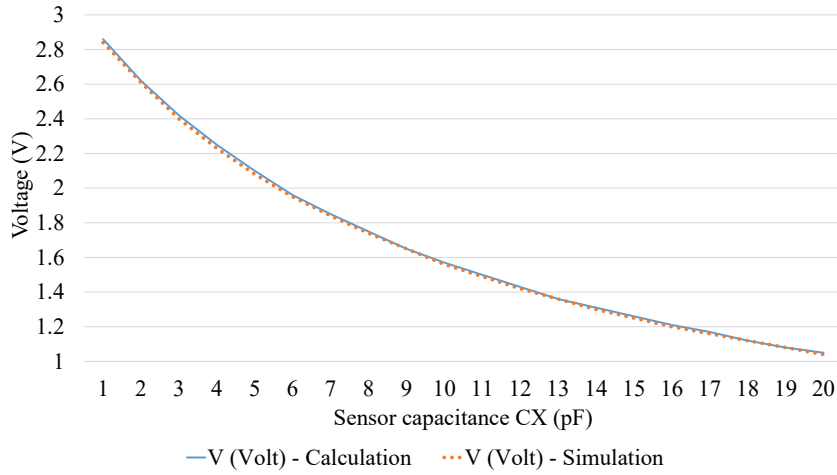


Figure 3.6: Output voltage (V_{out}) vs. sensor capacitance (C_x) - $C_B = 10$ pF

1 pF. The output voltages relative to different base capacitances are plotted in Figure 3.7.

The simulation results demonstrate the effect of the base capacitance on the sensitivity of the sensor. In particular, as the base capacitance increases, the sensitivity of the output voltage to the changes in the sensor capacitance decreases. Note that the steepness of the voltage slope decreases as the base capacitance increases. In conclusion, we can say that minimizing the base capacitance is essential to maximize the sensitivity of the proposed self-capacitance sensing method.

It is important to note that in case of conductive material, the conductivity of the sensed material should be considered in the sensor model. This is done by representing the sensing cell as a first order RC circuit. Based on the working principle of the proposed sensing method, the measured voltage drops with an

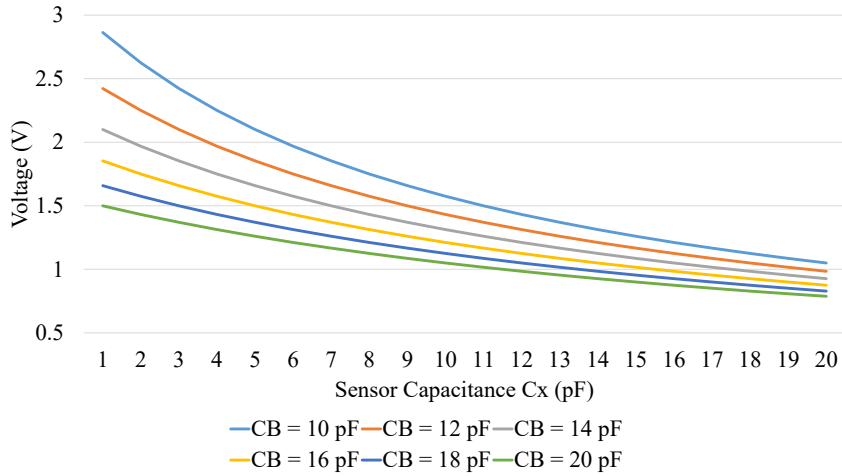


Figure 3.7: Output voltage (V_{out}) vs. sensor capacitance (C_x)

increase in the material’s conductivity (decrease in the resistance). Thus, it can be concluded that the sensing method can be used to differentiate between different types of insulating materials such as air and oil, and between insulating and conductive materials such as oil and water.

The correctness of the proposed sensor model was validated experimentally by performing measurements under different conditions. For instance, the measured voltage drops to around zero when the sensing electrodes are immersed in water. Also, it was validated experimentally that the drop in the measured voltage increases in a directly proportional manner to the amount of salt added to tested samples of distilled water. Validating the correctness of the sensor model against insulating material was performed by connecting circuit components with small capacitances to the sensing electrodes and observing the increase in the measured capacitances. For instance, in one of the measurements, a two-pin wire connector (terminal block) was connected to the sensor electrodes and its capacitance of around 1.5 pF was measured using an LCR meter device. The capacitance of different sensing channels increased in an identical manner to the values expected by the parallel-connection model proposed for the insulating material.

3.3 System implementation

This section describes the implementation of different components of the self-capacitance sensing system including the sensor board, data acquisition unit, and processing unit.

3.3.1 Sensor unit

The proposed sensor design was implemented using a multi-layer PCB, holding a set of conductive pads (electrodes) on its surface layers (see Figure 3.8). The inner layers of the PCB hold the copper traces connecting the sensing electrodes to the capacitive transducers shown in the upper section of the implemented PCB (see Figure 3.9 (left)). To cover the desired sensing range (100 mm), forty-eight electrodes were used with a width of 2 mm each. The vertical gap separating the electrodes from each other is 1 mm. The total dimensions of the implemented sensor board are a width of 60 mm, a thickness of 1.6 mm, and a total length of 250 mm.

The resolution of the measurement depends on the dimensions of the sensing electrodes. For instance, in this particular prototype, the width of the electrodes is 2 mm and the vertical gap separating them from each other is 1 mm. Thus, the implemented sensor prototype is capable of measuring the thickness of oil layers ranging between 3 mm and 100 mm with a step resolution of 3 mm. The measurement resolution could be enhanced by decreasing the width of the electrodes and the size of the gap between them. However, this process is limited by manufacturing capabilities.

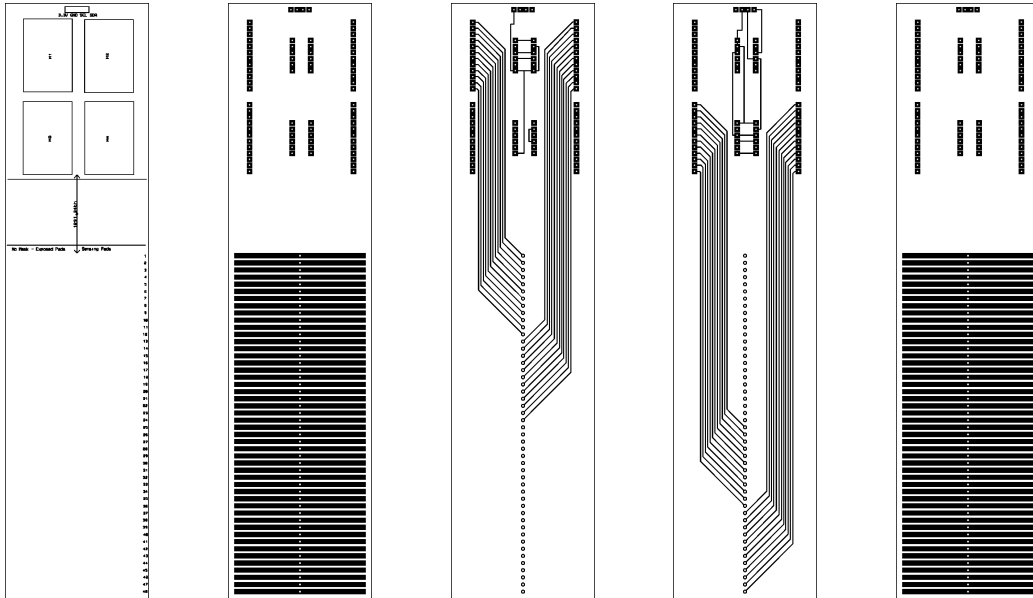


Figure 3.8: PCB Layout (from left to right): silkscreen layer, top copper layer, inner copper layer 1, inner copper layer 2, bottom copper layer

As mentioned earlier, due to the high viscosity of crude and heavy oil types, thin oil layers could be accumulated on the sensor body isolating some of the planar electrodes from their surrounding mediums. To help mitigate the oil fouling problem, we inserted horizontal pins into the sensing board. These pins con-

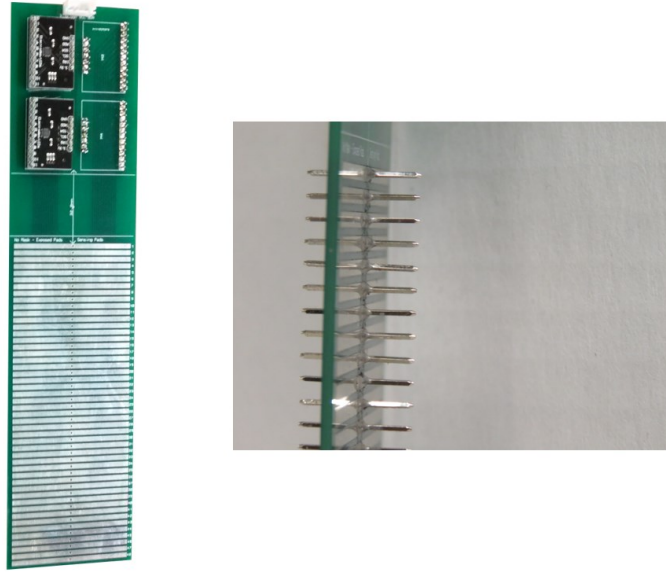


Figure 3.9: Implemented sensor unit. Left: Sensor PCB. Right: Pins

tribute to decreasing the fouling effect by allowing the electrodes to penetrate the oil layer covering the sensor body. The implemented sensor prototype with the inserted pins is shown in Figure 3.9 (right).

3.3.2 Data acquisition unit

The data acquisition unit is composed of four capacitive transducers MPR121 [38] mounted on the sensor PCB and controlled by a microcontroller. The MPR121 chip is designed for touch and proximity sensing applications. It works based on the single-electrode sensing mode and has several advantages over other available Capacitance-to-Digital-Converters (CDCs). For instance, it supports twelve sensing channels and could be connected to a microcontroller through an I2C communication channel. In terms of power requirements, it works with an input voltage ranging between 1.6 V and 3.3 V which is suitable for low-power microcontroller-based circuits and has a very low power consumption of 29 μA . Other advantages of the MPR121 chip include its fast response rate of 16 ms, the embedded multiplexing, filtering, and analog-to-digital conversion, and an operating temperature ranging between -40°C to $+85^{\circ}\text{C}$. It is important to note that several MPR121 chips could be connected to a single I2C channel and differentiated by using unique addresses.

The decision to mount the capacitive transducers on the sensor PCB was made after testing several initial prototypes that were equipped with D-subminiature connectors to connect the sensor boards to other independent data acquisition units. Due to mechanical variations, connector bending, and aging of soldering,

several disconnections of electrodes were recorded in the initial tests. Thus, this method of implementation offers a direct connection between the sensing channel pin and the electrode, avoiding possible disconnection problems that may occur due to the use of connection sockets or terminals.

As illustrated in Figure 3.10, the MPR121 capacitive transducers work by measuring the voltage of the electrode (V_T) after applying a constant amount of electric current (I) for a fixed duration of time (T). Since the current supplied to the sensing channel is constant, the voltage of the channel increases linearly during the charging phase. Note that the rate of change of the voltage is proportional to the supplied current; the slope of the voltage will be steeper as the current increases and vice versa. The capacitance (C) could be derived from the measured voltage and the predefined charging parameters as shown in 3.6. It is important to note that before charging the electrode, the corresponding channel is grounded to ensure that the voltage starts from zero.

$$C = \frac{Q}{V} \quad (3.6)$$

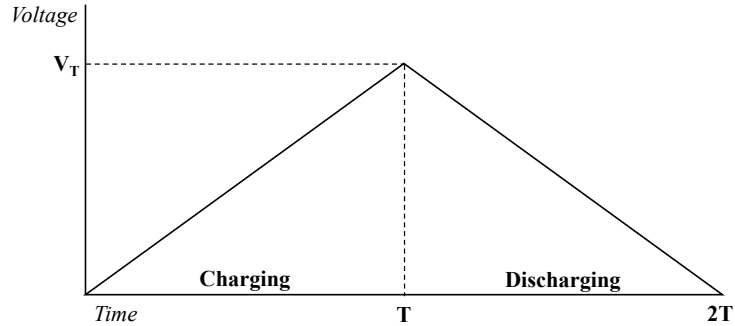


Figure 3.10: MPR121: charging-discharging measurement cycle

Note that since the electric current is defined as the rate of flow of charge, then, the amount of electrical current multiplied by the charging duration gives the total amount of the accumulated charge; $Q = I \times T$. The MPR121 module includes a set of registers for configuring the charging parameters (electric current and charging duration) and to store the voltages measured at each electrode. The measured voltage is converted to digital format and stored in one of the memory registers. This conversion is done using an embedded 10-bit Analog-to-Digital Converter (ADC) which represent the analog range in 1024 steps. For a power supply of 3.3 V ($V_{DD} = 3.3$ V), the relation between the analog voltage (V_{Analog}) and the digital voltage (V_{ADC}) is presented in 3.7. Given the measured digital voltage value, the capacitance could be calculated using 3.8.

$$V_{Analog} = 3.3 \times \frac{V_{ADC}}{1023} \quad (3.7)$$

$$C = \frac{Q \times 1023}{3.3 \times V_{ADC}} \quad (3.8)$$

As mentioned before, each of the MPR121 modules supports twelve sensing electrodes and is connected to the microcontroller through an I2C communication channel. Addressing of the four MPR121 modules is performed by connecting their address pins (ADD) to GND, 3.3 V, SDA, and SCL pins. These connections provide the following addresses to the MPR121 modules: 0x5A, 0x5B, 0x5C, and 0x5D. The four MPR121 modules were connected to the 48 electrodes as shown in Figure 3.11.

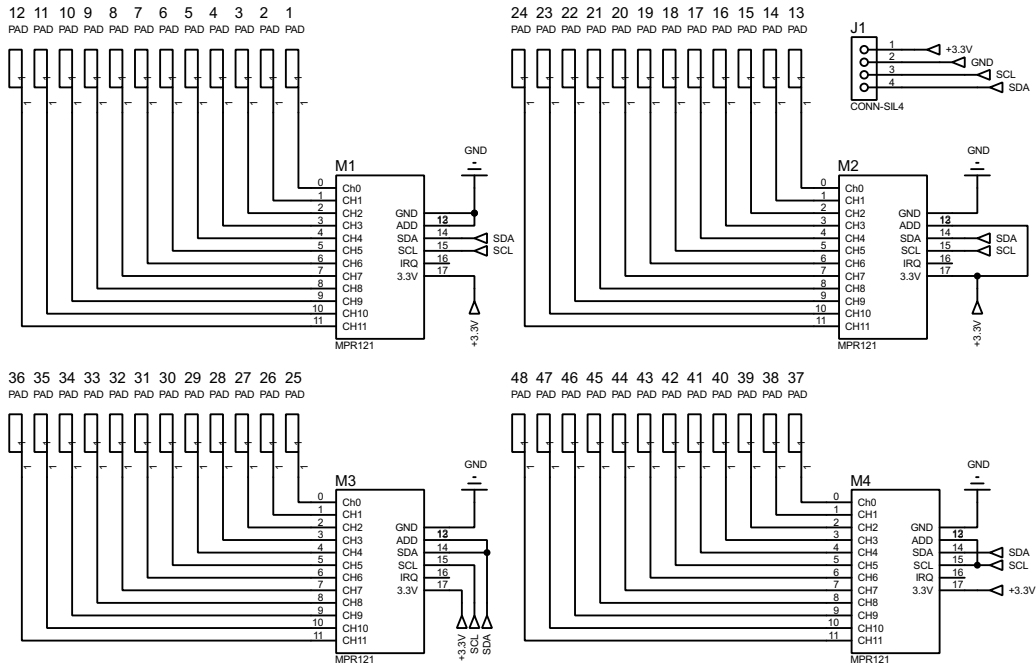


Figure 3.11: Electrical schematic of the data acquisition unit

3.3.3 Processing unit

The processing unit is composed of a microcontroller-based embedded system (Arduino Nano) that controls the data acquisition unit, receives the voltage measurements, applies the measurement algorithm, and sends the results wirelessly to a base station. In addition to the wireless communication module, the unit is equipped with a GPS module to provide location information during operation. The processing unit is independent from the sensor PCB and is connected to it

using a 4-pin wire that provides the required voltage signal and carries the measured data. This implementation method allows the replacement of the sensor cartridge without applying any changes to the processing unit. A block diagram showing the main components of the processing unit is shown in Figure 3.12. The implemented PCB holding the components of the processing unit including the wireless communication module is shown in Figure 3.13.

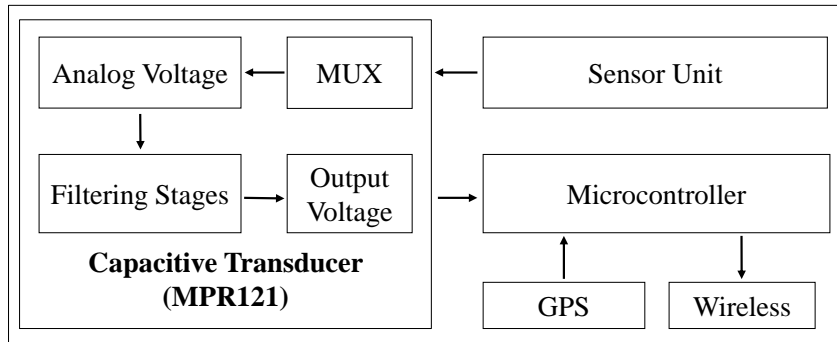


Figure 3.12: Block diagram of the processing unit

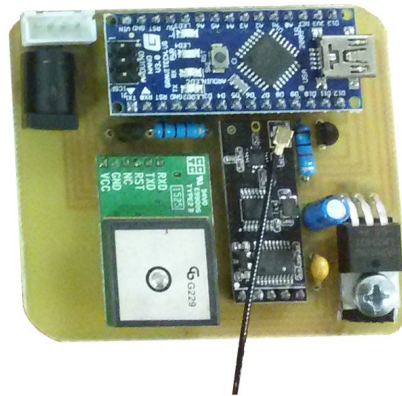


Figure 3.13: Processing unit PCB with components

3.3.4 Housing

The packaging was designed to fit the dimensions of the capacitive sensor and to provide waterproof protection for the electric components. The package parts were machined out of Polyamide, selected for its durability and shock absorption properties. Sealing was achieved by applying pressure on rubber O-rings

and gaskets. A set of experiments were performed to confirm the package's water resistance under different conditions: continuous water splashing, continuous contact with running water, and submersion in water to a depth of twenty centimeters. The final package design was retrofitted with a simple mechanism for mounting on different skimmers and floating platforms. Figure 3.14 shows the packaging design assembled with the sensor cartridge.

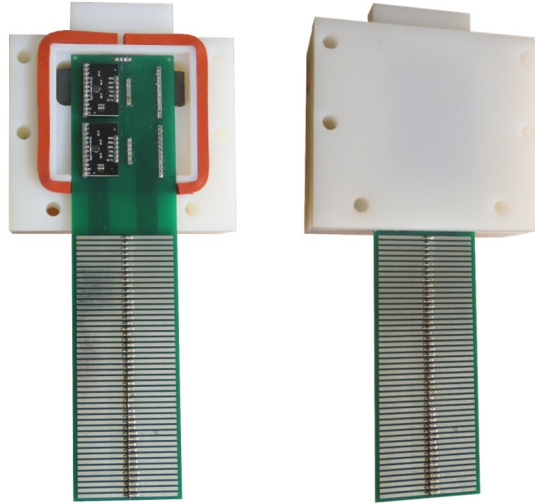


Figure 3.14: Complete sensor package

3.4 Measurement approach

As mentioned before, measuring the oil thickness is based on detecting the interfaces between different liquid layers (air-oil and oil-water). Then, the oil thickness could be inferred given the dimensions of the sensor electrodes and the number of the oil-immersed electrodes. To detect the interfaces separating the oil phase from the other phases, several techniques could be used. This section discusses the possible interface detection methods and introduces our proposed iterative interface detection process.

3.4.1 Normalization

The interface detection process starts by normalizing the output of the sensor array. The normalization step is essential because the base capacitances of the sensing channels are different and depend on several factors including the dimensions of the electrodes, the length of the connection traces, and other manufacturing aspects. Based on this fact, each electrode has a different voltage even

when the sensor is immersed in air. Thus, to infer the type of material contacting each of the electrodes, the absolute measured voltages should be normalized relative to the base voltages. For this purpose, given the voltage of each electrode in real-time, we calculate the percentage change from its reference voltage recorded in air. For instance, the percentage change (% change) of the voltage of the electrode with index n from its reference voltage, denoted as its intensity I_n , is calculated as shown in 3.9. The term *intensity* was used because it refers to the amount of the high permittivity material (water) found at a specific sensing region. Note that if an electrode is totally immersed in water, the percentage change of its measured voltage (around zero) relative to its reference voltage (recorded in air) is maximum (100). As the permittivity of the sensed material decreases, the percentage change of the measured voltage relative to the reference voltage decreases until reaching zero when the electrode is totally immersed in air; in this case, the measured voltage is equal to the reference voltage and the intensity is zero.

$$I_n = \text{voltage \% change } (n) = \frac{|V_{m(n)} - V_{ref(n)}|}{V_{ref(n)}} \times 100 \quad (3.9)$$

where n is the spatial index of the electrode, $V_{m(n)}$ is the voltage of the electrode n measured in real-time, and $V_{ref(n)}$ is the reference voltage of the electrode n recorded when the sensor is immersed in air.

At each measurement cycle, performed at time instant t , a vector of intensity values is acquired. During a fixed duration of time (fixed-size temporal window), a constant number of consecutive intensity vectors is acquired as represented in 3.10.

$$I_{temp} = (I_t \quad I_{t+1} \quad \dots \quad I_T) \quad (3.10)$$

where T is the total number of measurement cycles performed. Note that the intensity vector calculated at the time instant t , represented by I_t , contains the intensities of all electrodes included in the sensor array. The number of rows is equal to the count of the electrodes; for instance, since we are using 48 electrodes, each column has 48 elements in it.

3.4.2 Interface detection

The voltage measured at the oil-immersed electrodes is different from that measured at the water-immersed and the air-immersed electrodes. Thus, one way to measure the oil thickness is based on identifying the number of electrodes immersed in oil after detecting the upper and lower boundaries separating the oil phase from the air and water phases; the upper and lower boundaries of the oil phase are known as the interfaces. After detecting the number of electrodes im-

mersed in the oil phase (N_O), the oil thickness is calculated using the geometrical dimensions of the sensor as shown in 3.11.

$$\text{Oil Thickness} = (N_O)(W) + (N_O - 1)(G) \quad (3.11)$$

where W is the width of the electrodes (2 mm), and G is the vertical gap between the electrodes (1 mm).

Interface detection could be done by searching for sharp increases (step change) in the measured voltages or the normalized intensities. For instance, Figure 3.15 shows the output intensities (percentage change of voltages) of the sensor array when placed in a multiphase air-oil-water mixture. Note that the x-axis represents the electrode indices starting from the top electrode (electrode 1) at the left side, to the bottom electrode (electrode 24) at the right side. The y-axis represents the intensities calculated based on 3.9. The electrodes showing an intensity of zero are immersed in air, other electrodes showing a very high intensity of greater than 40 percent are immersed in water, and the remaining electrodes are immersed in oil showing an intermediate intensity ranging from 3 to 15 percent.

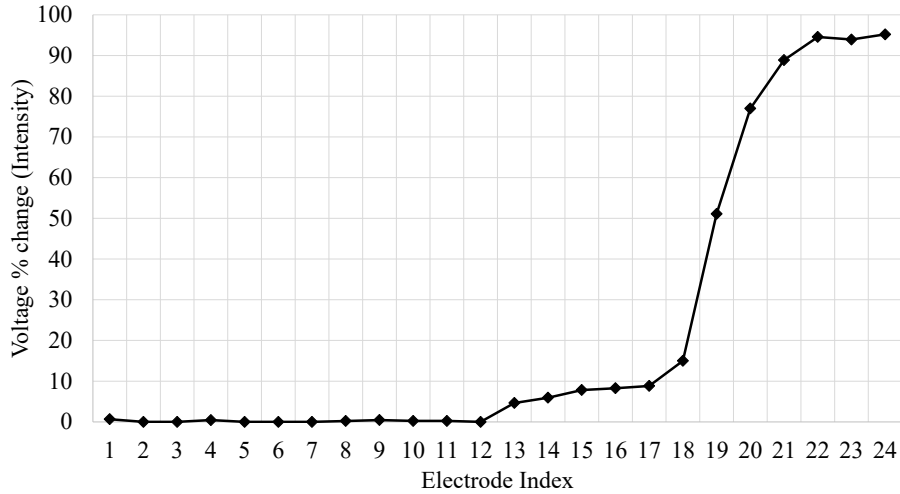


Figure 3.15: Sample of the sensor output when immersed in a multiphase mixture (y-axis: voltage % change (intensity), x-axis: electrode index)

3.4.3 Threshold-based detection

A threshold-based detection method could be used to detect the oil-immersed electrodes. This method relies on an assumption that the oil-immersed electrodes possess an intensity value ranging between a certain low threshold (3 percent) and a high threshold (15 percent); the interval of intensity values related to the oil-immersed electrodes is called the *oil intensity interval*. Starting from the top

electrode, the first electrode that shows in intensity value greater than the lower threshold is considered the air-oil interface. The oil-water interface is the last electrode (bottom) showing an intensity value greater than belonging to the oil intensity interval. For instance, based on the intensity output shown in Figure 3.15, we can detect the upper and lower interfaces of the oil layer at electrode 13 and electrode 18, respectively. Then, the oil thickness could be estimated using the predefined geometrical properties of the electrodes located between the two interfaces.

The threshold-based detection method could be used to detect the interfaces and consequently the oil thickness under relatively calm liquid condition with no disturbances or movements involved. This is because the change in the intensity is not instantaneous when one electrode changes from one phase to another. Another limitation of this method is its dependency on a set of predefined values to detect the air, oil, and water electrodes. Note that these values may change due to material properties or dynamic environmental conditions. Thus, repetitive calibration may be required to update the the threshold values depending on the operational conditions.

3.4.4 Edge-based detection

Another method for detecting the boundaries of the target phase (oil) is inspired from the traditional edge detection techniques used in image processing and segmentation applications. This method relies on calculating the differences between adjacent elements in the sensor array. By calculating the differences between neighboring elements, we track the rate of change of intensity values starting from the top electrode to the bottom electrode. Then, the interfaces could be detected at the two peaks, showing a significant step-change in the intensity, when moving from air to oil electrodes and then from oil to water electrodes. More formally, the rate of change of the output intensity vector is obtained by calculating its first derivative ΔI as shown in 3.12, where n is the spatial index of the electrodes.

$$\Delta I_n = I_n - I_{n-1} \quad (3.12)$$

For demonstration, the results of calculating the first derivative of the intensity vector shown before in Figure 3.15 are plotted in Figure 3.16. In this case, two peaks could be detected at electrodes 19 and 13 representing the bottom and top interfaces of the oil layer. By subtracting the indices of the two detected interfaces, we obtain the number of electrodes immersed in the oil phase and the thickness of the oil layer could be deduced.

Note that the peak of the air-oil interface (electrode 13) is much smaller than that of the oil-water interface (electrode 19). This is due to the limited change in intensity between air and oil electrodes in comparison to the change encountered

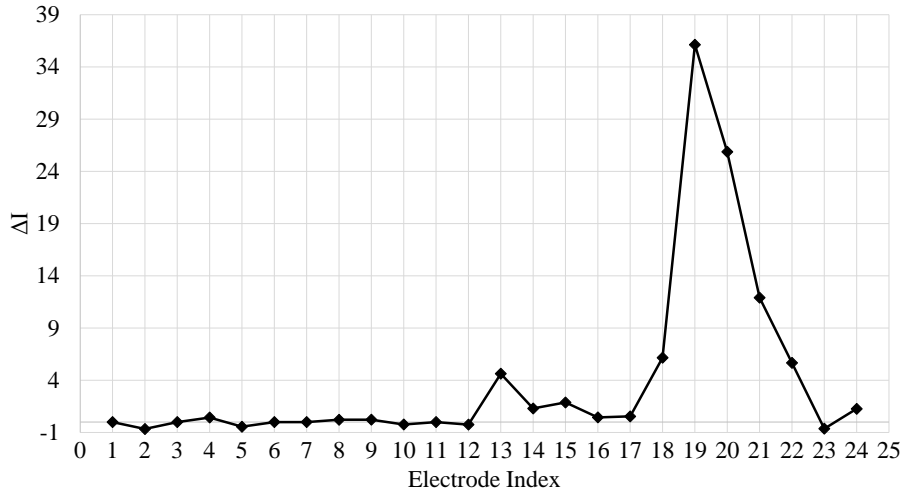


Figure 3.16: The rate of change of the intensity output vector (ΔI)

between oil and water electrodes. This makes the detection of the air-oil interface challenging using the first derivative approach especially in the presence of noise.

3.4.5 Iterative interface detection

To enhance the probability of detecting the interfaces using relative change detection methods, we introduced an iterative detection algorithm (*Get Interface*) that could be applied sequentially to extract interfaces separating different components of the multiphase mixture. This method is based on an unsupervised classification process that takes a single-dimensional array (vector) as an input and returns the index of the element (interface) that best separates its components into two homogeneous categories or classes (see Figure 3.17). It works based on finding the element that shows the largest step-change between the values of the elements located before and after it. To detect the interface element, the algorithm uses a voting process. First, a voting value for each of the elements is calculated based on the difference between the average of the elements located after and before it. Second, the index of the element with the maximum vote is selected as the interface. The equation used to calculate the votes is shown in 3.13.

$$v(i) = \mu(I(i+1 : N)) - \mu(I(1 : i)) - I(i)/2 \quad (3.13)$$

where $v(i)$ is the vote of the electrode with index i , N is the size of the input vector, I is the intensity vector, and $\mu()$ is a function that returns the arithmetic mean of its input.

After finding the interface element, the input vector is updated by removing

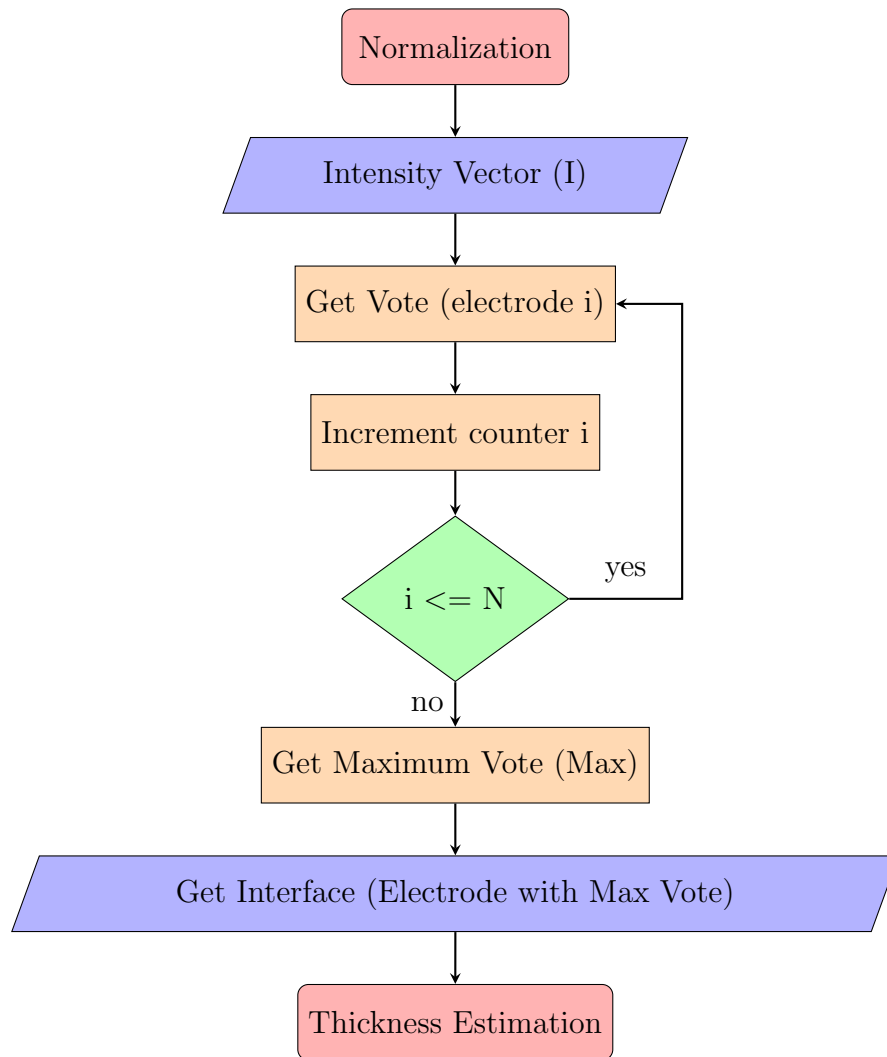


Figure 3.17: Flow chart of the *Get Interface* method

the elements of one of the detected classes; before or after the index of the interface element. Then, the same method could be applied on the updated vector to further classify the components of the remaining elements into two new classes. The method could be applied in several iterations to obtain the number of classes required in the application. For instance, in our application, two iterations were used to get the two required interfaces; first, using the original intensity vector to get the oil-water interface, and then, using the updated intensity vector to get the air-oil interface. Note that the result of the first iteration is the oil-water interface since it possess the largest step change in the input vector. Then, the input element are classified into two classes: class 1 contains the electrodes immersed in air or oil, and class 2 contains the electrodes immersed in water. The input vector is updated before applying the second iteration by removing

the oil-water interface and all of the electrodes beneath it from the input vector (water-immersed electrodes). The remaining elements are either immersed in air or in oil and the results of acquired from the second iteration include the air-oil interface, the air-immersed electrodes, and the oil-immersed electrodes.

3.5 Opportunistic filtering

This section describes the filtering methods developed to reduce the measurement error based on the dynamic conditions.

3.5.1 Dynamic conditions

A dynamic condition refers to the case where the sensor is floating on the surface of the water (*e.g.* mounted on a floating oil skimmer), and its position is continuously changing with time. In this case, the sensor continuously rises and drops in the examined liquid. A quantitative description of a dynamic condition is related to the properties of the waves. For instance, artificial waves created in testing facilities may have a height ranging from 7 to 11 cm and speed between 15 and 35 cycles per minute. These conditions are usually set to assess the performance of oil-sensing equipment while working in realistic open water environments. The developed system was tested under similar dynamic conditions while being mounted to a skimmer as described in the testing section below. It is important to note that under such dynamic conditions, the measurement of the oil thickness is challenging since the electrodes may be falsely identified between those immersed in oil and the adjacent fouled electrodes.

To allow the sensor to work under static and dynamic situations, an opportunistic signal filtering method was designed. This approach relies on sampling the collected data at some specific moments. The moments that are sought after here are the instants of time when clear detectable interfaces between different phases occur. To detect these cases, we performed several experiments where we analyzed the output of the sensor array while the sensing platform was moving vertically in and out of the multiphase mixture. A sample of the experimental results showing the output of the sensor in the form of an intensity-based image is shown in Figure 3.18. Note that the y-axis corresponds to the electrode index, and x-axis corresponds to time. Brighter intensities reflect an increase in the intensity due to water contact.

The results of the experimental analysis showed that the moments that best describe the sharp interfaces between the components of the multiphase mixture are when the sensor is at the highest points (crests) of the vertical motion. Note that when the sensor is moving downward (wave moving upward), the total average intensity increases since more electrodes are immersed in the examined liquid. In contrast, when the sensor is moving upward (wave moving downward),

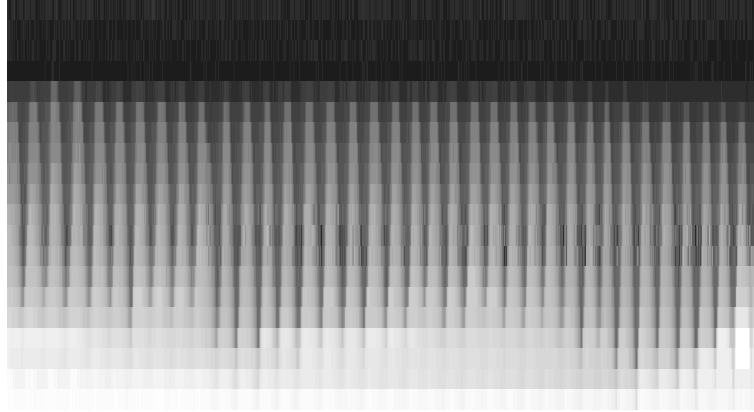


Figure 3.18: Grayscale intensity image

the total average intensity decrease. Based on this analysis, two opportunistic filtering methods were developed. These methods are explained in details in the next sections.

3.5.2 Highest point algorithm

The instants of time where the sensor is located at the highest positions of the vertical motion could be inferred by searching for the smallest intensity values recorded within a short temporal window. We refer to this approach as the *Highest Point Algorithm* presented in Figure 3.19. This algorithm starts by performing a set of consecutive measurement cycles and calculating the corresponding intensity vectors. The intensity vectors are stored in a matrix (Temporal Matrix) with a fixed size. Note that the number of columns of the matrix is equal to the size of the temporal window (T). Then, a vector containing the smallest intensity values (Min Vector) is filled and used to infer the air-oil and oil-water interfaces using the iterative interface detection method described before. The oil thickness is estimated after detecting the two interfaces (oil-water and air-oil), based on the geometrical properties of the sensor, as shown before in 3.11.

The initial experimental assessment of the system showed that the *Highest Point Algorithm (HPA)* was found to report the most accurate results for light oil types (e.g., Diesel). This result was expected because when dealing with light oils, the fouled electrodes that move from oil to air get cleaned relatively quickly, and electrodes that are fouled at the bottom side are minimal (if any). Note that this method was validated based on empirical evidence where we observed that at the highest point of the sensor movement, most fouled stripes moved upward into the oil.

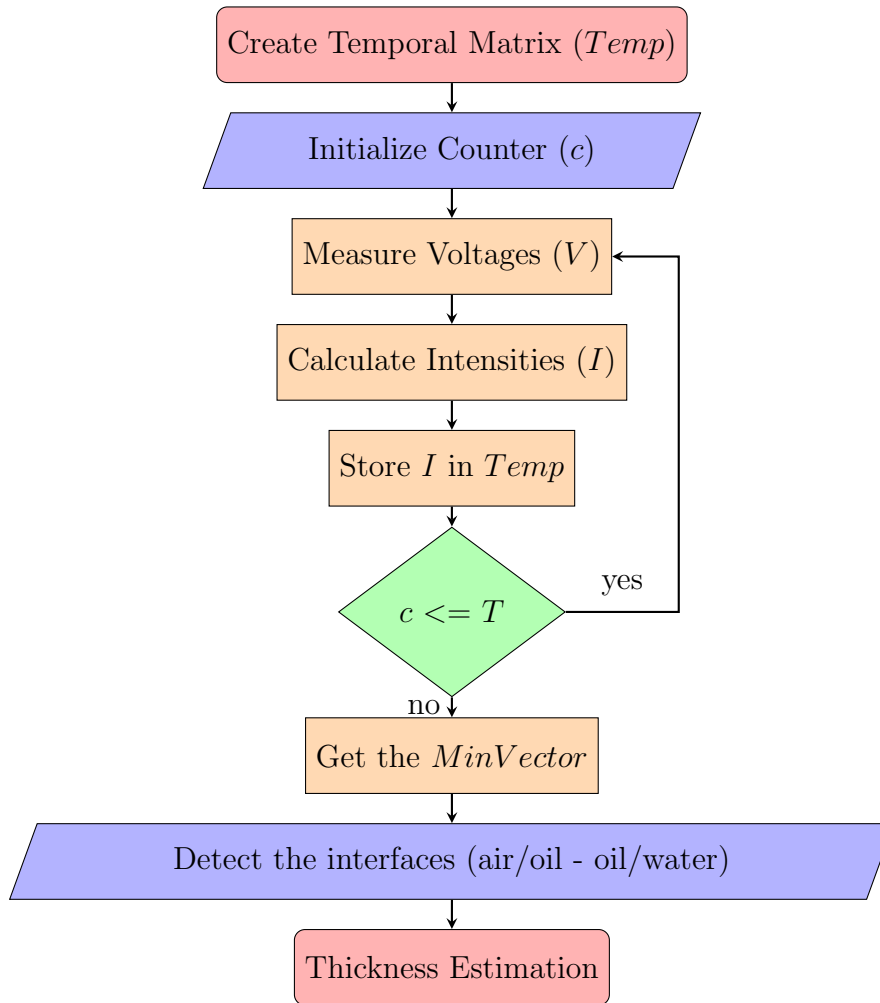


Figure 3.19: Flow chart of the *Highest Point Algorithm*

3.5.3 Corrected lowest point algorithm

When dealing with thick oils (e.g., Hydrocal, Calsol), the performance of the HPA was affected; this is because when the oil is highly viscous, it tends to stick to the strip surfaces, and it takes longer for them to get cleaned. Therefore, the optimal moments, in this case, would be when the sensor is at its lowest point of travel. In contrast, to the HPA, those moments could be detected by searching for the time instants where the sensor shows the largest intensity values. However, this method requires a correction step in which the fouled electrodes should be removed from the resulting intensity vector. This solution is referred to as the *Corrected Lowest Point Algorithm (CLPA)*. This algorithm is similar to the HPA in terms of calculating a set of consecutive intensity vectors and storing them in a temporal matrix. Then, the algorithm stores the maximum and minimum intensities in two separate vectors. A new vector is created to store the differences

between the maximum and minimum intensities; this vector is named *Amplitude* and is used later in the correction step. The method used for correction (removing the fouled electrode) is illustrated in pseudo-code in Algorithm 1.

Algorithm 1: Correction step - Corrected lowest point algorithm

Input: Max Vector, Min Vector
Output: Oil Thickness
Amplitude (K) = Max Vector (K) - Min Vector (K);
Water interface = Get interface (Max Vector);
 $m = [(\mu(\text{Max Vector}) - \mu(\text{Min Vector})) / \mu(\text{Max Vector})] \times 100$;
if ($m \geq 3$) **then**
 while (*Water interface* > 1) **do**
 if (*Amplitude (Water interface)* > $\mu(\text{Amplitude } (0: \text{Water interface} - 1))$) **then**
 Water interface = Water interface - 1;
 end
 end
end
Max Vector = Max Vector (0, Water interface - 1);
Oil interface = Get interface (Max Vector);
Oil Interval = Water interface - Oil interface;
Oil Thickness = (Oil Interval \times 2) + (Oil Interval - 1);

To decide on applying the correction step, first, the method calculates a new parameter (m) as shown in 3.14. Then, it decides on applying the correction step by comparing the indicator to a certain threshold. For instance, after performing several experiments, a threshold of 3 percent was found suitable for detecting the motion of the sensor. If the indicator is smaller than the threshold, the sensor is assumed to be in a static condition, and the thickness is calculated using the *Max Vector* only. Otherwise, the sensor is assumed in a dynamic condition, and the oil-water interface is corrected. The correction of the initially calculated oil-water interface, is done by decrementing its index until reaching a condition where the amplitude of the candidate is smaller than the average amplitude of the proceeding elements. Based on this logic, all the candidate interfaces with relatively high amplitudes, are removed from the selection process; elements with high amplitudes are considered fouled electrodes. The selected oil-water interface is the first interface having the minimum amplitude, representing the electrode located at the edge between oil and water. After correcting the oil-water interface, the method proceeds by detecting the air-oil interface and calculating the oil thickness.

$$m = \frac{\mu(\text{Max Vector}) - \mu(\text{Min Vector})}{\mu(\text{Max Vector})} \times 100 \quad (3.14)$$

where $\mu(\text{Max Vector})$ and $\mu(\text{Min Vector})$ are the averages of the maximum and minimum intensity vectors respectively.

3.6 Operational testing and results

To evaluate the performance of the implemented sensing system under operational conditions, testing was carried out at the Ohmsett facility [39] under static and dynamic conditions and using different types of heavy and light oils. This section, describes the experimental setups, procedures, and results.

3.6.1 Experimental setups

Testing was performed using two experimental setups. The first is an indoor lab setup in which quantities of oil were poured in carefully calibrated increments into a transparent glass tank (0.327 m x 0.327 m) shown in Figure 3.20. Here, four different oils were tested including Diesel, Hoops (weathered), Hydrocal 300, and Calsol 8240. Each oil was dispensed to create eight different slick thicknesses, starting from 3.175 mm to 76.2 mm. Oil thickness was increased, beginning with the oil with the lowest viscosity, by dispensing the appropriate volume using graduated cylinders. The sensor was removed from the container when oil was being added, but the sensor was not cleaned or modified between tests. The tank was emptied and cleaned between the tests using different oil types. In each experiment, the sensor was first held steady to obtain an initial static case reading, followed by a dynamic case for approximately one minute of reciprocating vertical motion; it was then followed by about one minute of lateral movement in a direction parallel to the oil slick. The equation used to calculate the desired amounts of oil is presented in 3.15. The total amounts of oil, with respect to the reference thicknesses, are shown in Table 3.1.

$$T = (V)(10^{-3})/A \quad (3.15)$$

where A is the area of the container (test area), T is the actual thickness measured in mm, and V is the oil volume measured in ml. Note that the area of the lab tank was 0.106929 m^2 . The actual thickness was confirmed visually using a ruler on the outside of the tank.

The second experimental setup is an outdoor large pool (203 m long, 20 m wide, 2.4 m deep) shown in Figure 3.21, including a wave generator capable of simulating regular waves up to one meter in height, and a tow bridge capable of towing test equipment at speeds up to 6 knots. We performed many tests while dragging the proposed instrument at three different speeds. Hydrocal 300 oil was the test oil. The sensor was tested in two different manners: first, it was attached to the movable bridge, then it was attached to a skimmer. When mounted on the skimmer, the system was tested under calm and wavy conditions.



Figure 3.20: Indoors experimental setup

Oil thickness (mm)	Oil volume (ml)
3.17	339.60
6.35	679.20
12.70	1358.40
19.05	2037.70
25.40	2716.90
38.10	4075.30
50.80	5433.80
76.20	8150.70

Table 3.1: Disposed oil amounts with actual oil thickness - Lab tank

3.6.2 Laboratory testing

The experimental results of the indoors testing (dipping tests) are discussed in this section. The actual thickness is calculated based on the geometric dimensions of the test tank, and the volume amount of the added oil. The thickness values measured by the sensor are labeled as "Average Measured Thickness (mm) – Static" for the static tests, and "Average Measured Thickness (mm) – Dynamic" for dynamic tests. The actual thicknesses are labeled as "Actual Thickness (mm)".

It is important to note that the results of the measurements displayed in the following graphs under the title "Average Measured Thickness (mm)" is the arithmetic mean of a set of measurements recorded for each thickness of the oil. The standard deviation of the recorded set of measurements indicating the precision of the results is shown in the graphs in the form of error bars. The accuracy of the



Figure 3.21: Outdoors experimental setup

measurement is calculated based on the absolute difference between the average measured thickness and the actual thickness. The accuracy of the measurements for each of the performed tests is discussed in the text after presenting the results.

Dipping tests (1-8) - Diesel

The sensor was tested using Diesel oil (viscosity 8 centipoise at 20 degrees Celsius) with a thickness ranging from 3.175 mm to 76.2 mm. Water and oil temperatures were recorded around 21.1 degree Celsius. The experimental results showing the measured thicknesses, in static and dynamic test cases, versus the actual thicknesses, are shown in Figure 3.22. Note that these results were obtained based on the *Highest Point Algorithm* developed for light-oil types (ex. Diesel – Hoops).

The results of the dipping tests performed with diesel oil showed that the absolute error of the measured thicknesses in the static case did not exceed the resolution of the sensor (3 mm) in most of the tests. In the last test (Test 8), the absolute error increased to around 6 mm where the average measured thickness was 70.41 mm, and the actual was estimated as 76.2 mm. In summary, the total average error of the static experiments was measured at 1.7 mm with five out of eight static tests showing an average absolute error of less than 1 mm. In the dynamic case, five out of the eight tests showed high accuracy, with an average absolute error of less than 1 mm. However, because of the increased dynamic motion of the sensor, the number of misclassified electrodes increased in some cases, thereby causing a higher error than in the static case, with a total average error of around 4 mm.

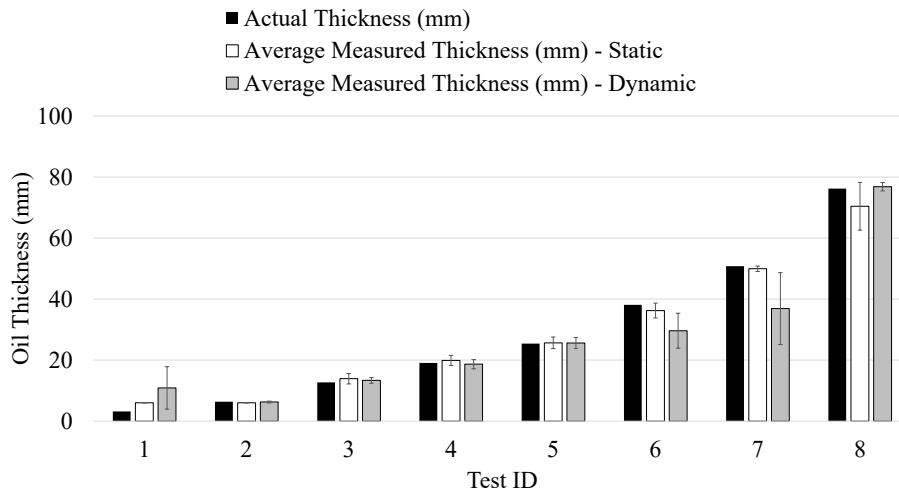


Figure 3.22: Measured vs. Actual Thickness (Dipping - Diesel)

Dipping tests (9-16) - Hoops (weathered)

Tests numbered from 9 to 16 used Hoops (weathered) oil (Viscosity 55 centipoise at 20 degree Celsius) with a thickness ranging from 3.175 mm to 76.2 mm. Water and oil temperatures were recorded around 21.1 degree Celsius. The results were obtained based on the *Highest Point Algorithm* developed for light-oil types. Figure 3.23, shows the plot of the measured thicknesses, in static and dynamic test cases, versus the actual thicknesses.

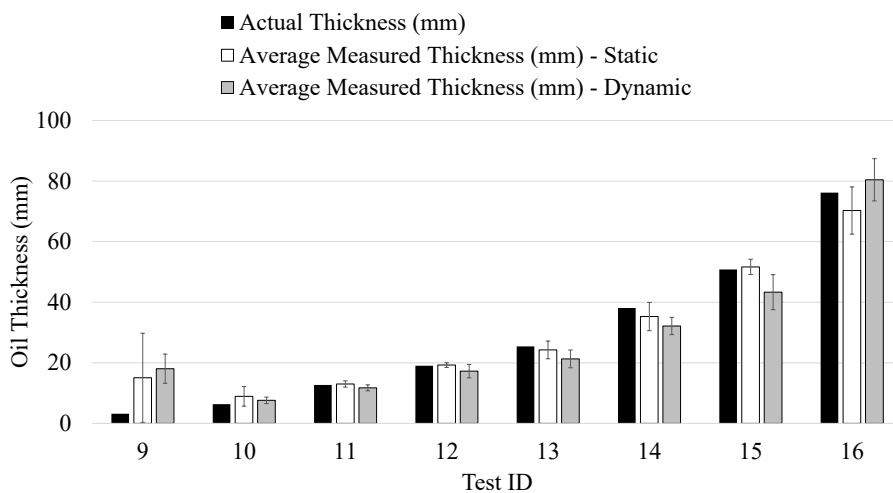


Figure 3.23: Measured vs. Actual Thickness (Dipping - Hoops)

For the static tests, three tests (11, 12, and 15) showed an extremely high

accuracy with an absolute error of less than 1 mm. The remaining tests showed an absolute error ranging from around 1 to 5 mm. The largest error occurred at the first test (Test 9), where the actual thickness is around 3.18 mm. This error is due to the oil-fouling effect. In particular, when the sensor is immersed in the liquid for the first time, most of the electrodes are covered with a layer of oil. For the dynamic test cases, the absolute error is equal to less than one electrode (3 mm) in three tests (10, 11, and 12) and less than two electrodes (6 mm) in the other three tests (13, 14, and 16).

Dipping Tests (18-25) – Hydrocal 300

Tests numbered from 18 to 25 used Hydrocal 300 oil (Viscosity 220 centipoise at 20 degree Celsius) with a thickness from 3.175 mm to 76.2 mm. Water and oil temperatures were recorded around 21.1 degree Celsius. Measurements are obtained by the *Corrected Lowest Point Algorithm* developed for heavy oils. The experimental results are shown in Figure 3.24.

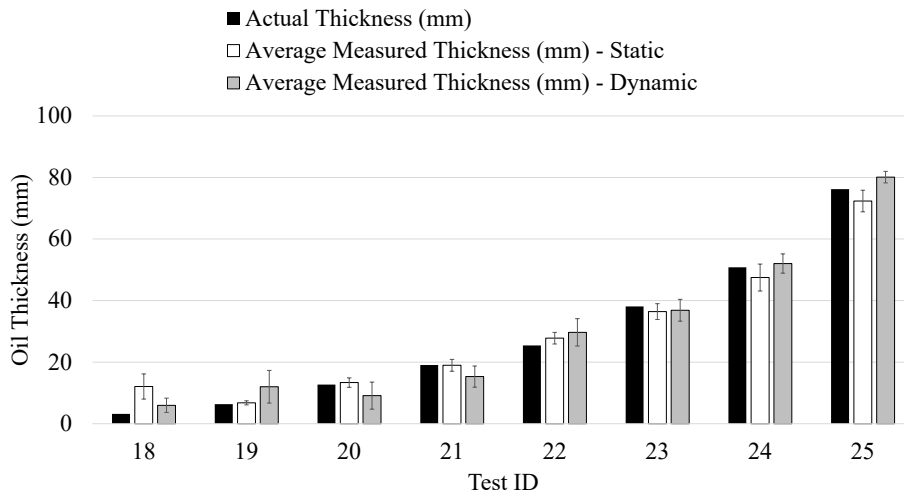


Figure 3.24: Measured vs. Actual Thickness (Dipping - Hydrocal 300)

The experimental results showed high accuracy, since all of the tests except for the first one had an absolute error of less than or around 3 mm, representing a misclassification of a single electrode. As described before, the first test with the thinnest oil thickness had the largest error due to the effect of oil fouling. In the dynamic tests, the Corrected Lowest Point Algorithm produced good results, where all of the dynamic tests showed an average absolute error ranging from 1 mm to a maximum of 5.4 mm.

Dipping Tests (26-33) – Calsol 8240

Tests numbered from 26 to 33 used Calsol 8240 (Viscosity 2653 centipoise at 20 degree Celsius) oil with a thickness ranging from 3.175 mm to 76.2 mm. Water and oil temperatures were recorded between 20.5 and 21.3 degree Celsius. Measurements are obtained by the CLPA. The experimental results are shown in Figure 3.25.

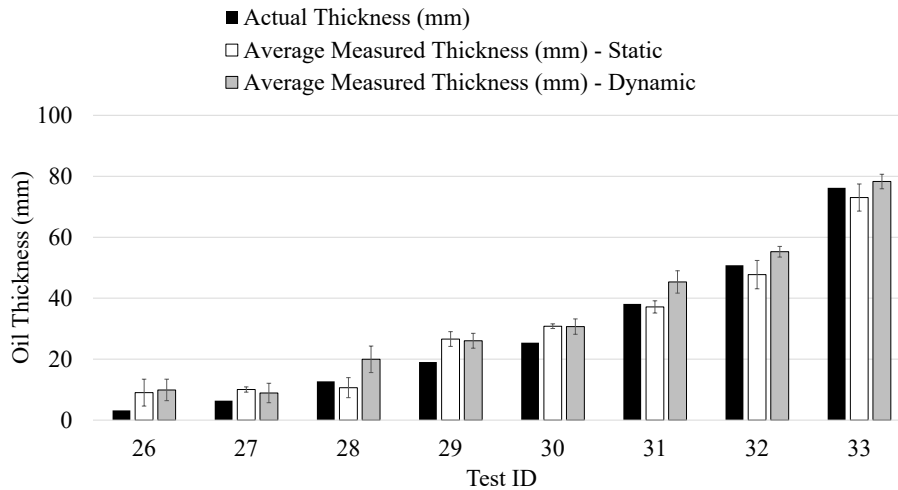


Figure 3.25: Measured vs. Actual Thickness (Dipping - Calsol 8240)

Experimental results on the Calsol 8240 oil in static and dynamic cases showed high accuracy against different thicknesses. For instance, the results of the static tests showed an absolute error ranging from 0.956 mm (test 31) to 5.823 mm (test 26). The maximum absolute error in this experiment did not exceed the misclassification of more than two electrodes. For the dynamic case, the absolute error ranges from around 2 mm to around 7 mm, representing one or two misclassified electrodes only.

3.6.3 Bridge-mounted tests

Bridge-mounted dragging tests were designed to obtain sensor data while it was dragged through surface slicks at a range of speeds that are typical when deployed onto spill response equipment, or in fast water currents. The test setup was accomplished by preparing a channel that was 0.86 m wide by 17.83 m long. The method used in performing the dynamic tests is as follows:

- Prepare defined slick thickness
- With the sensor in oil, travel at test speed, record measurements

- Stop, reverse direction, record measurements
- Repeat passes in the north and south directions (3 times)

The area of the test channel used for bridge testing is assumed constant (15.39 m^2). Specific amounts of oil were added to the channel area to obtain a set of defined slick thicknesses (estimated actual thicknesses). Similar to the procedure used in the indoors laboratory testing, the amounts of oil needed to obtain the desired thicknesses were calculated based on 3.15. The relation between the oil volume measured in ml and in gallons is shown in equation 3.16. The total volume amounts of oil added into the test channel, with respect to the reference thicknesses, are shown in Table 3.2.

$$Volume(ml) = \frac{Gallons}{0.26417} \times 10^3 \quad (3.16)$$

US Gallons (gal)	Est. Oil Volume (ml)	Actual Thickness (mm)
26	98421.47	6.35
52	196842.94	12.7
104	393685.88	25.4
208	787371.76	50.8

Table 3.2: Disposed oil amounts with actual oil thickness - Bridge testing

The test conditions for the bridge-mounted tests, including the oil thicknesses and bridge speeds, are summarized in Table 3.3. Hydrocal 300 oil (Viscosity 220 centipoise at 20 degree Celsius) was used as the test oil.

Test ID	Speed (knots)	Actual Thickness (mm)
34, 35	0.5	6.35
36, 37, 38	1	6.35
39, 40	2	6.35
41, 42	0.5	12.7
43, 44	1	12.7
45, 46	2	12.7
47, 48	0.5	25.4
49, 50	1	25.4
51, 52	2	25.4
53, 54	0.5	50.8
55, 56	1	50.8
57, 58, 59, 60	2	50.8

Table 3.3: Test cases for bridge-mounted testing

As shown in Table 3.3, relatively large thicknesses of oil (greater than 25 mm) were tested. Note that these thicknesses are intended to emulate realistic operational conditions where the oil is collected using specific booms to facilitate the cleaning procedure using skimmers. Under free-floating conditions, oil slicks show thin layers with thicknesses ranging from smaller than 1 mm to about 3 mm. However, since our system is designed to operate in oil-cleaning applications, it was tested against thick layers of oils as described below.

It is important to note that in the last set of tests (tests 53 to 60), due to wind effects, the contained slick was stacked more on one side of the channel. Consequently, the slick target thickness was skewed to a lesser thickness due to the boom bellying outward and thereby increasing the surface of the test area. In particular, the theoretically calculated thickness is around 50.08 mm but the actual thickness as measured by a manual tool (visual assessment on a graduated see-through container dipped in the oil) is around 38 mm.

Figure 3.26 shows the sensor mounting setup with the sensor, boom attached bracket, and channel. Measurements were obtained by the CLPA algorithm. Figure 3.27 plots the average measured thickness in comparison to the actual thicknesses. Error bars, based on the standard deviation of the set of recorded measurements, are shown for each average measurement.



Figure 3.26: Capacitive sensing system mounted to the moving bridge

The experimental results of the bridge-dragging tests shown in Figure 3.27 showed an average absolute error ranging from 0.313 mm to 7.1 mm. However, most of the tests showed an absolute error of less than 6 mm; representing the misclassification of fewer than two electrodes out of forty-eight electrodes. It is obvious that for the last three tests, numbered from 53 to 60, where the actual estimated thickness was 50.08 mm, the largest absolute error occurred. However, for this case, and based on the notes provided by Ohmsett staff, the slick target thickness was skewed to a lesser thickness due to the boom bellying outward,

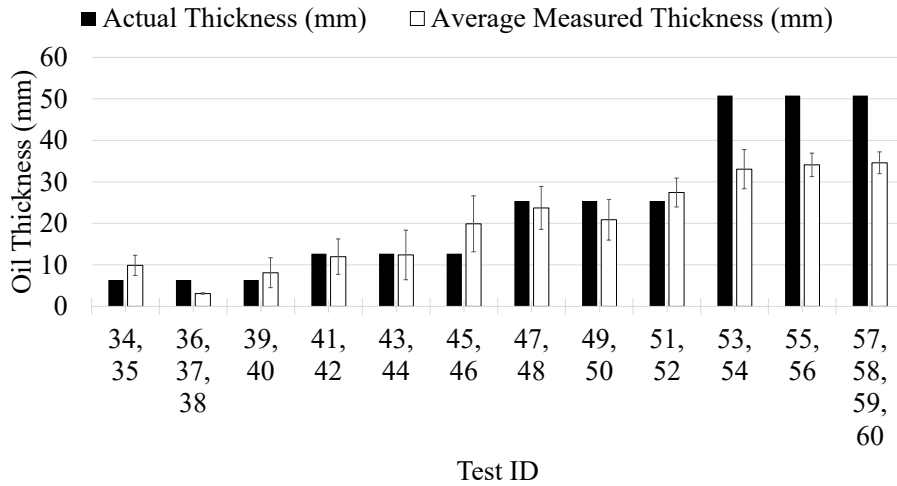


Figure 3.27: Measured vs. Actual Thickness (Hydrocal 300) – Bridge

thereby increasing the surface area. To represent the ground truth value more accurately, the oil thickness was measured using a manual tool at 38.1 mm. Based on this fact, and by assuming that the 38.1 mm is the actual thickness, the absolute average error in these tests ranges between 4 to 5 mm.

3.6.4 Skimmer-mounted tests

The purpose of this set of tests is to assess the performance of the sensing system when mounted on a typical skimmer during operation in a wavy environment. The system was tested against different wave conditions and while traveling slowly into and against the waves. The test setup consisted of a boomed area along the test basin west wall measuring 3.04 m x 9.14 m. The system was rigidly mounted to the frame of the *Desmi Termite* skimmer and positioned between two of the floats, and in front of the skimming weir. Prior to testing, the skimmer was placed into the test basin, and the sensor height was adjusted such that the waterline was near the center of the measurement range. Figure 3.28 shows the sensor mounted on the skimmer in the test area. Waves with different properties were generated using the wave generator available in the outdoor testing setup. The experimental conditions and the properties of the generated waves are discussed below.

The experimental procedure followed while executing the skimmer-mounted tests is summarized by:

- Prepare defined slick thickness (constant 76.2 mm) in the test area by adding the proper volume of oil
- Mount the sensor on the skimmer via sensor brackets

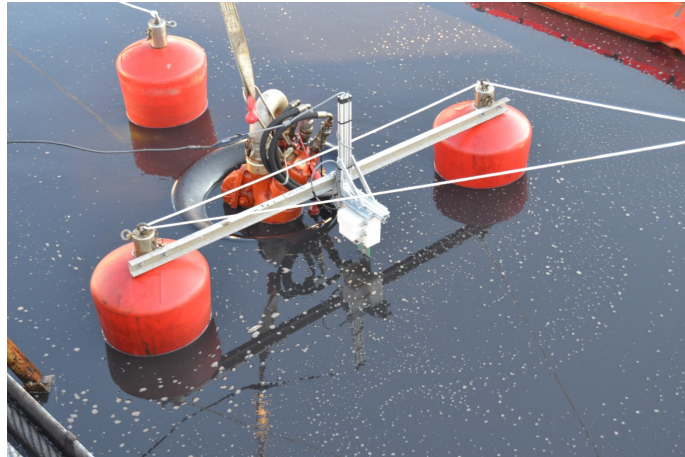


Figure 3.28: Capacitive sensing system mounted on a skimmer

- Lower the skimmer into the test area while tethered via control ropes to external bridges
- Establish initial sensor position relative to oil with the skimmer in water
- Obtain stationary readings
- Begin wave condition, run test while manually dragging the skimmer in the test area

The experimental conditions of the skimmer-mounted tests including the wave settings and time periods are shown in Table 3.4. The properties of the generated waves include the wave height in inches and the number of wave cycles per minute (cpm). The experimental results are shown in Figure 3.29.

Test ID	Start Time	End Time	Wave Setting
1	10:51:00	11:03:16	wave started, 15cpm, 3"
2	11:05:39	11:14:59	wave increased to 25cpm, 3"
3	11:18:24	11:20:55	wave changed to 25cpm, 4.5"
4	11:21:06	11:23:58	wave changed to 35cpm, 4.5"
5	11:26:24	11:37:21	wave stopped

Table 3.4: Wave conditions for skimmer-mounted tests

The experimental results of the skimmer-mounted tests showed an average absolute error of around 8 mm in the first two test cases. The error increased to around 10 mm when the amplitude of the waves increased to 4.5" in the third test case. In the last two test cases, the average error was reduced with the stopping of waves. It is important to note that despite the fact that the sensor accuracy

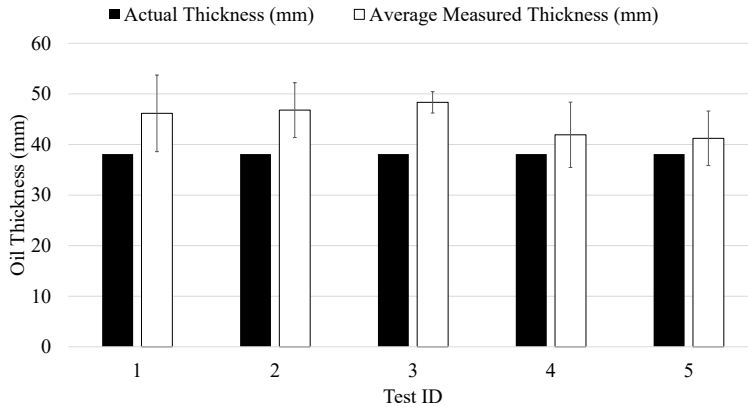


Figure 3.29: Skimmer-mounted tests – Experimental results

was affected by the presented wave conditions, the absolute average error in terms of the sensor resolution was considered acceptable (10 mm = 3 electrodes). It is also worth mentioning that in highly dynamic conditions, it is very challenging to ascertain the ground truth of the oil thickness.

3.7 Conclusion

In this chapter, we described the design, implementation, and testing of a sensing system for measuring the oil slick thickness in-situ and in real-time. The proposed system is based on a self-capacitance sensor array that works based on a geometrical sensing principle. This principle allows the sensor to work without relying on field calibration. By detecting the interface layers separating air, oil, and water, the system can measure the thickness of different types of oil and under different environmental conditions. Operational testing showed very good accuracy in the indoor setup, where the average absolute error ranged from less than 1 mm to around 5 mm in the worst-case scenario (dynamic motion). Also, the system showed good accuracy during the bridge-mounted and skimmer-mounted tests, where the average absolute error ranged from less than 5 mm to around 10 mm in worst-case scenarios (aggressive harbor chop waves).

Chapter 4

Dual-modality sensing system

This chapter describes the design, implementation, and testing of a dual-modality ultrasonic/capacitive sensing system for measuring the oil slick thickness under open water conditions. This system was developed based on the conclusions obtained from the operational testing of the self-capacitance sensor array presented in the previous chapter. It was identified that there is a need for two different sensing devices optimized for different applications; a hand-held device and a skimmer-mount device. The first hand-held device is intended for measuring the oil slick thickness in two main scenarios: (1) for experimental ground truth to verify oil thickness measurements during experiments at testing facilities such as *Ohmsett*, (2) for use from on-board vessels to obtain sample measurements in the field. The second skimmer-mount device is optimized for mounting on skimmers, buoys, or in an oil spill boom apex to provide thickness data under field conditions.

4.1 Proposed sensing approach

This section describes the main principles of the proposed sensor fusion approach for measuring the oil thickness.

4.1.1 Sensor fusion

Sensor fusion is a term used to describe the process of combining data from different sensors in order to measure a physical quantity. Generally, the principle of sensor fusion could be applied in three ways: competitive, cooperative, and complementary. Competitive (also known as redundant) sensor fusion represents the case where every sensor independently measures the same physical quantity. In cooperative fusion, data from a set of independent sensors is combined to achieve information that is not possible to achieve using the data obtained from a single sensor. In complementary fusion, sensors do not depend on each other

directly but their measurements could be combined to give a complete view of the measured physical quantity.

Our proposed sensing principle combines two categories of fusion methods. First, to estimate the water-level, we use a cooperative fusion strategy by analyzing the changes of the voltages measured at all of the sensing units. Note that information about the water-level could not be obtained using a single capacitive sensing unit. In addition, we use complementary fusion to deduce the oil thickness. The complementary approach is applied by combining the information obtained from the capacitive sensor array (oil-water interface) and the information obtained from an ultrasonic sensor (air-oil interface) to calculate the target oil thickness.

It is important to note that the combination between the ultrasonic sensor measurements and the capacitive sensor measurements is essential to circumvent the limitations of the two sensing modalities. For instance, the ultrasonic sensor is limited to measuring the liquid level and cannot be used to differentiate between oil and water layers. Thus, it is used to detect and track the upper interface of the oil phase known as the air-oil interface. Similarly, the capacitive sensing technique has a limitation when trying to differentiate between air and oil layers due to the small difference in the relative permittivity of the two insulating materials. Thus, the capacitive sensor array is used to detect and track the oil-water interface which could be detected easily due to the high conductivity of the water. Given the air-oil interface from the ultrasonic sensor and the oil-water interface from the capacitive sensor, the oil thickness could be easily calculated based on the geometrical properties of the electrodes as described before.

4.1.2 Dual-modality sensing

The proposed sensing approach is applied using a dual-modality sensing system combining an ultrasonic sensor to measure the liquid level and a capacitive sensor array to measure the water level. The measurements of the two sensors are fused complementarily to infer the oil thickness as illustrated in Figure 4.1. In particular, the partition of the capacitive sensor array immersed in air (Air section) is derived from the ultrasonic sensor measurements. The partition of the capacitive array immersed in the liquid (Liquid section) is obtained by subtracting the air-immersed section from the total length of the capacitive sensor array (sensing range). Note that the liquid-immersed section is the sum of the thicknesses of the oil and water phases. Thus, the oil thickness could be deduced given the water level. To detect the water level, the capacitive sensing cells are classified into oil-immersed and water-immersed classes. After detecting the water-immersed cells, the water level is calculated based on the geometrical dimensions of the sensors array.

The capacitive sensing cells emit a set of signals that could be used to indicate the type of material surrounding them. For instance, these signals could be

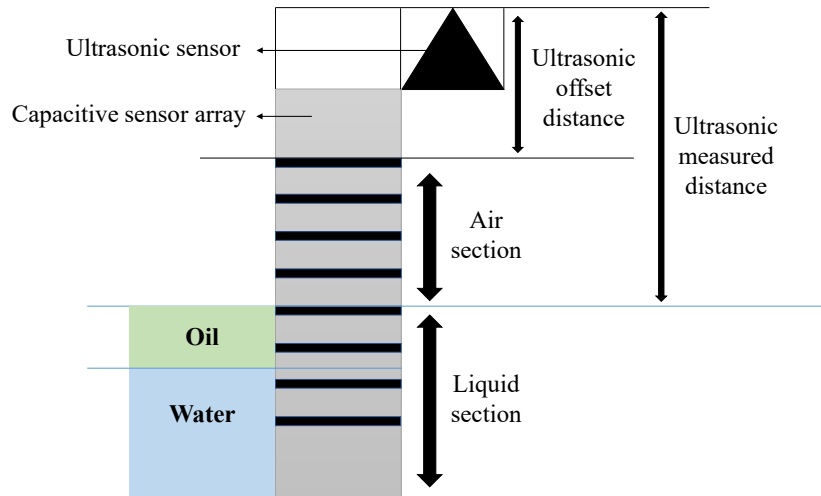


Figure 4.1: Sensing principle of the dual-modality system

compared against predefined thresholds to infer the types of material contacting the sensor cells. However, the threshold-based detection method may not work accurately under dynamic and fast-changing liquid conditions due to the transient response of the signals; when a sensing cell moves from one phase to another, the change in the output signal is not immediate and requires some time to be significant. To solve this problem, we propose a machine-learning-based classifier that relies on the shape of the output signal, instead of its absolute value, to infer the type of material contacting the sensing probes. The proposed classifier is trained using a set of labeled signals obtained through an experimental procedure designed for this purpose.

4.1.3 Sensing parameters

In what follows, we describe the main sensing parameters used to extract the oil thickness.

Ultrasonic offset distance

The ultrasonic offset distance represents the distance between the ultrasonic sensor, mounted above the capacitive sensor board, and the top edge of the first cell included in the capacitive sensor array (see Figure 4.1). This distance could be measured in real-time through a calibration procedure. The calibration procedure is simple and is applied by immersing the sensor in any liquid while recording the distances measured by the ultrasonic sensor. The ultrasonic offset distance is calculated based on the ultrasonic measured distance and the dimensions of the

capacitive sensor as shown in 4.1.

$$Offset = Measured - [(I_L - 1)(W + G)]; \quad (4.1)$$

where I_L is the index of the first capacitive unit immersed in the liquid, W is the width of the electrodes, and G is the vertical gap between the electrodes. Note that if the first electrode is immersed in the liquid ($I_L = 1$), the offset distance is equal to the measured ultrasonic distance.

Air section

The *Air section* represents the length of the sensor immersed in air. This parameter is obtained by subtracting the measured ultrasonic distance from the ultrasonic offset distance as shown in 4.2. Practically, this calculation is performed in short temporal windows where several consecutive measurements are made by the ultrasonic sensor. Thus, the *Measured* parameter represents the average of a number of distances measured by the ultrasonic sensor within a certain interval of time.

$$Air\ Section = Measured - Offset; \quad (4.2)$$

Sensing range

The total length of the capacitive sensor array is referred to as the *Sensing Range*. It is calculated based on the count and dimensions of the sensing cells as shown in 4.3.

$$Sensing\ Range = (N)(W) + (N - 1)(G); \quad (4.3)$$

where N is the total number of electrodes, W is the width of the electrodes, and G is the vertical gap between the electrodes.

Liquid section

The *Liquid Section* represents the length of the sensor immersed in the multiphase mixture. This parameter is obtained by subtracting the *Air Section* from the *Sensing Range* as shown in 4.4.

$$Liquid\ Section = Sensing\ Range - Air\ Section; \quad (4.4)$$

Oil thickness

The oil thickness is the output of the system and could be deduced after knowing the water level. The water level is detected using a machine-learning-based

classifier designed to classify the liquid-immersed cells into water-immersed or oil-immersed cells. After detecting the water level, the *Oil Thickness* is calculated by subtracting the water level from the *Liquid Section* as shown in 4.5.

$$Oil\ Thickness = Liquid\ Section - [(N_w)(W) + (N_w - 1)(G)]; \quad (4.5)$$

where N_w represents the number of sensing cells classified as water-immersed, W is the width of the electrodes, and G is the vertical gap between the electrodes.

4.2 Capacitive sensor design optimization

The capacitive sensor array used in the dual-modality system is similar to the one introduced in the previous chapter in terms of the design concept (distributed sensing cells) and sensing method (single-electrode mode). However, in this system, the capacitive sensor array is used mainly to infer the water level (oil-water interface) since the oil level (air-oil interface) is detected by the ultrasonic sensor. Based on this, the main target of the sensor array is to detect the differences between insulating materials (air, oil) and conductive material (water). By minimizing the area of the electrodes, the conductivity of a material plays the major role in causing a change in the voltage of the sensing cells. This makes the differentiation between the air and oil phases challenging using the output of the capacitive sensor array but is not considered a problem since the air-oil interface is detected using the ultrasonic sensor. Based on this interpretation, we can say that minimizing the area of the electrodes contributes to mitigating the oil fouling problem and converts the sensor array from being capacitive to relying on resistance variations (conductive) since it targets the detection of the water level.

In this study, we performed several simulations and experiments considering different shapes of coplanar electrodes and pins. The overall result of this study is to select a new design for the sensor electrodes that maximizes the sensor's ability to differentiate between oil and water. This is considered a key factor for allowing the sensor to mitigate the oil-fouling problem. In what follows we analyze the various design variables, as well as the parameters used for evaluation.

4.2.1 Design variables

In a coplanar capacitive sensor, the measured capacitance depends on a set of variables including the geometrical and structural properties of the electrodes, the Material Under Test (MUT), the substrate material, and the type of shielding [40]. The geometrical features of the electrodes include their length, width, thickness, and shape. The size of the gap between the electrodes is another important feature that impacts the penetration depth of the sensor. The properties of the MUT and the substrate include the relative permittivity, conductivity, and

geometrical dimensions. Another factor that impacts the behavior of the sensor is the shielding used to shape the electric field. One widely used type of shielding, known as passive shielding, is applied by surrounding the sensing electrodes by conductive material connected to the system ground.

4.2.2 Evaluation parameters

A set of parameters were used to evaluate the performance of the capacitive sensor relative to different design variables. These parameters include the sensitivity, dynamic range, and penetration depth.

Sensitivity

Sensitivity is defined as the ratio between the change in the measured capacitance and the change in the dielectric constant, and is calculated as shown in 4.6.

$$S = \frac{C - C_{min}}{\epsilon_r - \epsilon_0}, \quad (4.6)$$

where C is the measured capacitance, C_{min} is the base capacitance (also known as the standing or parasitic capacitance), ϵ_r is the relative permittivity of the MUT, and ϵ_0 is the relative permittivity of free space.

Dynamic range

The measured capacitance is a function of the base capacitance and the dynamic capacitance (also known as the sensor capacitance). The base capacitance, measured when no MUT is present, is caused by the circuit components, connection tracks, and the dimensions of the electrodes. On the other hand, the dynamic capacitance is the capacitance caused by the presence of the MUT. Usually, the value of the base capacitance is much larger than that of the dynamic capacitance. The dynamic range represents the interval within which the capacitance changes based on the properties of the MUT. It is important to note that minimizing the base capacitance is desirable to increase the dynamic range. Computationally, the dynamic range is obtained by calculating the difference between the maximum and minimum measured capacitances, respectively C_{max} and C_{min} .

Penetration depth

The penetration depth (PD) is defined as the distance along the z-axis (perpendicular to the surface of the PCB) required for measuring a detectable change in the output capacitance. Usually, a threshold of 3% of the dynamic range is used to detect the penetration depth. Practically, the penetration depth is identified by gradually moving away (lifting) the MUT from the surface of the sensor (along the z-axis), and recognizing the distance where (4.7) is satisfied.

$$PD = \frac{C - C_{min}}{C_{max} - C_{min}} \leq 3\% \quad (4.7)$$

4.2.3 Design options

In order to identify the optimum design, we considered several different design alternatives. Table 4.1 presents the three different options we considered, including the coplanar parallel design, the interleaved, and the concentric.



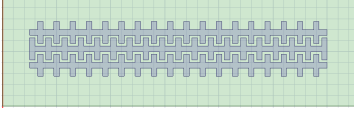

Design	Drawing
Parallel	
Interleaved_1 (N=9)	
Interleaved_2 (N=18)	
Concentric	

Table 4.1: Design alternatives, including parallel, interleaved with N= 9, interleaved with N= 18, and concentric

Parallel rectangular blocks

The coplanar parallel design includes electrodes shaped as rectangular blocks. For the sake of analysis, a single sensing cell was considered, composed of three coplanar electrodes mounted on the top surface of a PCB. The central electrode is used for excitation and measurement, and the two adjacent electrodes are used for shielding (connected to 0 V). In the simulations, the separation gap was set to different values (0.5 mm, 1 mm, 1.5 mm, and 2 mm). The width of each electrode is set to 2 mm and the length is set to 55 mm. The PCB is made from $FR4_{epoxy}$ material with a dielectric constant of 4.4. The PCB dimensions are: 20 mm x 65 mm x 1.6 mm. The electrodes are made of copper, with a thickness of 0.05 mm. In all simulations, the sensor was placed at the center of a 3D box composed of air with a relative permittivity of one.

Interleaved and concentric

To assess the effect of different separation gaps on the response of the sensor, two different interleaved designs were considered. The first design includes 9 elements ($N=9$), with a width of 2 mm ($W=2$ mm), and a separation gap of 1 mm ($G=1$ mm). The second design includes 18 elements with a width of 1 mm each, and a separation gap of 0.5 mm. In the concentric design, two concentric electrodes are laid with a width of 2 mm and a separation gap of 1 mm. The inner electrode is used for excitation and measurement, and the outer electrode is used for shielding (connected to 0 V). The PCB material and dimensions, electrodes material and thickness, and region of the simulation are identical to the ones of the rectangular blocks described above.

4.2.4 Assessment via simulations

Finite element simulations were performed to characterize different coplanar sensor designs and to assess their performance relative to the evaluation parameters introduced above. The simulations were applied using the Maxwell package included in the ANSYS 19.0 software.

Thickness-sweep simulations

The thickness sweep simulations aim to study the sensitivity and the dynamic range of the sensors. The MUT is made of silicon dioxide with a relative permittivity of 4. The thickness of the MUT (placed at the top surface of the sensors) was changed gradually from 0 mm to 5 mm with increments of 0.2 mm. An excitation of 2 V was applied at the center electrode and that of 0 V to the adjacent electrodes; for all designs, the capacitances are measured at the center electrode. Table 4.2 reports the different metrics for all simulated designs, including values for dynamic range (DR), minimum measured capacitance (Min.C), maximum measured capacitance (Max.C), and the average sensitivity (AS). Based on the results of the simulations, we note the following:

- In all designs, the measured capacitances increased with the increase of the MUT thickness (Figure 4.2). After reaching a certain thickness, the measured capacitance saturates, indicating that a maximum penetration distance of the electric field is reached.
- For the parallel designs (rectangular blocks), the base capacitance, measured when MUT thickness is equal to zero, increased as the separation gap decreased. This result was expected since the separation gap is inversely related to the output capacitance. It is important to note that the increase in the base capacitance is not desired because it reduces the interval available for measuring the dynamic capacitance, changes of the output capacitance caused by the presence of the MUT.

- As shown in Figure 4.3, the sensitivity of the parallel sensors increased as the separation gap decreased. The concentric and the first interleaved (N=9) sensor showed a similar behavior in terms of sensitivity and dynamic range. The second interleaved design showed a larger base capacitance, larger dynamic range, and increased sensitivity.

Simulated Designs	Simulation Results			
	<i>Min. C (pF)</i>	<i>Max. C (pF)</i>	<i>DR</i>	<i>AS</i>
Parallel (G= 0.5 mm)	6.78	11.02	4.23	0.92
Parallel (G= 1 mm)	4.49	7.29	2.79	0.69
Parallel (G= 1.5 mm)	3.68	5.97	2.28	0.6
Parallel (G= 2 mm)	3.24	5.39	2.15	0.53
Interleaved (N= 9)	3.97	6.51	2.54	0.69
Interleaved (N= 18)	6.99	11.48	4.48	1.28
Concentric	4.05	6.97	2.91	0.69

Table 4.2: Results for thickness-sweep simulations

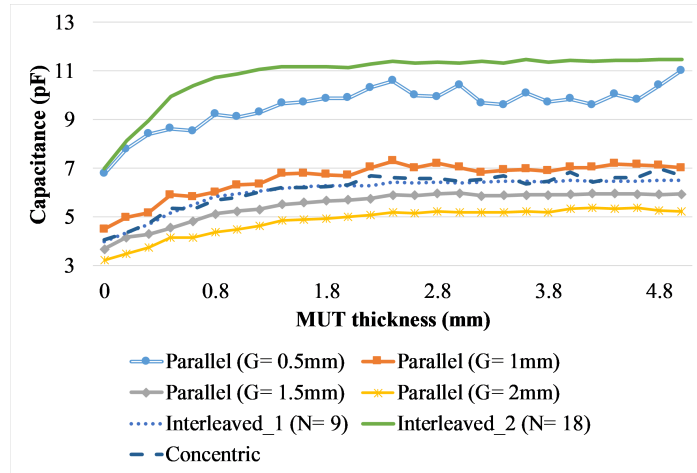


Figure 4.2: Capacitance (pF) vs. MUT thickness (mm)

Backplane shielding

To assess the impact of adding a conductive backplane, acting as a passive shield to the electrodes, a copper sheet with a thickness of 0.05 mm and a surface area identical to that of the PCB was attached to the bottom side of the PCB. The excitation was set to 2 V for the central electrode and 0 V for the adjacent

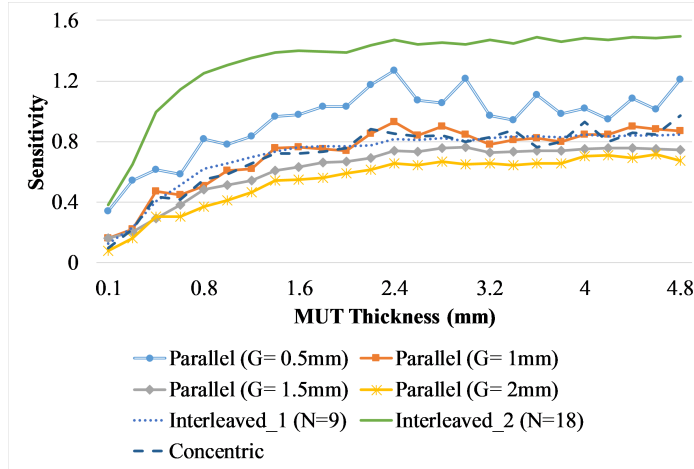


Figure 4.3: Sensitivity vs. MUT thickness (mm)

electrodes and the backplane sheet. The magnitude of the electric field, with and without shielding, is shown in Figure 4.4.

The magnitude distribution of the electric field showed that when no backplane is present, the electric field penetrates the PCB and propagates through its bottom side. This result validates that proper shielding is needed to isolate the sensing electrodes and the connection tracks from unwanted sensing regions. On the other hand, it was noted that the magnitude of the electric field along the z-axis (in front of the PCB) is decreased. The base capacitance of the sensor increased after adding the backplane.

Lift-off simulations

The lift-off simulations aim to study the penetration depth of electric fields of the sensors. These simulations were performed by setting the thickness of the MUT to a constant value (10 mm), and changing its vertical position (lift-off distance) along the z-axis from 0 mm to 20 mm with increments of 0.2 mm. The capacitances measured at the central electrode relative to different lift-off distances are shown in Figure 4.5. Simulations showed that the measured capacitances decreased exponentially with the increase in the lift-off distance. The penetration depths calculated based on the lift-off simulations are shown in Table 4.3.

The results of the lift-off simulations showed that, for all designs, the capacitances decreased exponentially while the position of the MUT was increased along the z-axis. The penetration depths showed that the second interleaved design, which has the largest sensitivity, provided a limited penetration depth of around 1 mm. This result validates that the sensitivity of the coplanar sensor is inversely related to its penetration depth.

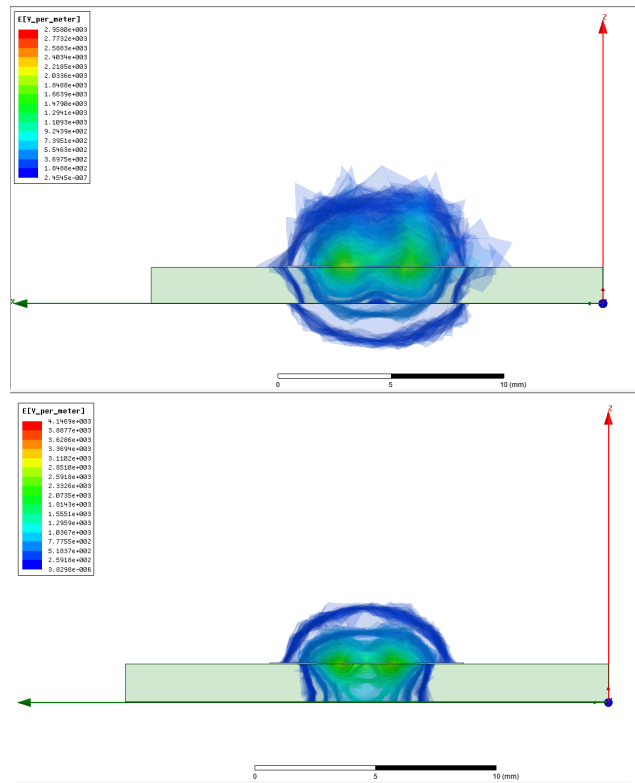


Figure 4.4: Magnitude of the electric field – Top: Without a backplane. Bottom: With conductive backplane connected to 0V

Lessons learned from simulations

The simulations showed that decreasing the separation gap and increasing the number of leaves in a co-planar sensing cell, increases the sensitivity of the sensor. Increasing the sensitivity is desired because it improves the ability of the sensor to differentiate between materials with comparable dielectric constants, such as oil and air. However, for the application of oil thickness measurement, extending the penetration depth is essential in order to mitigate the oil-fouling problem. In order to enhance the penetration depth while maintaining high sensitivity, one solution is to increase the area of the electrodes. Unfortunately, increasing the overall width of the sensing cell is not possible due to the relatively small geometric design constraint of minimum measured thicknesses. Because of the fact that in all coplanar designs we observed an oil-fouling layer that was much thicker than the penetration depth, the use of coplanar sensing cells is not expected to mitigate the oil-fouling problem. As a result, we propose to use a parallel-plate structure design as will be detailed next.

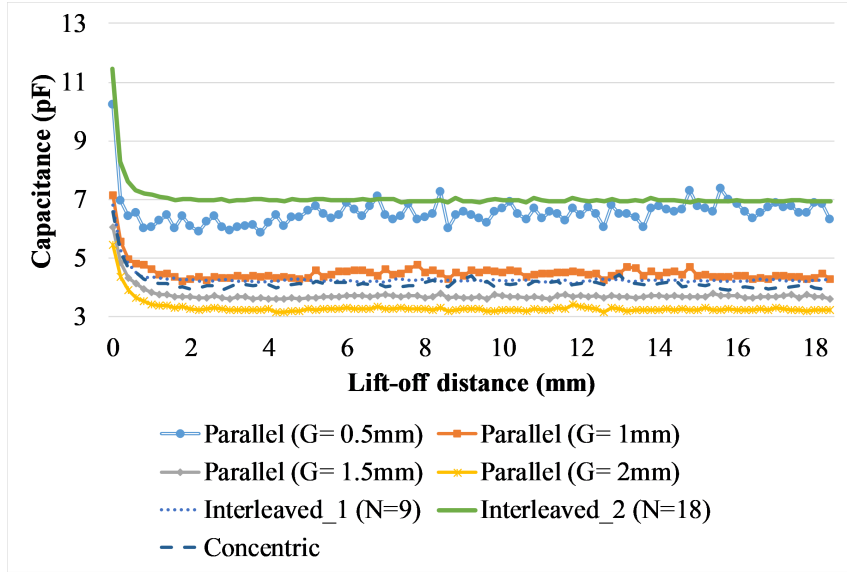


Figure 4.5: Capacitance (pF) vs. lift-off distance (mm)

Simulated Designs	Pen. Depth (mm)
Parallel (G= 0.5 mm)	0.8
Parallel (G= 1 mm)	1.6
Parallel (G= 1.5 mm)	1.6
Parallel (G= 2 mm)	2.2
Interleaved (N= 9)	1.8
Interleaved (N= 18)	1.2
Concentric	1.6

Table 4.3: Penetration Depths

4.2.5 Proposed design

The proposed design uses a set of needle-like pins as structure that can penetrate the oil-fouling layer and focus the electric field towards the target area along the z-axis. In what follows, we investigate in a systematic manner the changes caused by adding the pins to the coplanar electrodes used before, and the modifications required to increase their effectiveness.

Analysis of the effect of adding pins

In this set of simulations, we study the effect of the pins added to the coplanar sensor design presented in the previous chapter. The 3D model represented a single cell, and the magnitude of the electric field is shown in Figure 4.6.

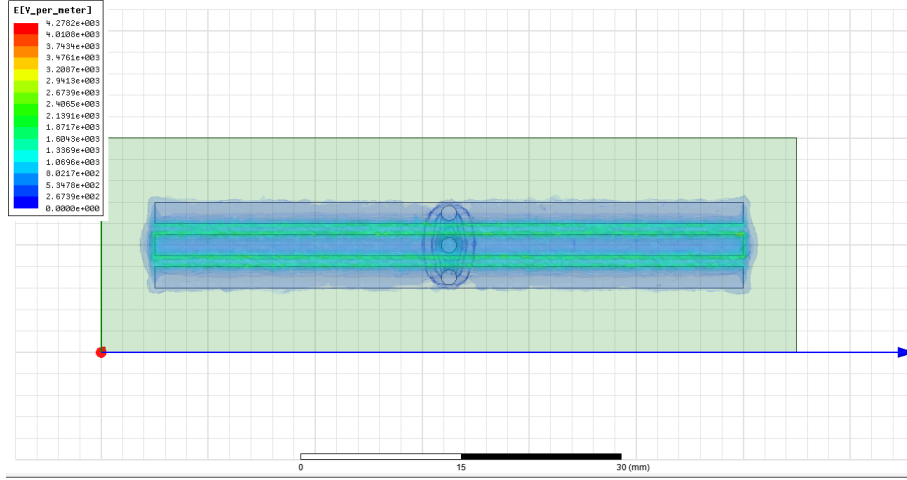


Figure 4.6: Magnitude of the electric field - Initial sensor with pins (front view)

In order to obtain the basic distribution of the electric field, the first simulation was completed without adding any material to the surface of the sensor. Three cylindrical pins were added to the center of the co-planar electrodes (rectangular blocks, width= 2 mm, gap= 1 mm), each having a diameter of 1 mm and a length of 10 mm. The pins were united at their base electrodes and excited in the same manner as above. The result of this simulation showed that the electric field was denser near the surface of the PCB. This is because the coplanar electrodes possessed a much larger surface area than the pins, and the gap between them (1 mm) was smaller than the gap separating the pins (2 mm). The result revealed a limited contribution of the pins in the initial design in extending the penetration depth.

To plot the response of the sensor relative to different MUT thicknesses, a thickness-sweep simulation was performed, where the thickness of the MUT placed at the surface of the PCB was increased from 0 mm to 15 mm, with increments of 0.2 mm. The measured capacitances versus the MUT thicknesses are shown in Figure 4.7. The result of the thickness-sweep simulation revealed that the rate of capacitance change (sensitivity) was high near the surface of the PCB (MUT thickness less than 1 mm), and decreases afterward.

Proposed sensing cells

Based on the analysis of the initial design, we concluded that in some applications where enhancing the penetration depth is essential, removing the coplanar electrodes is recommended to focus the electric field along the z-axis. For this purpose, we removed the coplanar electrodes, and designed a new set of sensors that uses normally-mounted pins as sensing probes. The working principle of these sensors is based on the basic concept of a parallel-plate capacitor. Note

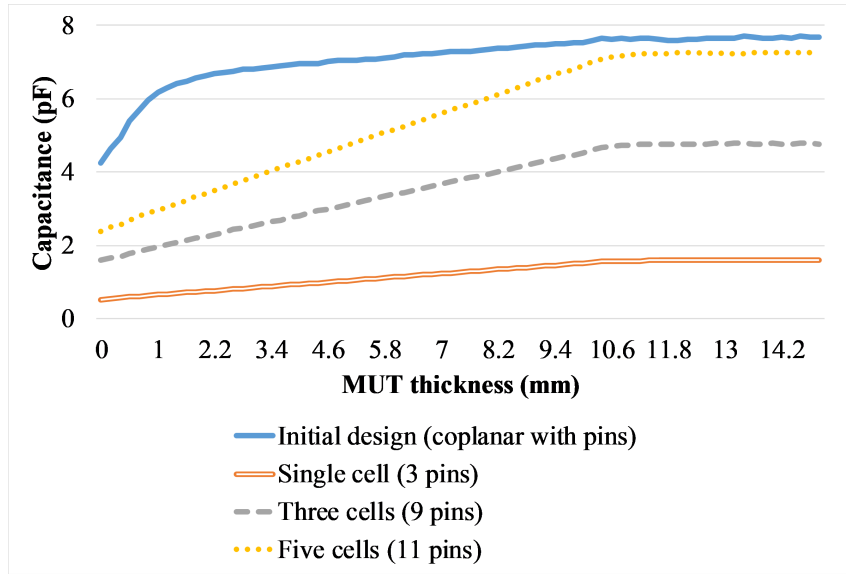


Figure 4.7: Capacitance (pF) vs. MUT thickness (mm)

that the sensing pins are guarded horizontally by two conductive pins, connected to the system ground. The center pin acts as the first plate of a capacitor, and the adjacent electrodes as the second plate; the filling material represents the dielectric. In the case of conductive liquids, such as sea water, the pins are actually shorted out. In case of non-conductive material, such as oil and air, measuring the capacitance at the center pin would be useful to identify the type of the material.

To evaluate the proposed design, three sensors were designed and assessed via simulations. The first one included a single sensing cell, the second one is composed of three sensing cells, separated horizontally by a distance of 5 mm, and the third sensor is composed of five sensing cells. The 3D models representing the three sensors are shown in Figure 4.8, Figure 4.9, and Figure 4.10 respectively.

The first simulation was performed without adding any material to the surface of the sensors, and revealed that the magnitude of the electric field was more focused along the body of the pins (along the z-axis), and almost removed from the bottom layer of the PCB (unwanted sensing area). To validate this interpretation, three identical thickness-sweep simulations were performed. The capacitances measured relative to the MUT thicknesses are shown in Figure 4.7. The results showed a linear relation between the measured capacitance and the thickness of the MUT, and indicated that removing the coplanar electrodes contributed to directing the sensor's sensitivity from the surface of the PCB to the body of the sensing pins (along the z-axis). In addition, the sensitivity and the dynamic range increased when more sensing cells were added. Since the cells were added next to each other along the same row, the resolution of the oil thickness measurement was not affected.

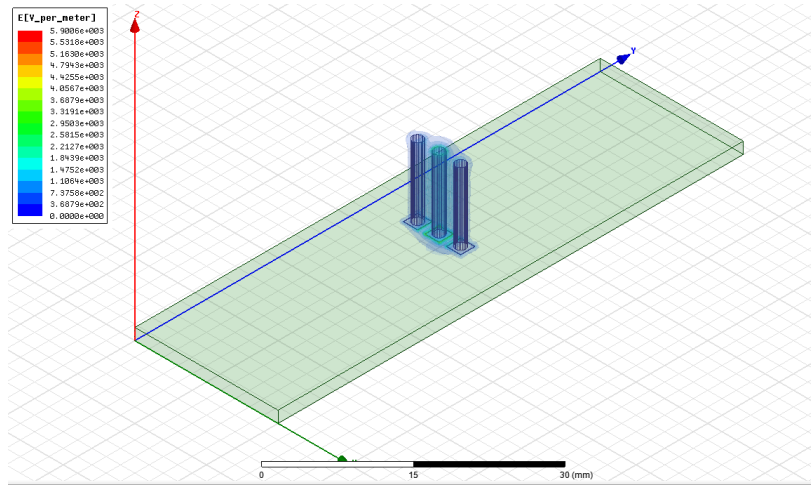


Figure 4.8: Electric field magnitude - Single sensing cell

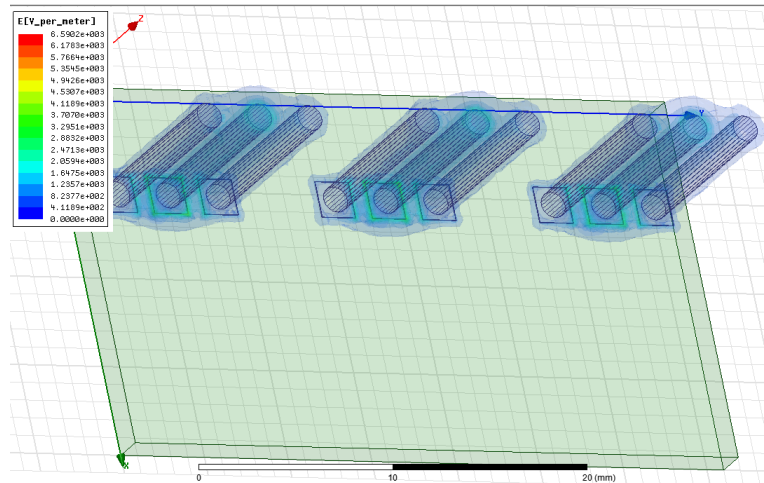


Figure 4.9: Electric field magnitude - Three separated sensing cells

4.2.6 Experimental evaluation

In order to validate the analysis made via simulations, several prototypes were implemented and tested. Figure 4.11 shows the implemented PCB prototypes, including the interleaved, spiral, concentric, parallel, and pins-based designs.

The prototypes were tested according to the following criteria. First, to record the base capacitance, a LCR meter instrument (*BK Precision 875B*) was used to measure the capacitance of the prototypes in air. The measurements were performed indoors with an ambient temperature of around 25 degree Celsius. Then, the maximum capacitance was measured for each prototype, while being totally immersed in oil. The experiments were performed using a gear lubrication oil (SAE 140) having a dielectric constant between 2.1 and 2.8 [41]. A cylindrical

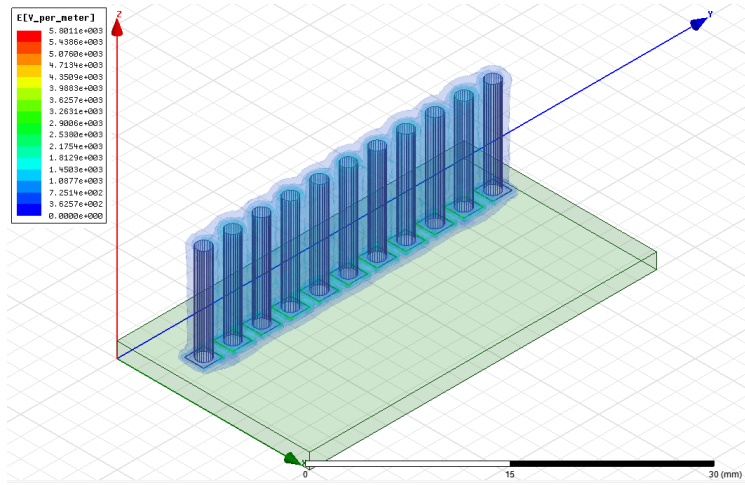


Figure 4.10: Electric field magnitude - Five sensing cells

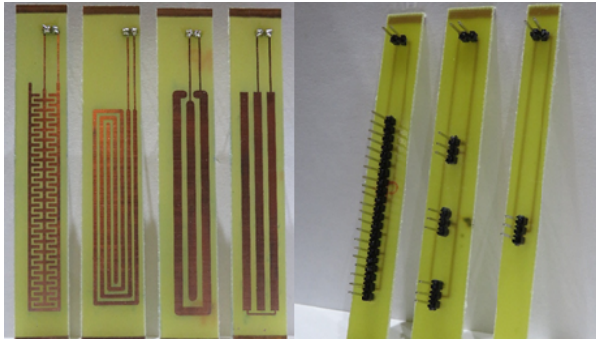


Figure 4.11: Implemented sensor prototypes (optimization study)

liquid container with a diameter of 8 cm and a height of 9 cm was used in the experiments. The capacitance measured in air and oil, as well as the absolute differences (A.D.), are summarized in Table 4.4.

The results of the measurements showed the following:

- For all designs, the maximum capacitances (oil) were smaller than the maximum capacitances recorded in simulations. This is because the dielectric constant of the oil (≈ 2) is smaller than the dielectric constant of the MUT used in the simulations.
- The measured base capacitances of the concentric and parallel designs matched the capacitances recorded in simulations. In addition, the two designs encountered an identical capacitance change (≈ 1 pF) after being immersed in oil. This result shows a good agreement with simulations where the two models have an identical change due to the presence of the MUT.
- The measurements demonstrated that the interleaved design provided the

Implemented Prototypes	Capacitance (pF)			
	<i>Air (pF)</i>	<i>Oil (pF)</i>	<i>A.D.(measured)</i>	<i>A.D.(simulation)</i>
Parallel	4.8	5.8	1	2.79
Concentric	4.6	5.7	1.1	2.91
Interleaved	11.2	13.4	2.2	4.48
Spiral	12.3	14.6	2.3	-
Pins (1 cell)	1.6	2	0.4	1.07
Pins (3 cells)	3.2	4.7	1.5	3.20
Pins (10 cells)	7.2	11.1	3.9	-

Table 4.4: Experimental results of the design optimization study

largest sensitivity in comparison to other co-planar designs. It is important to note that the dynamic range of the interleaved design was twice the dynamic range of the parallel and concentric designs in both simulations and measurements.

- The spiral design (not used in simulations) showed a similar sensitivity to the interleaved design. However, the interleaved design is preferred because of its smaller area.
- For the designs based on pins, the measurements showed that their average base capacitance is smaller than the coplanar designs. For example, the second design (3 cells) has a sensitivity greater than that of the parallel and concentric coplanar, with a smaller base capacitance.
- The measurements showed that the sensitivity of the pins-based sensors increased when more cells were added.
- The third design based on pins, with 10 cells, possessed the maximum sensitivity with an intermediate base capacitance. Therefore, this design represents the most effective solution to differentiate between different dielectric materials, and at the same time to mitigate the oil-fouling problem.

4.2.7 Conclusion

In this section, we presented the results of a simulation-based study performed to assess the impact of different designs of electrodes on the performance of our capacitive sensor. The results showed essential information about the relation between the design variables and the performance of the sensor. Based on these results, we proposed a new electrode design based on thin needle-like pins to improve the sensitivity, dynamic range, and penetration depth of the sensor. In

addition, the proposed pins are best suited for detecting the water level in the multiphase oil-water mixture due to their role in penetrating the oil layer caused by fouling and enhancing the rate of the signal change. Therefore, in the dual-modality sensing system, a decision was made to remove the planar electrodes and replace them by a set of thin needle-like pins acting as the sensing electrodes.

Minimizing the area of the electrodes by using the pins instead of the coplanar electrodes reduces the capability of the sensor to differentiate between insulating materials such as air and oil based on capacitance differences. However, it does not affect the capability of the sensor in detecting the water level due to large water conductivity. The ultrasonic sensor is used to compensate for the need to detect the air-oil interface by providing distance measurements indicating the total liquid level.

4.3 System implementation

In this section, we present the implemented prototypes for the hand-held and the skimmer-mount sensing systems.

4.3.1 Ultrasonic sensor

The ultrasonic range detection sensor selected is named *ToughSonic 3 (TSPC-30S2 Series)* provided by *Senix Corporation*. This sensor has a resolution of 0.086 mm and a maximum range of 91 cm. It has a short dead-zone distance of 4.5 cm and could be connected to a microcontroller using serial communication. To account for the dead-zone sensing area of the ultrasound sensor, the sensing probe was mounted inside an enclosure installed with an offset distance above the capacitive sensor board. In order to allow the microcontroller to read the measurements directly from the ultrasonic sensor, an RS232-TTL conversion circuit based on MAX232 chip was included in the circuits of the processing units.

4.3.2 Hand-held device

The implemented hand-held device, shown in Figure 4.12, is composed of three main components:

- Sensor unit: responsible for obtaining the measurements and sending them to the microcontroller. It contains the capacitive and ultrasonic sensors.
- Processing unit: responsible for data acquisition, processing, display and logging. It is equipped with an OLED screen to show the results and a set of buttons to allow the user to select particular sensor functionalities, such as calibration and measurement.

- Mounting mechanism: composed of an extensible hand grip and mounting mechanisms for the sensor and processing units.

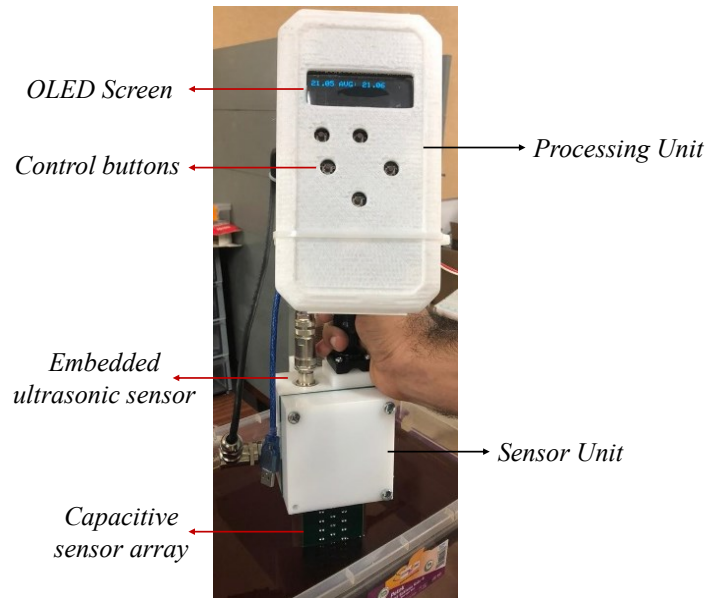


Figure 4.12: Hand-held device

Capacitive sensor

The capacitive sensor board for the hand-held device was implemented using a 6-layer PCB (see Figure 4.13). The connection layers were embedded in the inner layer of the PCB. Two grounded copper sheets were included above and under the connection layers to isolate the tracks from any possible external interference. The implemented PCB contained 48 sensing cells with two pins in each cell. The first pin is connected to the sensing channel of the MPR121 chip and the second pin is grounded. The pins have a diameter of 1 mm and the horizontal gap between them is 2.4 mm. The vertical gap between the sensing cells is 1 mm. This configuration results in a sensing resolution of three millimeters for the capacitive sensor. The PCB was given a T-shape and equipped with 6 mm mounting holes at its edges to facilitate the mounting into the sealed package. Images showing samples of the implemented PCB are shown in Figure 4.14. Note that sockets were used instead of direct soldering to mount the MPR121 devices to the PCB. This would facilitate the replacement of any of the four MPR121 breakout boards in case of failure.

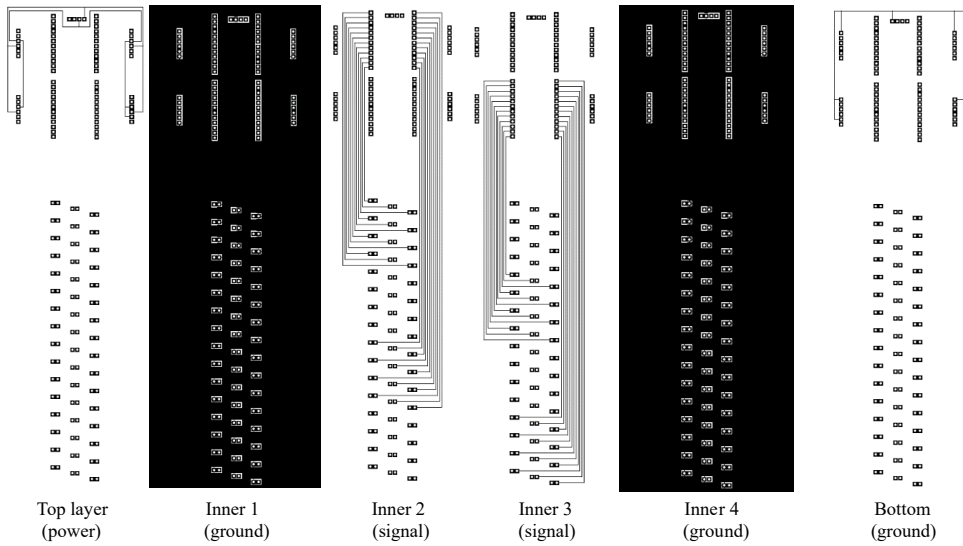


Figure 4.13: PCB layout - Hand-held capacitive sensor

Processing unit

The processing unit was implemented based on the *Teensy* microprocessor-based development board provided by *PJRC*. This module includes a 32-bit microprocessor (MK64FX512VMD12) and is pre-flashed with a boot-loader. Thus, no additional devices are required for re-programming the module other than the USB cable. It has a flash memory of 512 KB, RAM of 256 KB, and 58 digital I/O pins. The board includes a built-in micro SD socket which can be used for data logging and saving/reading settings. In addition to the processor, the processing unit included several other modules including: OLED display, GPS module, control buttons, and temperature sensor.

4.3.3 Skimmer-mount device

The skimmer-mount sensor followed a similar configuration of the hand-held sensor with some modifications. Basically, the major difference between the two devices is in the resolution of the two sensors. The skimmer-mount sensor has a resolution of 10 mm and a sensing range of 50 cm. Also, the skimmer-mount device does not include a screen to display the results. Instead, it is equipped with wireless communication module to send the results to a base station within a range of 200 meters.

Capacitive sensor

Two prototypes of the skimmer-mount capacitive sensor were implemented. In the first prototype, the pins were mounted using the traditional soldering tech-



Figure 4.14: Implemented capacitive sensors - hand-held

nique. In the second board, the pins were assembled using the press-fit technology. The two prototypes have the same connections and dimensions. The vertical gap between the sensing units is 10 mm, and the distance between the top and bottom units, representing the sensing range, is more than 50 cm. The PCB is made from six layers and has a total thickness of 2 mm. The connection tracks are mounted in the inner layers and the sensing units are mounted on the surface layers. Each sensing unit contains five pins in which two of them are connected to the capacitive transducer and the others are connected to the system ground. Passive shields (ground-connected) planes are embedded in the inner layers to protect the sensor from external fields. The shielding also protects the tracks from the effect of water splashing or touching by human-hand or other conductive objects. Photos of the implemented prototypes are shown in Figure 4.15.

Processing unit

The electronic components of the processing unit for the skimmer-mount sensor are similar to the ones used in the hand-held device (described in the previous section). For example, temperature sensor, GPS module, RS232-TTL converter, and a Teensy 3.5. Note that the OLED screen was removed and the XBEE module was added to allow for wireless communication. The XBEE module was connected to the processor using hardware serial communication port. The circuit was designed using the Proteus software and implemented using a double-sided PCB. The 3D model of the PCB and the implemented prototype are shown in Figure 4.16.

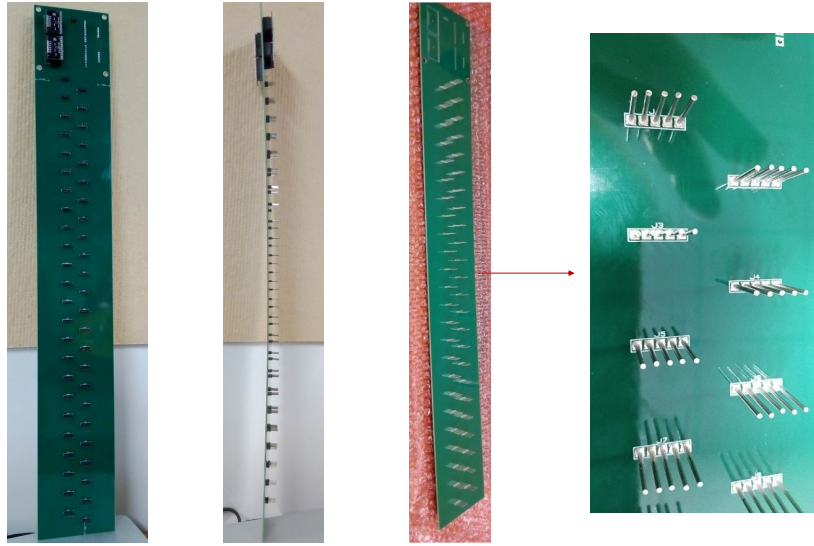


Figure 4.15: Implemented skimmer-mount capacitive sensor

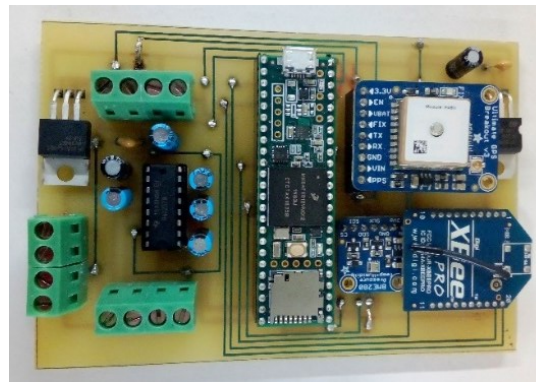


Figure 4.16: Processing unit PCB for the skimmer-mount device

4.4 Classification approach

To classify the capacitive sensor units, a classification method was developed based on four major stages: data acquisition, normalization, feature extraction, and classification. The overall block diagram of the proposed method is shown in Figure 4.17 and each of the included steps is explained below.

4.4.1 Data acquisition

The analog voltage of each sensing cell is measured sequentially by the MPR121 transducers. These voltages are converted to digital values and stored in the dedicated registers as discussed before. In a single measurement cycle, the microcontroller reads the digital voltages of all of the sensing cells and stores them

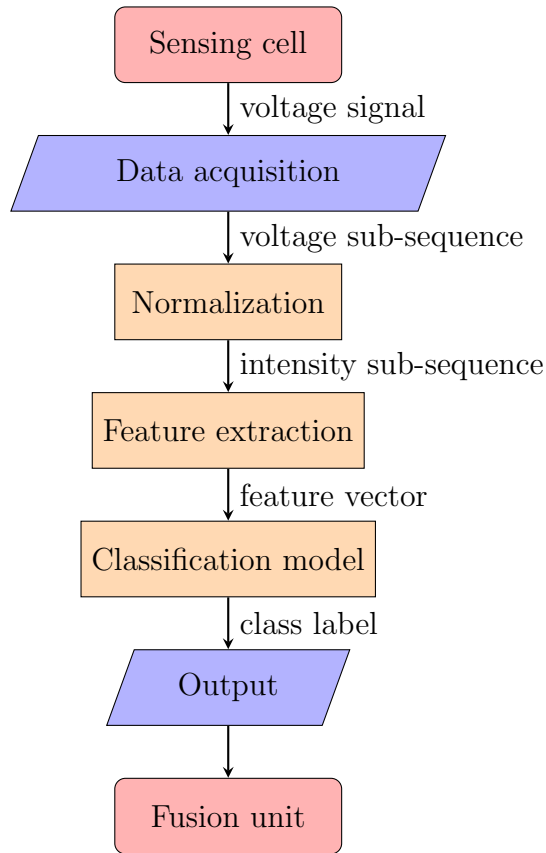


Figure 4.17: Flow chart of the signal classification method

in a single row of a temporary matrix. The temporary matrix has a fixed size where the number of columns represent the count of the sensing cells and the number of rows represent the number of consecutive measurement cycles performed. In order to fill the temporary matrix, a fixed number of measurement cycles are performed at a fixed sampling rate set to 100 ms. Since the number of measurement cycles was set to 10, the microcontroller needs one second to fill the temporary matrix. After exiting the data acquisition loop, the values stored in the temporary matrix are sent to the normalization routine.

4.4.2 Normalization

The normalization of the measured voltages is performed based on 3.9. Note that the normalization process converts the absolute voltages to intensity values representing the ratio of the high permittivity material (water).

4.4.3 Feature extraction

Feature extraction is the process of transforming the raw time-series data (also named as discrete/digital signals) into a reduced set of features. A finite set of statistical measures could be used as a feature-based representation of the signal. These features are application dependent and should be selected based on their contribution to the classification result. Usually, several statistical features could be used such as the arithmetic mean, standard deviation, skewness, kurtosis, chaos, energy, and periodicity. However, since we divided the sensor signals into short sub-sequences (10 values each) that are recorded in a short period of time (one second), our signals could be assumed linear and we need to select some features that best describe their main properties; amplitude and shape. After testing several statistical features, we found that the optimal features could be reduced to two: average and steepness. The average feature, calculated in 4.8, is used to describe the amplitude of the signal, and the steepness feature, calculated in 4.9, is used to describe its orientation; increasing, decreasing, or stable.

$$mean = \frac{\sum_{i=1}^N I_i}{N} \quad (4.8)$$

$$steepness = I_N - I_1 \quad (4.9)$$

where N is the number of intensity values included in the each signal.

4.4.4 Classification model

Supervised learning methods aim to infer a function that relates the output class label to the input feature vector. This relation is extracted by observing the training set. In the literature, there is a wide variety of supervised classification algorithms. However, for binary classification problems, where the output label is either 1 or -1 (true or false), Support Vector Machines (SVM) are widely used. Support Vector Machines (SVM) define a hyperplane, which best separates a given set of training samples. In the training phase, the hyperplane is defined by maximizing its distance to the closest instances from each class (support vectors). After learning the coefficients, the model is used to classify new samples. The implementation of the SVM model in the microcontroller's code is simple and involves the execution of the function $f(w_1 F_1 + w_2 F_2 - b)$, where w_1 and w_2 are the model coefficients, and b is the bias value. If the function returns a positive value, the cell is classified as water-immersed, otherwise, the cell is classified as oil-immersed.

The classifier unit takes the feature vector representing the intensity signal of a single sensing cell and identifies the type of material in which the cell is immersed in; water or oil/air. This task is formulated as a binary classification problem where a label of +1 represents the conductive material (water) class and

a label of -1 represents the insulating material (oil/air) class. The classification process is applied to the intensity signals obtained from all of the sensing cells sequentially. After the classification is completed, a vector containing the predicted labels is created. The output vector is sent to the *Fusion Unit* to infer the oil thickness given the other parameters obtained from the distances measured by the ultrasonic sensor.

It is important to note that the machine-learning-based technique could be applied as a method for classifying sensor signals created by the previously introduced self-capacitance sensing system. However, we should note that the classification model should be trained against different types of oil to be able to differentiate between air and oil layers. In this case, the classification is more challenging since unpredicted mixtures of oil could be formed under real oil-spill conditions. By using the dual-modality sensing scheme, the model is trained to differentiate between insulating (air/oil) and conductive material (water). This training enhances the generalization of the model to unseen oils since it relies on the common insulating property of all types of oil.

4.5 Dataset and model development

The dataset is composed of digital signals obtained from the capacitive sensor cells that are immersed in water or in air/oil. Each signal, stored in one row, is composed of 10 consecutive intensity values and a label in the last column. The label is +1 for a water-immersed sensor electrode and -1 for an air/oil-immersed sensor electrode. The dataset is used to train a classifier to infer the type of material in which an electrode is immersed in (water or air/oil), given a sample signal composed of 10 consecutive values.

4.5.1 Dataset creation procedure

To create the dataset, we designed an experimental procedure that measures, normalizes, and labels the sensor signals autonomously. In particular, the micro-controller was programmed to calculate a set of 10 consecutive intensities for each sensing cell, and send them as a comma-delimited text messages to the computer via the serial port. The messages were reported at a rate of one message per second and the intensity values were calculated based on the reference voltages recorded during calibration. Two different modes of operation were used to create the dataset while the sensor is under static and dynamic conditions as described below.

Static mode

The first experimental condition used to create the dataset is the "static mode". In this mode, the sensor was activated after being immersed in the multiphase

mixture for a long duration of time; more than 10 minutes. Visual observation was used to decide on the actual states (labels) of the investigated sensing cells. The workflow of the automated process used to create the dataset under this mode is illustrated in Figure 4.18.

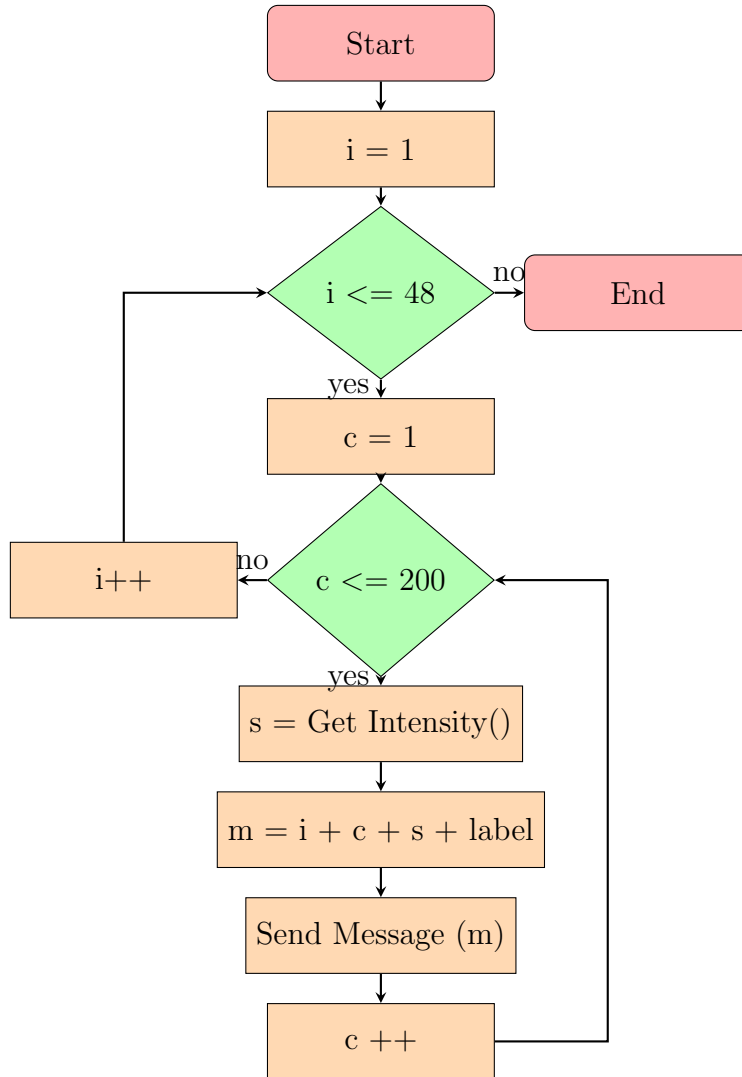


Figure 4.18: Flow chart for dataset creation in static mode

Dynamic mode

The dataset created under the "dynamic mode" is composed of different sets of signals obtained from different sensing cells while they were immersed in the oil and water phases at different instants of time. Similar to the dataset created in the static mode, the resulting dataset obtained in the dynamic mode is composed of fixed-size intensity signals labeled as +1 (water) or -1 (oil). However, the major

difference here is that the capacitive sensing cells were constantly moving between the water and oil phases. The recording of the signals was initiated immediately after the target cell moves from one phase to another; from water to oil or from oil to water. To move the target cell from one phase to another, we programmed the linear actuator holding the capacitive sensor array to follow a square-wave vertical motion. The distance measured by the ultrasonic sensor was used as a reference to obtain information about the phase in which the target cell is immersed in at a certain instant of time. The major steps of this process are listed below:

- the linear actuator was programmed to move the sensor vertically (up and down) at a constant speed (ex: 20 mm/second).
- the actuator stops when reaching the upper and bottom positions for a fixed duration of time (*e.g.* 60 seconds).
- while the sensor is held at the upper position, the target electrode is immersed in oil; consecutive intensity signals are labeled -1.
- while the sensor is held at the bottom position, the target electrode is immersed in water; consecutive intensity signals are labeled +1.

Note that the rate in which a complete measurement cycle is completed (measurements rate) is one measurement per 100 millisecond. Thus, since each intensity signal contains 10 values, it takes around one second to record a single intensity signal.

4.5.2 Applied procedure and created dataset

In this section, we describe the experimental steps performed for creating the dataset. Also, we describe the structure and dimensions of the created dataset.

Base voltage calibration

The process starts by recording the base voltages of the capacitive cells. As noted before, these values are required to calculate the intensity values. Thus, the first step is to record the base voltages of the sensing cells while the sensor is immersed in the air. For instance, the base voltages of the skimmer-mount capacitive sensor "1" are shown in Table 4.5. The voltages are listed in the digital form after ADC conversion as calculated based on 3.7.

After recording the base voltages, the system was mounted on the linear actuator mechanism of the laboratory experimental setup and immersed in a multiphase oil-water mixture as shown in Figure 4.19. It was noted that the sensing cells were distributed in the different components of the multiphase mixture as follows:

Cell Index	Voltage (ADC)	Cell Index	Voltage (ADC)
C1	644	C25	284
C2	561	C26	283
C3	563	C27	269
C4	507	C28	271
C5	521	C29	271
C6	466	C30	274
C7	472	C31	258
C8	427	C32	261
C9	427	C33	245
C10	387	C34	246
C11	389	C35	231
C12	355	C36	235
C13	491	C37	243
C14	443	C38	242
C15	450	C39	232
C16	413	C40	232
C17	421	C41	235
C18	386	C42	238
C19	392	C43	227
C20	362	C44	228
C21	363	C45	216
C22	333	C46	216
C23	332	C47	207
C24	312	C48	210

Table 4.5: Base voltages for skimmer-mount capacitive sensor 1

- Air Phase: Cells from index 1 to index 35
- Oil Phase: Cells from index 36 to index 39
- Water Phase: Cells from index 40 to index 48

After mounting the system on the experimental setup, ultrasonic offset calibration was performed.

Ultrasonic offset calibration

To acquire the offset ultrasonic distance, the distance to the liquid level was measured by the ultrasonic sensor. The average of the measured distances is 513.45 mm with a standard deviation of 0.086 mm indicating the high precision of the sensor. The offset distance was calculated using 4.1 as described before;

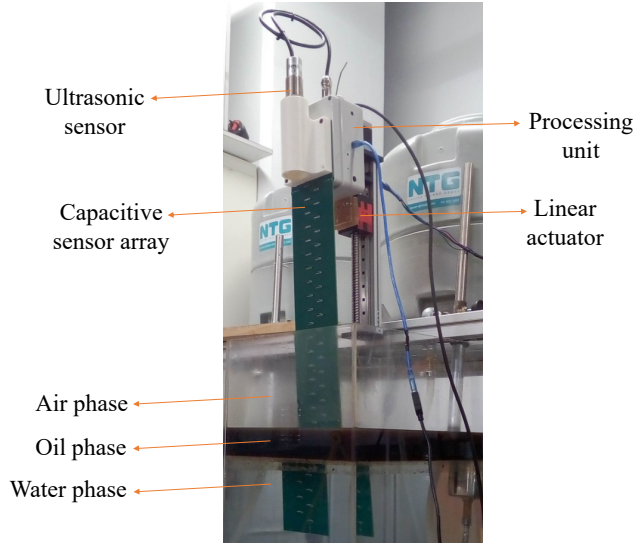


Figure 4.19: Experimental setup for the skimmer-mount device

knowing that $I_L = 36$, $W = 2$ mm, and $G = 10$ mm, the resulting offset distance is 93.5 mm. In real-time, the partition of the capacitive sensor array which is immersed in air (air section) is calculated by subtracting the offset distance from the ultrasonic measured distance. These parameters are essential for creating the dataset as described below.

Dataset structure and contents

The dataset was created under static and dynamic modes based on the experimental procedure described previously. A sample of the dataset obtained under static mode is shown in Table 4.6. The first column contains the cell index, the second column contains the message number, and the intensity signal values start in the third column. The last column shows the class label of the signal; -1 for oil/air and +1 for water. Note that under steady-state conditions, signals originating from water or oil cells are stable but different in terms of magnitude; water cells have a large intensity value of around 50 percent and oil cells have a small intensity value of around 1 percent.

Cell Index	Message Number	I1	I2	I3	I4	I5	I6	I7	I8	I9	I10	Label
38	199	1.72	1.72	1.72	1.72	1.72	1.72	1.72	1.72	1.72	1.72	-1
38	200	1.72	1.72	1.72	1.72	1.72	1.72	1.72	1.72	1.72	1.72	-1
39	1	55.17	55.17	55.17	55.17	55.17	55.17	55.17	55.17	55.17	55.17	+1
39	2	55.17	55.17	55.17	55.17	55.17	55.17	55.17	55.17	55.17	55.17	+1

Table 4.6: Sample of the dataset (static mode) - skimmer-mount sensor

In the second phase of the dataset creation process, the signals were recorded under dynamic mode; the target sensing cell changes its position from being

immersed in one material to another. Thus, one target electrode is tracked while it moves from the oil phase to the water phase, stays in the water phase for a certain amount of time, and then moves back to the oil phase. Intensity signals were recorded while the electrode is immersed in one of the two phases. To accomplish this process automatically, we programmed the vertically-installed linear actuator to follow a square-wave motion as described before.

Figure 4.20 shows a set of photos taken consecutively after the sensor moves downwards and stops at the bottom position; the top three sensing cells were initially immersed in the oil phase and moved to the water phase. These sensing cells are labeled 27, 28, and 29 from top to bottom. The first photo taken after 5 seconds shows how the cells are fouled by oil. As time passes, the oil is removed from the cells and the pins appear more clearly. This process, referred to as “cleaning”, could be confirmed by observing the state of the fouled electrodes in the consecutive images taken after 10, 25, and 50 seconds.

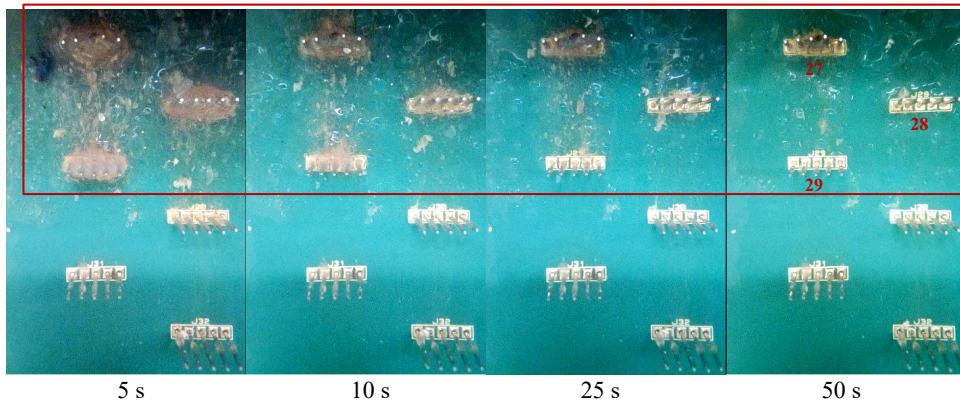


Figure 4.20: Oil fouling of the sensing pins - skimmer-mount sensor

The signals obtained under dynamic and static modes were concatenated in a one dataset file. The total number of samples is 4474 distributed into 2569 of water samples and 1905 of oil samples. The samples were converted to a set of feature-based vectors containing the mean and steepness of each signal. A scatter plot showing the distribution of the vectors in the feature space is shown in Figure 4.21.

It is important to note that the steepness value is positive for the water samples and negative for the oil samples. In addition, the average value is high (around 80 percent) for the water samples and low (less than 20 percent) for the oil samples. The number of water samples having an average value of more than 20 percent is 2443. The minimum steepness value for all water samples having an

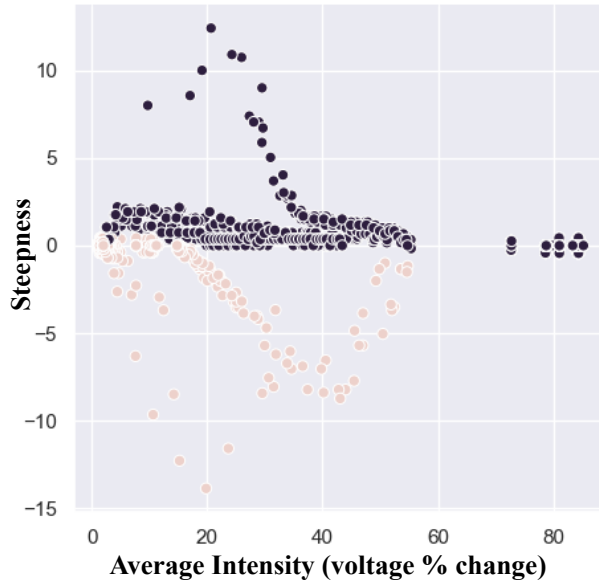


Figure 4.21: Scatter plot of the dataset (black: water, brown: oil)

average of greater than 20 percent is -0.444 . This indicates that water samples are expected to have a large average value (greater than 20) and at the same time must have a steepness value that is greater than -1 . In fact, steepness values which are less than -1 indicate that the intensity of the electrodes is severely decreasing and this could not be the case when the sensing cell is immersed in water.

4.5.3 Model development

To differentiate between the water and oil samples, a linear SVM model was trained using the python sickit-learn library [42] and implemented as an equation in the code of the microcontroller. The coefficients of the trained linear model are listed in Table 4.7.

Device	Weight 1	Weight 2	Bias
Skimmer-mount sensor device	0.169	3.958	-3.561
Hand-held sensor device	0.163	3.283	-4.286

Table 4.7: Coefficients of the trained classification models

4.6 Experimental evaluation and analysis

In this section, we describe the laboratory experimental evaluation of the implemented dual-modality sensing systems. It is important to mention that operational testing was supposed to be performed at the OHMSETT facility during Summer 2019-2020. However, due to COVID 19 pandemic, the operational testing was postponed to Spring 2020-2021.

4.6.1 Ultrasonic sensor

In order to evaluate the performance of the ultrasonic sensor while measuring the distance to the top surface of the oil, the sensor was fixed at a distance of 98 cm above the oil surface and activated for a duration of around 1 hour. The sensor measured consecutive distances at a sampling rate of one measure per 50 millisecond; the total number of recorded measurements is 81800. The results showed that the measurements ranged between 9.78 and 9.82 cm with an average of 9.80 cm and a standard deviation of 0.0066 cm. The result demonstrates the ability of the selected ultrasonic sensor to measure the distance to the top surface of the oil with high accuracy and repeatability.

Another set of experiments were performed to evaluate the performance of the ultrasonic sensor while working under dynamic liquid conditions. As explained before, the distance measured by the ultrasonic sensor is used to extract the air-immersed partition of the capacitive sensor array. Based the proposed oil-thickness estimation algorithm, oil thickness is estimated after recording several measures in a short temporal window. Thus, a single value representing the distance between the ultrasonic probe and the liquid level should be selected. We should note that this process should take into account the effect of slosh waves on the measured distances. For instance, if the liquid surface is subjected to slosh waves, high frequency noise will be introduced to the measured distances. To assess the signal of the ultrasonic sensor under these conditions, we designed an experimental setup where the sensor is mounted above a water-filled container (pointing downwards) and slosh waves were introduced to the water manually using a rectangular plate. Messages containing 10 consecutive distances measured by the ultrasonic sensor were sent to the computer at a rate of one message per second. After recording the messages, three functions were applied to extract a value representing each message: Maximum, Mean, and Median. The results of the three functions are shown in Figure 4.22.

The experimental results revealed that random slosh waves caused large increases in the signal resulting from the *Maximum* function. Note that in relative to the average measured distance, which is around 280 mm, the distance increased to 310 mm showing a large deviation of around 30 mm. The signal resulting from the *Mean* function showed a relatively stable behavior but was also affected by the waves; note that the mean of a set of measurements is easily biased by a

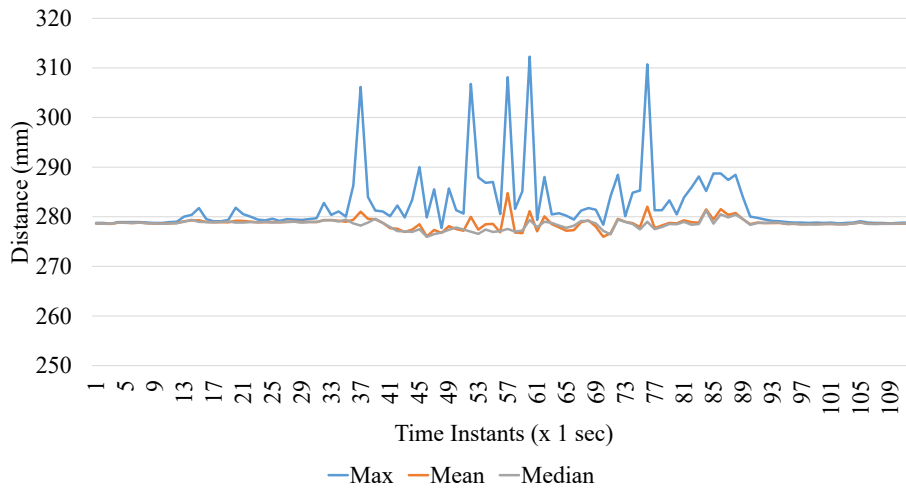


Figure 4.22: Ultrasonic distances resulting from max, mean, and median filters

single large outlier. Since the signal resulting from the Median calculation was not affected by the slosh waves, a decision was made to use a moving median filter to remove large deviations in the ultrasonic sensor output. Note that the filter is applied by selecting the median value from the set of distances recorded during each of the temporal windows.

4.6.2 Measurement of oil thickness

The experimental evaluation of the implemented systems was performed under laboratory conditions; using the indoors laboratory setups with a room temperature of around 23 degree Celsius. Transparent containers were used; glass container for the hand-held and plexiglass container for the skimmer-mount. After filling the containers with tap water, different amounts of oils were poured above the water surface. The actual thickness of the oil samples was measured using a ruler attached to the external wall of the setup.

Manual testing (hand-held)

The hand-held device was tested against fuel oil with high viscosity (3777 cSt) and gear oil of intermediate viscosity (140 cSt). The experimental setup used in the testing is shown in Figure 4.23. In our testing, we performed several iterations of measurement after dipping the sensor in the liquid and requesting thickness measures. The device was held by hand and the measurements were displayed on the screen. The average and standard deviation of the experimental results are listed in Table 4.8.

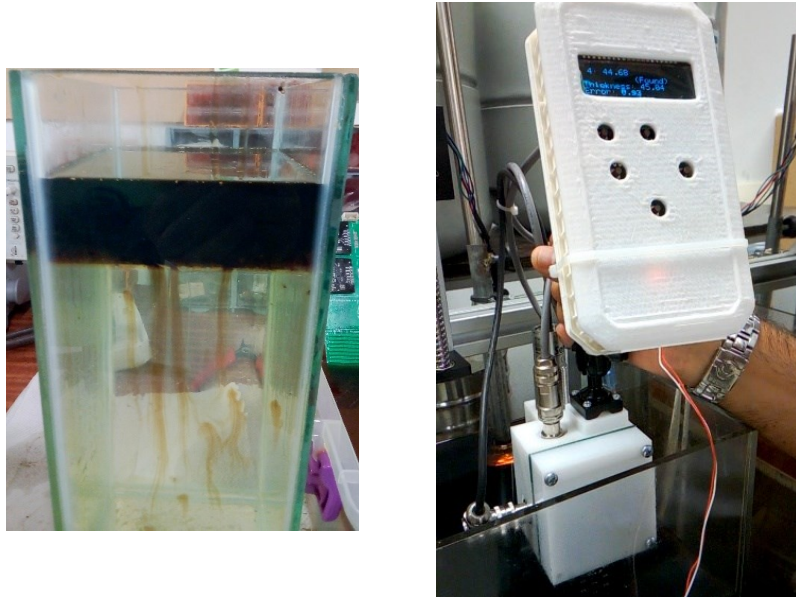


Figure 4.23: Left: Hand-held testing: container (left), hand-held device (right)

Oil type	Actual thickness (mm)	Measured Thickness (mm)	Standard Deviation
Gear oil	45	44.732	1.18
Fuel oil	37	35.093	1.86

Table 4.8: Hand-held sensor testing (manual) - experimental results

As shown in the results, the laboratory testing of the hand-held device against the two different types of oil showed high accuracy of measurement with an absolute error of less than 2 mm. We should note that the capacitive sensor resolution is related to the vertical gap between the sensing cells which is 3 mm. Thus, we can conclude that the high resolution of the ultrasonic sensor contributed to enhancing the accuracy of the system in comparison to the previous self-capacitance sensing system.

Experimental setup testing (hand-held)

Several experiments were performed while the hand-held sensor was mounted on the experimental setup. In these experiments, the sensor was tested against samples from light engine oil and gear oil. A summary of the experimental results is shown in Table 4.9.

As shown in the results, the oil thickness measurements were stable with a standard deviation less than 0.5 mm. Also, the measurements were accurate since the absolute error did not exceed 0.5 mm. Note that based on the application requirements, the resolution of the hand-held sensor device is about 3 mm.

Oil type	Actual thickness (mm)	Measured Thickness (mm)	Standard Deviation
Light oil	13	13.53	0.071
Gear oil	33	33.37	0.37

Table 4.9: Hand-held sensor testing (fixed) - experimental results

Skimmer-mount device

Several tests were performed to evaluate the skimmer-mount device under laboratory conditions. The liquid container was filled with tap water and specific amounts of oil were added to the water surface. We recorded a set of measurements under static and wavy liquid conditions while the sensor is mounted to the experimental setup. In addition, the sensor was tested manually in a dynamic mode; the device was held by hand and immersed continuously in an oil-water mixture composed of tap water and light engine oil. The experimental results are shown in Table 4.10.

Oil type	Actual thickness (mm)	Measured Thickness (mm)	Standard Deviation
Light oil (setup)	25	22.025	0.0665
Light oil (setup with waves)	25	26.12	0.83
Light oil (manual with waves)	29	31.85	7

Table 4.10: Skimmer-mount device - experimental results

For the tests performed using the experimental setup, the sensor showed high accuracy with an average absolute error of less than 3 mm. We should note that the standard deviation of the measurements increased to around 1 mm when waves were introduced to the water surface. For the manual tests, the standard deviation increased to around 7 mm. Note that this increase is related to the movements induced by the user holding the sensor by hand. Despite this variation, the results of the manual tests also showed high accuracy with an average absolute error of less than 3 mm. Note that all of the measurements were still less than the sensor resolution which is 10 mm.

Skimmer-mount device - Dynamic

To evaluate the performance of the skimmer-mount device while working under dynamic conditions, the sensor was mounted on the linear actuator installed on the laboratory setup and programmed to move vertically in and out of the multiphase oil-water mixture. Gear oil with high viscosity of 140 W and a thickness of 50 mm was used in the experiment. The span of motion of the linear actuator was set to 50 mm and the speed was set to 20 mm per second. The experiment lasted around 30 minutes and the measurements were reported by the device via serial port at a rate of one measurement per second. A statistical summary of the obtained results is shown in Table 4.11.

Oil type	Gear oil
Actual thickness (mm)	50
Average measured thickness (mm)	52.02
Standard Deviation (mm)	2.71
Average absolute error (mm)	2.02
Average percentage error (%)	4.04
Count of measurements	1451

Table 4.11: Skimmer-mount device - dynamic testing results

As shown in the results, the skimmer-mount device showed high accuracy and high precision under dynamic testing conditions with an average absolute error of 2 mm and a standard deviation of 2.7 mm.

4.7 Conclusion

In this chapter, we described a dual-modality sensing system based on a combination of capacitive and ultrasonic sensors to measure the oil thickness. Two different devices were developed to fit different use-cases; hand-held and skimmer-mount. Testing showed that the results were enhanced in comparison to the previously implemented systems. For further improvement, online filtering methods should be studied and applied to smooth the measurement result and minimize the error under harsh dynamic conditions. Further testing will be performed at the OHMSETT facility to evaluate the performance of the implemented systems under realistic operational conditions.

Chapter 5

Other applications

This chapter describes two different applications related to our proposed sensing methodology. In the first section, we describe a new sensing method for measuring the viscosity of oils in online measurement applications. This method was inspired from working on the oil-fouling problem in measuring the oil thickness. In particular, the time required to remove the oil from the surface of the sensor when it moves from one phase to another was found to be directly related to the viscosity of the oil. Based on this observation, we proposed to monitor and analyze the rate of change of the sensor capacitance to infer the oil viscosity. In the second section, we describe the use of capacitive sensor arrays to measure the moisture of soils at different depths and to calculate the water infiltration rate. This method is considered as another direct application of our proposed self-capacitance sensor array to characterize a multiphase mixtures composed of air, soil, and water.

5.1 Measurement of oil viscosity

Measurement of oil's internal flow resistance, usually known as viscosity, is essential in several domains such as automotive and oil production. Although different types of viscosity measurement instruments are available, several limitations affect their usability in online measurement applications; mainly the requirement for calibration and cleaning. In this section, we describe a new method for detecting the viscosity of oils in online measurement applications. The proposed method relies on analyzing the changes in the sensor's capacitance while it is moving vertically from the oil phase to the air phase. The advantages of the proposed sensing method includes the low cost of implementation, simplicity of operation, and online calibration capability.

5.1.1 Related work

Real-time viscosity sensing provides essential information for applications in a wide variety of domains. For instance, viscosity is considered a critical attribute that impacts product quality in the personal care industry [43]. In oil production applications, viscosity is an important parameter for estimating the economic value of a hydrocarbon reservoir and for analyzing its compositional gradients [44]. In the automotive domain, information about the viscosity of the oil is used for evaluating the condition of the engine [45]. Sensors used to measure the viscosity are known as *viscometers* and could be classified based on their sensing principle. For instance, rotational viscometers rely on torque measurements and use rotating spindles immersed in the measured sample. These devices are designed for offline measurement applications where a sample of the liquid could be extracted and measured under controlled laboratory conditions. Another widely known type of viscometers is known as flow cups which measure the kinematic viscosity of fluids based on the effect of gravity. Flow cups could be used for getting approximate and fast measurement of viscosity but they are not designed for industrial applications due to their limited accuracy. In the literature, several sensing methods were proposed for online measurement of viscosity. Mainly, these methods could be categorized into three major categories: 1) body displacement, 2) acoustic, and 3) vibrational [46].

The body displacement method is based on measuring the displacement of a piston immersed in the measured fluid [47]. The basic implementation of this method is based on moving a piston to an elevated position via a pneumatic mechanism and then allowing it to fall into the oil sample under the effect of gravity. The viscosity of the measured oil sample could be derived by measuring the piston travel time. This basic implementation was improved by including two electromagnetic coils around the piston to create a force that would drive the piston up and down [48]. In another implementation, a remotely controlled piston combined with a measuring bushing was used [49]. When the piston is in the lifting position, fluid is drawn into the bushing. The lifting mechanism is maintained by a controller for a specific time after which the piston falls due to gravity.

Acoustic viscometers rely on piezoelectric materials to generate acoustic waves under the application of an alternating electric field. The viscosity of a lubricant is evaluated by measuring the shift in the resonant frequency of the piezoelectric crystal. With the advancement of microfabrication, Capacitive Micro-machined Ultrasonic Transducers (CMUTs) have been used for detecting viscosity [50]. The design principle consists of a CMUT transmitter and receiver. An excitation ultrasonic wave is emitted by the transmitter into the fluid medium. The receiver picks up the transmitted signal and processes it using frequency-domain analysis techniques. The viscosity of the measured material could be inferred from the frequency response of the received signal. In addition to acoustic transducers, the

physical properties of lubricating oils, including viscosity, were evaluated using a combination of ultrasonic, capacitance, and inductance-based sensing methods [51].

More recently, optical-based methods were introduced to measure the viscosity of oils [52]. The optical method is based on emitting a light beam using an LED through an optical fiber that is immersed in the measured oil sample. The light passing through the optical fiber is sensed using a photodetector. As the viscosity of the oil increases, the refractive index of the optical fiber also increases causing the attenuation of the light received at the photodetector. Thus, the attenuation in the received light intensity could be used to infer the viscosity of the measured oil.

Several practical limitations affect the applicability of the methods mentioned above in online viscosity measurement applications. For instance, displacement viscometers are characterized by their design complexity, size, and maintenance requirements. Traditional acoustic and capacitance measurements require accurate calibration and are affected by ambient conditions. Optical fibers require complex setup and are limited to work against specific types of oil.

5.1.2 Proposed sensing method

The proposed sensing method is based on the fact that the flow rate of the oil depends on its kinematic viscosity. Based on this, we propose to monitor the flow rate of the oil by utilizing capacitance measurements. This principle is applied by immersing a coplanar capacitive sensor into the oil sample in a controlled manner and measuring its capacitance continuously. While moving upwards, the sensor is changing from being fully-immersed in oil to being exposed to air. During this phase of motion, the relative permittivity ϵ_r of the dielectric, and consequently the capacitance of the sensor decreases as the air replaces the oil in the sensing region. While the sensor is moving towards the air phase, oil slides from the sensor's surface differently based on its viscosity. Therefore, the rate of change of capacitance calculated while the sensor is moving from the oil phase to the air phase could be used to detect the viscosity of the measured oil sample.

To avoid requiring offline calibration, the system records the capacitance of the sensor when it is fully immersed in the measured oil sample. This capacitance is named the reference capacitance and is obtained in real-time; the system detects the time instant where the sensor reaches the bottom position of the controlled motion and stores the average of a set of capacitance measurements. During operation, the absolute capacitance of the sensor is converted to a value representing the relative change from the reference capacitance; known as the Capacitance Relative Change (CRC) and calculated as shown in 5.1.

$$CRC = \frac{|C_m - C_{max}|}{C_{max}} \times 100 \quad (5.1)$$

Where C_m is the absolute capacitance of the sensor measured in real-time and C_{max} is the reference capacitance recorded while the sensor is fully immersed in the measured oil sample.

5.1.3 Implementation and experimental evaluation

To evaluate the feasibility of the proposed sensing approach, we used a coplanar capacitive sensor implemented using a Printed Circuit Board (PCB). The sensing electrodes were designed based on an interleaved shape as shown Figure 5.1.

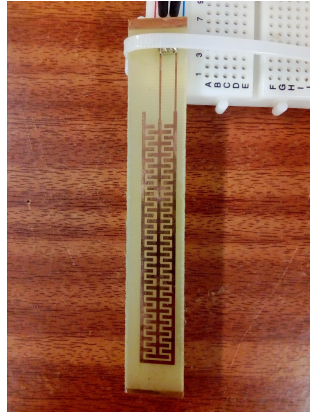


Figure 5.1: Capacitive sensor board used for viscosity measurement

The capacitance of the sensor was measured using the *FDC1004* Capacitance-to-Digital-Converter (CDC) chip provided by Texas Instruments [53]. The CDC chip was connected to a microcontroller-based development board (Arduino Nano) through an I2C channel. To report the measured capacitance in real-time, the microcontroller was connected to a laptop through a serial port. In order to move the sensor in and out of the oil sample in a controlled manner, a vertically-installed linear actuator was used. The experimental setup including the linear actuator, the capacitive sensor, and the oil container is shown in Figure 5.2.

The main aim of the experiment is to record the capacitance of the sensor continuously while it is moving upwards; from the oil phase to the air phase. After recording the capacitance values, the rate of change (slope) of the capacitance is calculated and compared for light and heavy oil samples. For this purpose, the linear actuator was programmed to follow a vertical motion with the following parameters: speed 10 mm/s, stop duration 60 s, and distance of motion 90 mm. Two different oil samples with different viscosity values were tested in the experiment (light oil: 10 W and heavy oil: 140 W). A sample of the experimental results is shown in Figure 5.3.

The experimental results showed that the absolute capacitance of the sensor decreases as it moves from the oil phase to the air phase. This behavior was expected since the relative permittivity of the dielectric decreases during the



Figure 5.2: Experimental setup for viscosity measurement system

upward motion. In addition, the rate of change of the capacitance over time is different for light and heavy oil samples. This conclusion could be made from the apparent difference between the slope of the measured capacitance corresponding to heavy and light oil samples. However, since the reference capacitance for the two oils is different, the results should be normalized before comparison. For this purpose, the absolute capacitance measurements were converted to CRC values according to 5.1. After calculating the CRC values, a moving average with a three-samples sliding window was used to decrease the effect of random noise. The filtered CRC values corresponding to the capacitance recorded while testing light and heavy oil samples are plotted in Figure 5.4.

In our argument, we proposed that the slope of the capacitance change will be different depending on the viscosity of the oil. The results of these experiments showed a clear difference between the slopes of the normalized changes from the reference capacitance for light (10 W) and heavy (140 W) oils. As expected, the heavy oil had a smaller slope since oil slides slower from the sensor surface than the light oil. The light oil is removed from the surface of the electrodes faster than the heavy oil as the sensor moves from the oil phase to the air phase. This result indicates that information about the rate of change of capacitance could be used to detect the viscosity of the measured oil sample.

5.1.4 Conclusion

In this section, we described a new sensing method for detecting the oil viscosity in online measurement applications. The proposed method is based on a coplanar capacitive sensor combined with a vertically-installed linear actuator. The actuator dips the sensor into the oil sample while the capacitance of the sensor

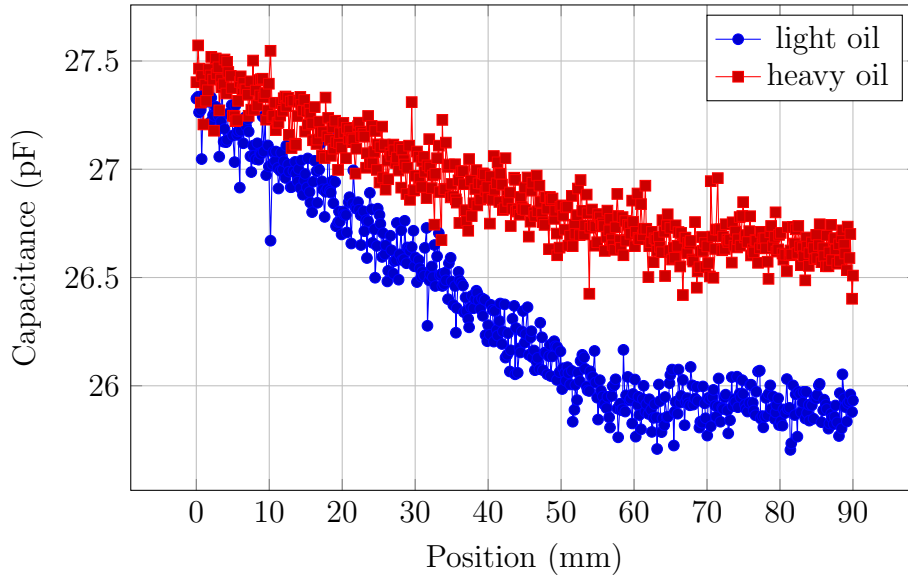


Figure 5.3: Plot of absolute capacitance (pF) vs. position (mm)

is measured continuously. Since the flow rate of the oil is directly related to its kinematic viscosity, we proposed that the slope of the capacitance change is directly related to the oil viscosity. Initial experiments demonstrated the validity of this hypothesis and is considered a proof-of-concept for this new sensing method. Further work could be done on optimizing the sensor design and performing additional experiments on several types of oil to formulate equations relating the oil viscosity to the slope of the measured capacitance signals.

5.2 Measurement of soil moisture

Measurement of soil moisture is essential for precision agriculture and smart irrigation applications. However, currently available measurement techniques have several limitations that affect their performance under field conditions. This section presents a low-cost and simple-to-use instrument for measuring the soil moisture based on a coplanar capacitive sensor array. The main advantage of the proposed instrument is that it allows for high-resolution water depth profiling by sensing the changes in the soil moisture at different soil depths, ranging from 2 mm to around 150 mm with increments of 2 mm. This allows the sensor to produce an output representing the depth of the interface layer separating dry and wet soil layers.

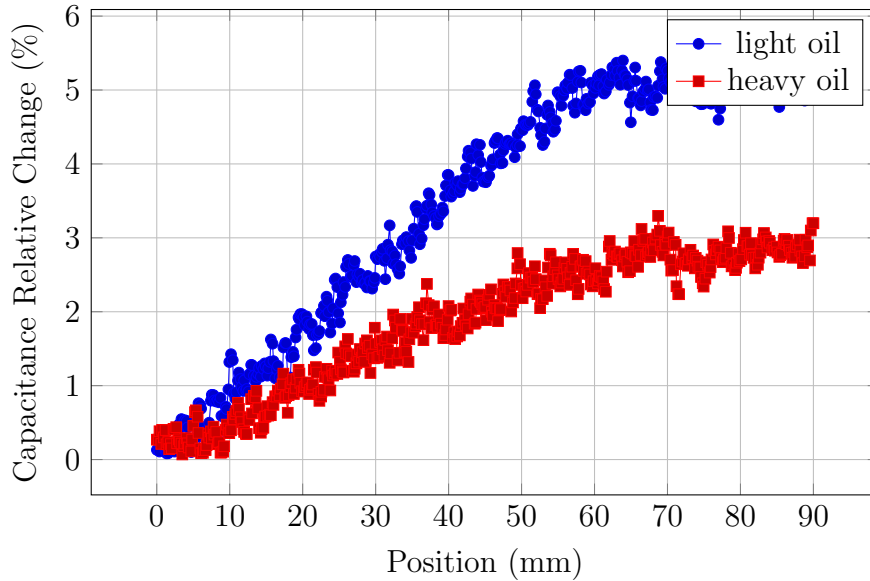


Figure 5.4: Plot of Capacitance Relative Change (%) vs. position (mm)

5.2.1 Related work

Precision Agriculture (PA) applications aim to enhance crop production while decreasing cost and resources [54]. Production enhancement is achieved by utilizing sensors to continuously monitor the state of the crops. However, one of the impediments to adopting PA is the high cost and complexity of equipment [55]. Thus, low-cost and simple-to-use instruments are desired to facilitate the application of PA strategies. In particular, soil moisture measurement represents a key enabling technology for smart irrigation systems [56], whose use avoids overestimating/underestimating irrigation. For instance, the use of an automated irrigation system based on soil moisture sensors contributed to saving up to 90 percent in water consumption compared to traditional irrigation practices [57]. However, accurate soil moisture measurement is challenging due to several factors, such as the differences between soil compositions and dynamic environmental conditions [58].

Measuring soil moisture was attempted using several sensing techniques, including resistance, neutron, and capacitance probes [59]. Resistance-based sensors are considered one of the simplest and cheapest methods to measure the soil moisture; however, they are highly affected by problems of aging and environmental variations [60]. Neutron probes, which work by measuring radioactive emissions, are robust and accurate but have several limitations related to their high cost, safety concerns, and licensing problems [61]. Capacitance-based sensors have several advantages like being non-invasive and highly sensitive; however, most of the commercially available sensors provide an aggregate estimate of the

soil water content based on measuring the changes in the dielectric constant of the soil. Since the dielectric constant is influenced by temperature changes [62], the use of these sensors requires specific compensation techniques and continuous calibration. To summarize, traditional soil moisture sensors provide analogue outputs and depend on calibration. This makes them vulnerable to changes in the environmental conditions and complicates the interpretation of their outputs.

5.2.2 Proposed sensing method

Since water possesses a high dielectric constant (80) in comparison to dry soil samples (1.5 - 4) [63], the capacitance of the soil increases significantly as more water is added to it. Based on this principle, traditional capacitive sensors (also known as continuous/analogue capacitive sensors) measure absolute moisture levels based on analog capacitance values. In contrast to the traditional sensors, we propose a capacitive sensor array composed of a set of electrodes distributed at discrete levels of a planar platform. When one of the electrodes is electrically excited, an electric field is created towards its adjacent grounded electrodes and penetrates the surrounding soil medium. The capacitance measured at the position of the excited electrode changes depending on the water contents of its surrounding medium. This process is applied to all electrodes in a sequential manner, providing an array of values representing the water content at each level of the sensor body. This design is characterized by its low cost and straightforward manufacturing.

5.2.3 Implementation and experimental evaluation

The proposed sensor design was implemented using a PCB holding forty-eight electrodes. The electrodes have equivalent dimensions and are distributed systematically on the PCB as shown in Figure 5.5. In contrast to the self-capacitance sensor array designed for the oil sensing application, the soil moisture sensor electrodes are completely coated with a solder mask layer. The addition of the isolation layer is essential in this application to avoid short-circuiting of the electrodes. The exact specifications of the implemented prototype are: electrode width: 55 mm, electrode height: 2 mm, vertical gap between electrodes: 1 mm, and PCB thickness: 1.6 mm. The connection tracks are embedded in the inner layers of the PCB. To measure the capacitance of the electrodes, four MPR121 devices were used. The working principle of these modules was described in the previous chapters.

A set of experiments were performed to assess the performance of the sensor under laboratory conditions. First, tuning experiments were performed to monitor the effect of different amounts of electric current on the sensitivity of the sensor. Starting by a dry soil sample (agricultural) with a weight of 300 grams, water was added gradually in defined amounts to create specific percentages of

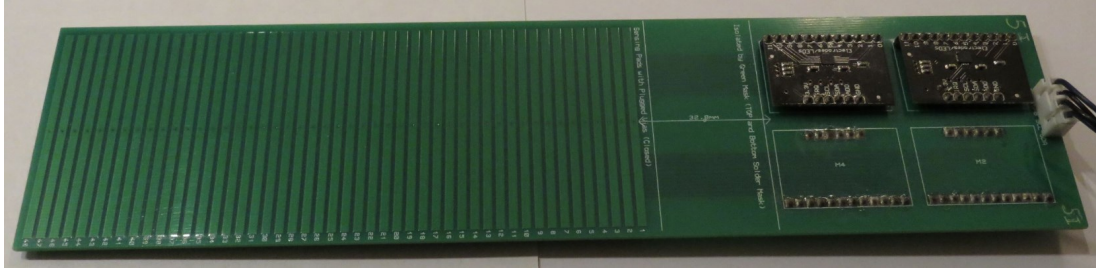


Figure 5.5: Coplanar capacitive sensor for soil moisture measurement

Soil Moisture Percentage	Water Weight (grams)
10	30
20	60
30	90
40	120
50	150
70	210
90	270

Table 5.1: Water amounts and moisture percentages

moisture. The amounts of water added, and the corresponding soil moisture levels are shown in Table 5.1.

We followed a consistent procedure for installing the sensors on the top surface of the soil and mixing the sample after each iteration. This process aimed to achieve a homogeneous distribution of the water within the soil layers. The sensor was configured to a fixed charge duration of $1 \mu\text{s}$ and the current was increased from 1 to $63 \mu\text{A}$ with increments of $1 \mu\text{A}$. Voltages measured at all electrodes were averaged and stored after the current was incremented. During these experiments, the average temperature and relative humidity were recorded as 29 degree Celsius and 65 percent respectively. A sample of the experimental results is shown in Figure 5.6. Note that the voltages are provided in digital form after analog-to-digital (ADC) conversion.

The results of the tuning experiment revealed that the sensitivity of the sensor

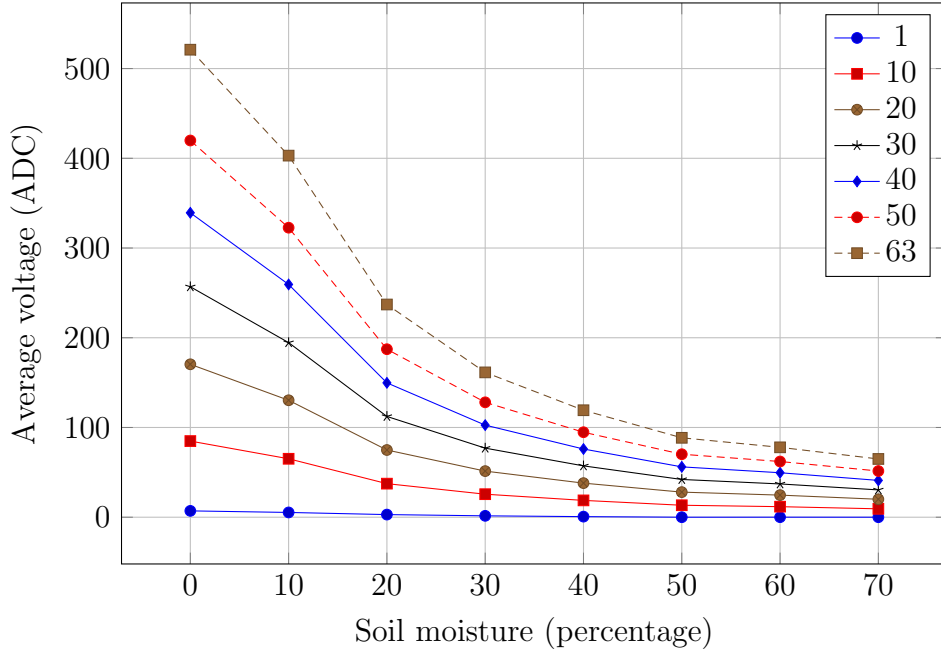


Figure 5.6: Average voltage (ADC) vs. soil moisture - tuning

increased as the excitation current increased. This can be deduced from observing the slope which gets steeper as the amount of current increases. Based on this observation, the largest amount of current ($63 \mu\text{A}$) was selected to be used throughout the experiments.

It is important to note that since water possesses a relatively high dielectric constant (80) in comparison to dry soil samples (1.5 - 4), as more water is added to the soil sample, the dielectric constant of the soil increases, and accordingly, the measured capacitance also increases. Since the voltage is inversely related to the capacitance, the measured voltage decreases with the increase of capacitance caused by added amounts of water.

In another experiment, we aimed to test the sensor performance during water evaporation process. For this purpose, the sensor was inserted into a mixture of clay and sandy soils which was irrigated once using tap water at the first day of the experiment. The sensor was activated and voltages of electrodes were saved automatically on an embedded SD card with a sampling rate of one measure per 10 seconds. The sensing system was battery operated and the experiment lasted for 12 days without intervention. For normalization, voltages measured in real-time were converted to relative change values based on (5.2). A sample of the results, taken per day, are shown in Figure 5.7.

$$RC[i] = \frac{Measured[i] - Saturation[i]}{Saturation[i]}, \quad (5.2)$$

Where i is the spatial index of the electrode, *Measured* is the voltage measured in real-time, and *Saturation* is the voltage recorded when the soil was irrigated.

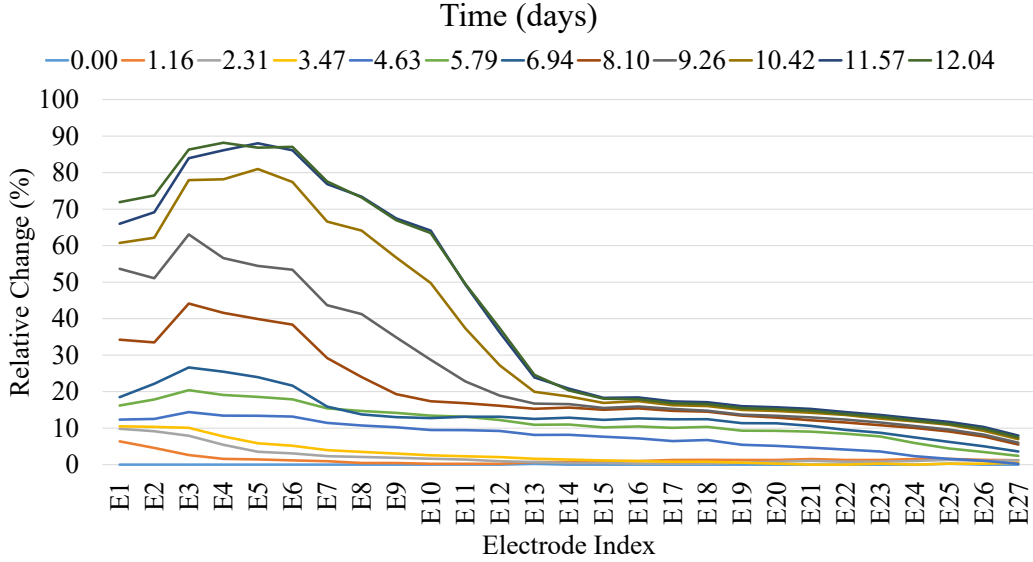


Figure 5.7: Relative moisture change vs. time

As shown in Figure 5.7, the relative change values of the electrodes increased with time. A "knee" point representing the edge between dry and wet soil layers becomes more obvious as more time passes. To extract the index of the interface layer automatically, a threshold-based detection algorithm could be used. Starting from the bottom electrode (E48), the algorithm iterates through all electrodes and detects the first electrode that exhibits a change greater than 10%. For instance, at the end of the experiment (day 12), the electrode with index 14 (E14) represents the interface between dry and wet soil layers. The threshold-based detection method could be used for demonstration, however, more advanced step-change detection algorithms could be used to detect the interface layer depending on the application requirements.

5.2.4 Conclusion

Measuring the soil moisture is of crucial importance for smart irrigation systems and water conservation plans. In this section, we presented the use of coplanar capacitive sensor arrays for measuring the soil moisture at different depths. Future development work includes evaluating the performance of these sensors when deployed in groups under realistic agriculture field conditions.

Chapter 6

Summary and future work

This dissertation presented new sensing systems and methods for characterizing multiphase mixtures based on their electrical properties. The developed systems were aimed mainly for measuring oil-thickness during oil spills. However, the applicability of the proposed methods was demonstrated to other multiphase sensing applications including online measurement of oil viscosity and in-situ characterization of soil moisture. This chapter summarizes the main topics of the developed work and presents the main contributions of the implemented systems.

6.1 Summary

Previous research studies done on developing technologies for cleaning up oil spills revealed that there is a major need for measuring oil spill thickness in real-time. After evaluating several commercially available sensors, it was found that none of the available sensing technologies could be used to accurately measure the oil slick thickness under open-water conditions. The work presented in this dissertation aimed to respond to this need by developing measurement systems that can work against different types of crude and refined oils floating on the seawater surface. Different models of the proposed sensing strategy were implemented to be mounted on skimmers, in the apex of a boom, or to be deployed from a vessel in the area of an oil skimming operation.

After reviewing the related work presented in the literature, the dissertation starts by describing the design, implementation, and testing of the first oil-thickness measurement system based on a self-capacitance sensor array. The self-capacitance sensor array was designed to measure oil thicknesses ranging from 3 mm to 100 mm. It is composed of a set of electrodes to measure the capacitance of the air/oil/water layers contacting the sensor body. The measurements of the electrodes are used to detect multiple interfaces separating the components of the measured multiphase mixture. Several methods for detecting the interfaces were presented and discussed. After detecting the interfaces, the thickness of

each phase, including the oil phase, is calculated based on the pre-defined sensor dimensions. This approach does not require any calibration against different types of water or oil.

To evaluate the performance of the self-capacitance sensor array, the implemented prototype was tested against multiple oil types and thicknesses and in static and dynamic liquid environments. The testing was performed at the *Ohmsett* testing facility and designed to emulate realistic oil spill conditions. The test cases included three rigorous tests: dipping in a laboratory setup, forward-moving at different speeds while being mounted to a bridge, and subjected to different wave conditions while being mounted on a skimmer. The experimental results demonstrated the ability of the implemented prototype to operate against different oil types without requiring calibration and showed a measurement accuracy in the order of the sensor resolution.

Another measurement system was developed based on the conclusions obtained from testing the self-capacitance sensor array. The main motivation behind the development of the dual-modality ultrasonic/capacitive sensing system is to mitigate the effects of oil fouling and to improve the measurement resolution. This is done by using thin needle-like pins instead of the planar electrodes and by adding an ultrasonic sensor with high resolution to measure the liquid level. The thickness of the oil phase is estimated based on the fusion of the information obtained from the capacitive sensor array and the distances measured by the ultrasonic sensor. Two use-case-specific models were developed. The first model was designed as a hand-held device for use in testing facilities as a reference testing tool. The second model was designed to measure the oil thickness in real-time while being mounted on a skimmer during oil cleaning operations. The dual-modality system was tested under laboratory conditions. The results showed enhancements in terms of sensor resolution and accuracy.

In addition to the oil-thickness measurement application, the proposed sensing strategy was applied to other related multiphase sensing applications. Inspired by the problem of oil fouling, a new method for measuring oil viscosity was proposed. The proposed method is based on using a coplanar capacitive sensor in a dynamic scheme to infer the kinematic viscosity of the oil samples. Initial experimental work demonstrated the applicability of the proposed method to differentiate between light and heavy oil samples. In addition, the applicability of the proposed sensor design was demonstrated to detect and track interfaces separating different stratified layers of soil moisture. In contrast to traditional soil moisture sensors that provide analog values representing the total measured moisture, the proposed sensor allows for tracking interfaces separating wet and dry soil layers. The importance of this technique is in extracting a new sensor output describing the depth of the wet soil layers instead of the percentages of the total soil moisture. This output could be used more easily by traditional farmers to estimate the wetness state of the soil and to plan irrigation.

6.2 Contributions

The main contribution of my work is the development of a multiphase characterization method that can work against different types of materials without requiring calibration. As an application for the proposed method, we targeted the oil spill sensing application where a measurement system was designed and implemented to measure the thickness of oil slicks in open-water environments. The proposed measurement system can work against different types of oil/water based on the initial calibration done in the air only.

Another major contribution of our work is related to the proposed sensor design that mitigates the problem of oil fouling. Note that the performance of traditional contact-based sensors usually degrades when dealing with highly viscous oils under dynamic liquid conditions. Thus, we proposed a new design for a capacitive sensor array that can considerably reduce the effect of fouling by using a multi-row self-capacitance sensor array equipped with thin needle-like pins. It is important to note that several designs were first analyzed using finite element simulations, and then experiments were performed to validate the simulations and select the optimized design.

Several methods and algorithms were proposed for interface detection and signal classification. These methods include an unsupervised step-change detection technique to detect the interfaces separating distinct layers of the multiphase mixture. In addition, we designed and implemented a signal classification technique based on machine-learning models to identify the type of material surrounding each of the sensing cells in real-time. For this purpose, we proposed a methodology for creating a labeled dataset under laboratory experimental conditions.

To enhance the measurement resolution of the discrete capacitive sensing technique, we proposed a new dual-modality sensing system that combines the information of the capacitive sensor array with information of an ultrasonic range detection sensor. The proposed system followed a collaborative sensor fusion approach to infer the thickness of the target oil layer. The proposed approach benefits from the geometrical dimensions of the capacitive sensor array and the liquid level measured by the ultrasonic sensor. The main contribution of the proposed fusion method is reducing the error in estimating the position of the air/oil interface. In addition, the dual-modality sensing system has several advantages including online calibration capability, a fast response rate, and low-cost in terms of manufacturing and maintenance.

It is important to note that the proposed sensing concept is not limited to the oil spill sensing application and could be applied to characterize other multiphase mixtures; industrial multiphase flows containing gas/liquid and liquid/liquid interfaces.

6.3 Limitations

The main limitation that affects the proposed discrete capacitive sensing technique is that the measurement resolution is limited to the dimensions of the sensor array. In other words, since the gap between the electrodes and the width of the electrodes are limited to some considerable value (1 or 2 mm), the resolution of the measurement cannot be increased beyond a certain threshold (3 mm).

In addition to the basic limitation of the discrete sensing principle, we should mention that the needle-like pins proposed to mitigate the effects of oil fouling have some limits in terms of thickness and length. For instance, to increase the rate of signal change, the length of the pins could be increased to penetrate the oil fouling layer more effectively. However, increasing the length of the pins would also require to increase their thickness to maintain their strength; this would also affect the sensor resolution. In summary, the designer should make a trade-off between the lengths and thickness of the pins while considering the required resolution and the types of material.

6.4 Future work

For the future development of the proposed systems, several research tracks could be followed. First, in terms of the sensing principle, we should mention that the planar capacitive sensors could be used in the form of tomographic imaging systems. Based on the principle of electrical tomography, the sensing domain is divided into a large number of pixels, and image reconstruction algorithms are used to reconstruct the electrical properties of the sensing domain. This track should be followed if it is required to increase the spatial resolution of the sensor beyond the dimensions of the electrodes. However, we should mention that tomographic imaging approaches are characterized by the ill-posedness and non-linearity of the mathematical problem they intend to solve. In other words, the number of measurements acquired by the sensor electrodes is much smaller than the number of pixels included in the sensing domain. Thus, the main challenge in this approach is to solve the inverse problem of inferring the electrical properties of the sensing domain using the measurements. Machine-learning-based methods could be evaluated to create this non-linear relation between the measurements and the type of material included in the sensing domain.

In terms of signal processing and thickness estimation, deep learning methods could be evaluated to extract quantitative information about the components of the multiphase mixtures. Based on the results of this study, the deployment of these methods under online conditions should be planned in terms of hardware and software requirements. The challenges related to this research work include the problem of acquiring labeled images for training, the generalization of the trained models on unseen types of oils, and maintaining the logical order of layers

in the output images.

Depending on the requirements of the application, one possible track is to study the deployment of the developed sensors in the form of a wireless sensor network to cover a large region of interest. In such cases, the application would aim to map the oil spill in a specific target area. In this case, several research challenges should be handled such as the communication and fusion of the oil thickness information.

Regarding the additional applications such as the oil viscosity sensing system, the experimental work should be extended to develop accurate relations between the viscosity of the measured oils and the output of the sensor. In particular, this should be done by performing additional experiments to compare the output of the proposed sensor to the output of other standard viscometers available in the market. Similarly, for the soil moisture sensing application, experimental work could be expanded to evaluate the performance and lifetime of the developed sensors under field conditions.

Appendix A

Abbreviations

ADC	Analog-to-Digital Converter
BS	Base Station
ECT	Electrical Capacitance Tomography
FFT	Fast Fourier Transform
GPS	Global Positioning System
GUI	Graphical User Interface
I2C	Inter-Integrated Circuit
LED	Light-Emitting Diode
MUT	Material Under Test
MSE	Mean Squared Error
OLED	Organic Light Emitting Diodes
PCB	Printed Circuit Board
PCS	Planar Capacitive Sensor
RF	Radio Frequency
SNR	Signal-to-Noise Ratio
SPI	Serial Peripheral Interface
TTL	Transistor-Transistor Logic
UART	Universal Asynchronous Receiver/Transmitter
USB	Universal Serial Bus

Bibliography

- [1] J. Beyer, H. C. Trannum, T. Bakke, P. V. Hodson, and T. K. Collier, “Environmental effects of the Deepwater Horizon oil spill: a review,” *Marine pollution bulletin*, vol. 110, no. 1, pp. 28–51, 2016. Publisher: Elsevier.
- [2] F. Aguilera, J. Méndez, E. Pásaro, and B. Laffon, “Review on the effects of exposure to spilled oils on human health,” *Journal of Applied Toxicology: An International Journal*, vol. 30, no. 4, pp. 291–301, 2010. Publisher: Wiley Online Library.
- [3] M. Fingas, “How to measure slick thickness (or not),” in *Proc. of the 35th Arctic and Marine Oil spill Program Technical Seminar*, pp. 617–652, 2012.
- [4] C. E. Brown, M. Fruhwirth, M. F. Fingas, G. Vaudreuil, J.-P. Monchalain, M. Choquet, R. Heon, C. Padioleau, R. H. Goodman, and J. V. Mullin, “Oil slick thickness measurement: a possible solution to a long-standing problem,” in *Arctic and Marine Oilspill Program Technical Seminar*, pp. 427–440, Ministry of Supply and Services, Canada, 1995.
- [5] C. Federici and J. Mintz, “Oil properties and their impact on spill response options,” *CNA, Alexandria, VA, USA*, 2014.
- [6] D. G. W. Johnson, C. Grayson, K. Dykstra, A. Stromlund, M. Wiggins, D. M. Fitzpatrick, and D. P. Swaszek, “Development of Smart Skimming Technologies,” *Final Report*, no. 7, p. 94, 2016.
- [7] M. Fingas, “The challenges of remotely measuring oil slick thickness,” *Remote sensing*, vol. 10, no. 2, p. 319, 2018. Publisher: Multidisciplinary Digital Publishing Institute.
- [8] K. Polychronis and K. Vassilia, “Detection of oil spills and underwater natural oil outflow using multispectral satellite imagery,” *International Journal of Remote Sensing Applications*, vol. 3, no. 3, pp. 145–154, 2013. Publisher: Science and Engineering Publishing Company.
- [9] O. P. N. Calla, H. K. Dadhich, and S. Singhal, “Oil spill detection using multi frequency microwave sensor onboard satellite; SSM/I and AMSR-E,”

in *2013 IEEE International Geoscience and Remote Sensing Symposium-IGARSS*, pp. 3710–3713, IEEE, 2013.

- [10] O. P. N. Calla, N. Ahmadian, and S. Hasan, “Estimation of emissivity and scattering coefficient of low saline water contaminated by diesel in Cj band (5.3 GHz) and Ku band (13.4 GHz),” *Indian Journal of Radio and Space Physics (IJRSP)*, vol. 40, pp. 267–274, 2011. Publisher: NISCAIR-CSIR, India.
- [11] F. Nunziata and M. Migliaccio, “Oil spill monitoring and damage assessment via PolSAR measurements,” *Aquatic Procedia*, vol. 3, pp. 95–102, 2015. Publisher: Elsevier.
- [12] M. Fingas and C. E. Brown, “Chapter 6 - Oil Spill Remote Sensing: A Review,” in *Oil Spill Science and Technology* (M. Fingas, ed.), pp. 111–169, Boston: Gulf Professional Publishing, Jan. 2011.
- [13] V. Karathanassi, “Spectral unmixing evaluation for oil spill characterization,” *Int. J. Remote Sens. Appl.*, vol. 4, 2014.
- [14] S. V. Corporation, *GER 1500*, Online (accessed December 1, 2020). <https://www.spectravista.com/our-instruments/ger1500/>.
- [15] A. Massaro, A. Lay-Ekuakille, D. Caratelli, I. Palamara, and F. C. Morabito, “Optical performance evaluation of oil spill detection methods: Thickness and extent,” *IEEE Transactions on Instrumentation and Measurement*, vol. 61, no. 12, pp. 3332–3339, 2012. Publisher: IEEE.
- [16] G. Baozhen, S. Jingbin, L. Pengcheng, L. Qieni, and W. Di, “Designing an optical set-up of differential laser triangulation for oil film thickness measurement on water,” *Review of Scientific Instruments*, vol. 84, no. 1, p. 013105, 2013. Publisher: American Institute of Physics.
- [17] S. Oh and M. Lee, “Oil spill detection sensor using artificial illumination with blue LEDs,” in *SENSORS, 2012 IEEE*, 2012.
- [18] M. Saleh, G. Oueidat, M. Ghamlouch, I. H. Elhajj, and D. Asmar, “LED-based Spectrometer for In Situ Oil Slick Thickness Measurement,” in *2018 IEEE International Multidisciplinary Conference on Engineering Technology (IMCET)*, IEEE, 2018.
- [19] H. Denkilian, A. Koulakezian, R. Ohannessian, M. S. Chalfoun, M. K. W. Joujou, A. Chehab, and I. H. Elhajj, “Wireless sensor for continuous real-time oil spill thickness and location measurement,” *IEEE Transactions on Instrumentation and Measurement*, vol. 58, no. 12, pp. 4001–4011, 2009. Publisher: IEEE.

- [20] X. Hu and W. Yang, “Planar capacitive sensors—designs and applications,” *Sensor Review*, vol. 30, no. 1, pp. 24–39, 2010.
- [21] W. Yang and A. K. Hennessey, “Security scanners with capacitance and magnetic sensor arrays,” Oct. 10 2006. US Patent 7,119,553.
- [22] G. Diamond, D. Hutchins, T. Gan, P. Purnell, and K. Leong, “Single-sided capacitive imaging for ndt,” *Insight-Non-Destructive Testing and Condition Monitoring*, vol. 48, no. 12, pp. 724–730, 2006.
- [23] K. Wei, C.-H. Qiu, and K. Primrose, “Super-sensing technology: industrial applications and future challenges of electrical tomography,” *Philosophical Transactions of the Royal Society A: Mathematical, Physical and Engineering Sciences*, vol. 374, no. 2070, p. 20150328, 2016.
- [24] W. Yang, *Imaging Sensor Technologies and Applications*. IET Publishing, 2020.
- [25] W. Yang, “Sensors and instrumentation for monitoring and control of multi-phase separation,” *Measurement and control*, vol. 39, no. 6, pp. 178–184, 2006.
- [26] K. Spaargaren and A. C. Leyen, “U-shaped capacitor level gauge,” Sept. 16 1986. US Patent 4,611,489.
- [27] W. Yang, M. Brant, and M. Beck, “A multi-interface level measurement system using a segmented capacitance sensor for oil separators,” *Measurement Science and Technology*, vol. 5, no. 9, p. 1177, 1994.
- [28] A. Hwili and W. Yang, “Multi-modality multi-interface level measurement,” in *Journal of Physics: Conference Series*, vol. 76, p. 012008, 2007.
- [29] T. Shi, C. Xie, S. Huang, R. A. Williams, and M. Beck, “Capacitance-based instrumentation for multi-interface level measurement,” *Measurement Science and Technology*, vol. 2, no. 10, p. 923, 1991.
- [30] H. Wang, W. Yin, W. Yang, and M. Beck, “Optimum design of segmented capacitance sensing array for multi-phase interface measurement,” *Measurement Science and Technology*, vol. 7, no. 1, p. 79, 1996.
- [31] S. F. A. Bukhari and W. Yang, “Multi-interface level sensors and new development in monitoring and control of oil separators,” *Sensors*, vol. 6, no. 4, pp. 380–389, 2006.
- [32] C. Xie, S. Huang, M. Beck, B. Hoyle, R. Thorn, C. Lenn, and D. Snowden, “Electrical capacitance tomography for flow imaging: system model for

- development of image reconstruction algorithms and design of primary sensors,” *IEE Proceedings G (Circuits, Devices and Systems)*, vol. 139, no. 1, pp. 89–98, 1992.
- [33] O. Isaksen, A. Dico, and E. A. Hammer, “A capacitance-based tomography system for interface measurement in separation vessels,” *Measurement science and technology*, vol. 5, no. 10, p. 1262, 1994.
- [34] I. D. Johnson, “Method and apparatus for measuring water in crude oil,” Feb. 17 1987. US Patent 4,644,263.
- [35] M. Da Silva, E. Schleicher, and U. Hampel, “Capacitance wire-mesh sensor for fast measurement of phase fraction distributions,” *Measurement Science and Technology*, vol. 18, no. 7, p. 2245, 2007.
- [36] H. Kawakatsu, K. Tanaka, and H. Uematsu, “Level sensor,” Aug. 15 2000. US Patent 6,101,873.
- [37] Y. Ye, J. Deng, S. Shen, Z. Hou, and Y. Liu, “A novel method for proximity detection of moving targets using a large-scale planar capacitive sensor system,” *Sensors*, vol. 16, no. 5, p. 699, 2016.
- [38] F. Semiconductor, “Proximity capacitive touch sensor controller,” *MPR121*, Sep, 2010.
- [39] BSEE, *Ohmsett – The National Oil Spill Response Research and Renewable Energy Test Facility*, Online (accessed December 1, 2020). <https://www.ohmsett.com/>.
- [40] Y. Huang, Z. Zhan, and N. Bowler, “Optimization of the coplanar interdigital capacitive sensor,” in *AIP Conference Proceedings*, vol. 1806, p. 110017, AIP Publishing LLC, 2017.
- [41] A. A. Carey, “The dielectric constant of lubrication oils,” tech. rep., Computational Systems Incorporated, 1998.
- [42] F. Pedregosa, G. Varoquaux, A. Gramfort, V. Michel, B. Thirion, O. Grisel, M. Blondel, P. Prettenhofer, R. Weiss, V. Dubourg, J. Vanderplas, A. Passos, D. Cournapeau, M. Brucher, M. Perrot, and E. Duchesnay, “Scikit-learn: Machine learning in Python,” *Journal of Machine Learning Research*, vol. 12, pp. 2825–2830, 2011.
- [43] K. Haroon, A. Arafeh, P. Martin, T. Rodgers, C. Mendoza, and M. Baker, “Use of inline near-infrared spectroscopy to predict the viscosity of shampoo using multivariate analysis,” *International journal of cosmetic science*, vol. 41, no. 4, pp. 346–356, 2019.

- [44] V. K. Mishra, B. E. Barbosa, B. LeCompte, Y. Morikami, C. Harrison, K. Fujii, C. Ayan, L. Chen, H. Dumont, D. F. Diaz, *et al.*, “Downhole viscosity measurement: revealing reservoir fluid complexities and architecture,” in *SPWLA 55th Annual Logging Symposium*, Society of Petrophysicists and Well-Log Analysts, 2014.
- [45] B. Jakoby, M. Scherer, M. Buskies, and H. Eisenschmid, “An automotive engine oil viscosity sensor,” *IEEE Sensors Journal*, vol. 3, no. 5, pp. 562–568, 2003.
- [46] X. Zhu, C. Zhong, and J. Zhe, “Lubricating oil conditioning sensors for on-line machine health monitoring—a review,” *Tribology International*, vol. 109, pp. 473–484, 2017.
- [47] L. Markova, V. Makarenko, M. Semenyuk, and A. Zozulya, “On-line monitoring of the viscosity of lubricating oils,” *Journal of Friction and Wear*, vol. 31, no. 6, pp. 433–442, 2010.
- [48] R. E. Kasameyer and W. Warren, “Fast-recovery viscometer,” July 1 2003. US Patent 6,584,831.
- [49] R. A. Norcross Jr, “Falling-piston viscometer and methods for use thereof,” Oct. 28 2014. US Patent 8,869,600.
- [50] R. Goyal and D. M. Yadav, “Design and simulation of a mems-based capacitive micro-machined ultrasonic transducer for viscosity sensing applications,” 2019. IOP Publishing COMSOL.
- [51] M. Appleby, F. K. Choy, L. Du, and J. Zhe, “Oil debris and viscosity monitoring using ultrasonic and capacitance/inductance measurements,” *Lubrication Science*, vol. 25, no. 8, pp. 507–524, 2013.
- [52] M. Yunus and A. Arifin, “Design of oil viscosity sensor based on plastic optical fiber,” in *Journal of Physics: Conference Series*; IOP Publishing: Bristol, UK, p. 012083, 2018.
- [53] T. Instruments, “Capacitive-based liquid level sensing sensor reference design,” tech. rep., Texas Instruments Incorporated TIDU736A, 2015.
- [54] M. Srbinovska, C. Gavrovski, V. Dimcev, A. Krkoleva, and V. Borozan, “Environmental parameters monitoring in precision agriculture using wireless sensor networks,” *Journal of Cleaner Production*, vol. 88, pp. 297–307, 2015.
- [55] M. Keskin, S. M. SAY, and S. G. Keskin, “Evaluation of a low-cost gps receiver for precision agriculture use in adana province of turkey,” *Turkish Journal of Agriculture and Forestry*, vol. 33, no. 1, pp. 79–88, 2009.

- [56] R. G. Vieira, A. M. Da Cunha, L. B. Ruiz, and A. P. De Camargo, “On the design of a long range wsn for precision irrigation,” *IEEE Sensors Journal*, vol. 18, no. 2, pp. 773–780, 2018.
- [57] J. Gutiérrez, J. F. Villa-Medina, A. Nieto-Garibay, and M. Á. Porta-Gándara, “Automated irrigation system using a wireless sensor network and gprs module,” *IEEE Transactions on Instrumentation and Measurement*, vol. 63, no. 1, pp. 166–176, 2014.
- [58] S. R. Evett, J. A. Tolck, and T. A. Howell, “Soil profile water content determination,” *Vadose Zone Journal*, vol. 5, no. 3, pp. 894–907, 2006.
- [59] W. Dorigo, W. Wagner, R. Hohensinn, S. Hahn, C. Paulik, A. Xaver, A. Gruber, M. Drusch, S. Mecklenburg, P. v. Oevelen, *et al.*, “The international soil moisture network: a data hosting facility for global in situ soil moisture measurements,” *Hydrology and Earth System Sciences*, vol. 15, no. 5, pp. 1675–1698, 2011.
- [60] M. Saleh, I. H. Elhajj, D. Asmar, I. Bashour, and S. Kidess, “Experimental evaluation of low-cost resistive soil moisture sensors,” in *Multidisciplinary Conference on Engineering Technology (IMCET), IEEE International*, pp. 179–184, IEEE, 2016.
- [61] T. Schmugge, T. Jackson, and H. McKim, “Survey of methods for soil moisture determination,” *Water Resources Research*, vol. 16, no. 6, pp. 961–979, 1980.
- [62] A. Chanzy, J.-C. Gaudu, and O. Marloie, “Correcting the temperature influence on soil capacitance sensors using diurnal temperature and water content cycles,” *Sensors*, vol. 12, no. 7, pp. 9773–9790, 2012.
- [63] R. T. Atkins, T. Pangburn, R. E. Bates, and B. E. Brockett, “Soil moisture determinations using capacitance probe methodology,” tech. rep., Cold Regions Research and Engineering Laboratory, 1998.